

Photoproduction of
 D^* Mesons and
 D^* Mesons Associated with Jets
at HERA

Dissertation

zur Erlangung des Doktorgrades
des Fachbereichs Physik
der Universität Hamburg

vorgelegt von
GERO FLUCKE
aus Hamburg

Hamburg
2005

| | |
|--|---|
| Gutachter der Dissertation: | Prof. Dr. V. Blobel Prof. Dr. R. Klanner |
| Gutachterin und Gutachter der Disputation: | Prof. Dr. B. Naroska Prof. Dr. P. Schleper |
| Datum der Disputation: | 3. März 2005 |
| Vorsitzende des Prüfungsausschusses: | Prof. Dr. C. Hagner |
| Vorsitzender des Promotionsausschusses und Dekan des Fachbereichs Physik: | Prof. Dr. G. Huber |

Abstract

Charm production is investigated in the H1 experiment at the electron-proton collider HERA. The data of the years 1999 and 2000 are analysed, corresponding to an integrated luminosity of 51.1 pb^{-1} . Photoproduction is selected by detecting the scattered electron at small angles, leading to photon virtualities $Q^2 < 0.01 \text{ GeV}^2$ and photon-proton centre-of-mass energies $171 < W_{\gamma p} < 256 \text{ GeV}$. Charm is tagged by reconstruction of D^* mesons in the pseudorapidity range $|\eta(D^*)| < 1.5$ and for transverse momenta $p_t(D^*) > 2 \text{ GeV}$. Differential cross sections as a function of $p_t(D^*)$, $\eta(D^*)$ and $W_{\gamma p}$ are measured and compared to QCD predictions in leading order, supplemented with parton showers, and in next-to-leading order. Reasonable agreement is found.

In a further measurement a jet not containing the D^* meson is required in addition to the D^* . Jets down to $p_t(\text{jet}) > 3 \text{ GeV}$ are shown to be reliably measurable in the central detector region $|\eta(\text{jet})| < 1.5$. Differential cross sections for variables characterising the D^* , the jet and the D^* +jet system are determined. They reveal the presence of radiative processes in addition to leading order photon-gluon fusion. The cross sections are compared with QCD calculations in collinear and in k_t -factorisation. Neither of them describes all observed features.

Kurzfassung

Die Produktion von Charm-Quarks wird mit dem H1-Experiment am Elektron-Proton-Speicherring HERA untersucht. Die Daten der Jahre 1999 und 2000 mit einer integrierten Luminosität von 51.1 pb^{-1} werden analysiert. Durch den Nachweis des gestreuten Elektrons unter kleinen Winkeln werden Photoproduktionsereignisse mit einer Photonvirtualität von $Q^2 < 0.01 \text{ GeV}^2$ und einer Schwerpunktsenergie des Photon-Proton-Systems von $171 < W_{\gamma p} < 256 \text{ GeV}$ ausgewählt. Der Nachweis von Charm-Quarks erfolgt durch die Rekonstruktion von D^* -Mesonen mit einem Transversalimpuls von $p_t(D^*) > 2 \text{ GeV}$ und einer Pseudorapidität $|\eta(D^*)| < 1.5$. Differentielle Wirkungsquerschnitte werden in Abhängigkeit von $p_t(D^*)$, $\eta(D^*)$ und $W_{\gamma p}$ bestimmt. Die Übereinstimmung mit QCD-Vorhersagen führender Ordnung mit Partonschauern und nächstführender Ordnung ist zufriedenstellend.

In einer weiteren Messung wird zusätzlich zum D^* -Meson ein Jet selektiert, der nicht das D^* enthält. Jets können im zentralen Detektor, $|\eta(\text{jet})| < 1.5$, ab Transversalimpulsen von $p_t(\text{jet}) > 3 \text{ GeV}$ gemessen werden. Differentielle Wirkungsquerschnitte werden für Jet-, D^* - und kombinierte D^* +Jet-Größen bestimmt. Sie zeigen, dass Strahlungsprozesse zusätzlich zur Photon-Gluon-Fusion in führender Ordnung wichtig sind. Die Messungen werden mit QCD-Rechnungen in kollinearer und k_t -Faktorisierung verglichen. Keine Rechnung kann alle beobachteten Eigenschaften beschreiben.

Contents

| | |
|---|-----------|
| Introduction | 1 |
| 1 Theoretical Overview | 3 |
| 1.1 Electron-Proton Scattering at HERA | 3 |
| 1.2 Factorisation and Parton Evolution | 4 |
| 1.3 Photoproduction at HERA | 7 |
| 1.4 Photoproduction of D^* Mesons | 8 |
| 1.4.1 Heavy Quark Production | 8 |
| 1.4.2 Fragmentation | 9 |
| 1.5 Jets and Jet Algorithms | 11 |
| 1.6 D^* +Jet Double Tag | 13 |
| 1.6.1 The Jet as Second Tag | 14 |
| 1.6.2 Combined D^* +Jet Quantities | 14 |
| 2 QCD Calculations of D^* and D^*+Jet Cross Sections | 18 |
| 2.1 Leading Order Calculations with Parton Showers | 18 |
| 2.2 Next-to-Leading Order Calculations | 20 |
| 2.3 The FMNR Program | 22 |
| 2.4 Contribution from Beauty Production | 26 |
| 3 The H1 Experiment at HERA | 28 |
| 3.1 Central Tracking Detectors | 29 |
| 3.2 Calorimeters | 30 |
| 3.3 Luminosity System and Electron Taggers | 31 |
| 3.4 The Trigger System | 32 |
| 3.5 Particle Identification using Energy Loss: dE/dx | 33 |
| 3.6 Detector Simulation | 34 |
| 3.7 Combining Tracks and Clusters | 36 |
| 4 Reconstruction of D^* Mesons | 40 |
| 4.1 Decay of D^* Mesons | 40 |
| 4.2 D^* Meson Selection | 41 |
| 4.3 Determination of the Number of D^* Mesons | 42 |
| 4.3.1 Monte Carlo Treatment | 43 |
| 4.3.2 Alternative Methods | 44 |

| | | |
|----------|---|------------|
| 5 | Inclusive D^* Meson Measurements | 46 |
| 5.1 | Run Selection and Luminosity Determination | 46 |
| 5.2 | Photoproduction Selection and Trigger Requirements | 47 |
| 5.3 | Improving the D^* Signal | 49 |
| 5.3.1 | Cuts Based on Particle Identification | 49 |
| 5.3.2 | Further Background Suppression | 50 |
| 5.4 | Comparison of Data and Simulation | 52 |
| 5.4.1 | Track Resolution: D^0 Width | 53 |
| 5.4.2 | Quality of D^* and Track Simulation | 53 |
| 5.5 | Correction Factors | 57 |
| 5.5.1 | L1 Trigger Efficiency | 57 |
| 5.5.2 | L4 Trigger Efficiency | 58 |
| 5.5.3 | Electron Tagger Acceptance | 60 |
| 5.5.4 | Reconstruction Efficiency | 61 |
| 5.6 | Systematic Uncertainties | 64 |
| 5.7 | Cross Sections | 66 |
| 5.7.1 | Differential Cross Sections | 67 |
| 5.7.2 | Double Differential Cross Sections | 68 |
| 6 | Measurement of D^* Mesons Associated with a Jet | 71 |
| 6.1 | Jet Selection | 71 |
| 6.2 | Comparison of Data and Simulation | 73 |
| 6.2.1 | D^* and Jet Quantities | 73 |
| 6.2.2 | Composition of the Transverse Jet Momentum | 74 |
| 6.3 | Resolution of Jet Quantities | 77 |
| 6.4 | Transverse Energy Flow Relative to the Jet | 77 |
| 6.5 | Correction Factors, Purities and Stabilities | 82 |
| 6.5.1 | Total D^* +Jet Sample | 84 |
| 6.5.2 | Single D^* and Jet Quantities | 85 |
| 6.5.3 | Combined D^* +Jet Quantities | 85 |
| 6.6 | Systematic Uncertainties | 86 |
| 6.7 | Hadronisation Corrections | 88 |
| 6.8 | Cross Sections | 92 |
| 7 | Summary and Discussion of D^* and D^*+Jet Cross Sections | 99 |
| 8 | Outlook | 101 |
| | Bibliography | 102 |

Introduction

Elementary particle physics studies the smallest accessible constituents of matter and their interactions. To date they are described by the so-called Standard Model where matter consists of six quark flavours and six leptons. The observed strong and electroweak forces between these elementary particles can be described by quantum field theories. The theory of the strong interaction between quarks, mediated by gluons, is called Quantum Chromodynamics (QCD). The Standard Model describes very successfully almost all observed phenomena in particle physics.

A characteristic feature of QCD is the “asymptotic freedom” which describes the fact that with increasing energy (or decreasing distance) the strong coupling constant α_s becomes smaller and smaller, leading to quasi free particles. The Nobel prize 2004 was awarded for the theoretical discovery of asymptotic freedom.

The prediction of scattering amplitudes in quantum field theories is usually obtained by a perturbative expansion in the coupling constant. The expansion series is truncated at a fixed order or only the leading terms are resummed to all orders. This approach requires a small coupling constant to ensure the convergence of the expansion which makes it possible to neglect higher order terms which are very complicated to calculate.

Since the strong coupling constant is large at low energy scales, perturbative calculations in QCD require the presence of a large scale compared to the QCD parameter Λ_{QCD} , e. g. a large virtuality Q^2 , a large transverse momentum p_t or large particle masses m . Even the lightest of the heavy quark flavours, the charm quark, has a mass large enough to provide such a scale, $m_c \sim 1.5 \text{ GeV}/c^2$. Therefore studying the heavy quark production mechanism is an ideal testing ground of perturbative QCD even at small p_t and low Q^2 . Consequently charm production has been investigated in various particle collisions (e. g. γp [1,2], ep [3,4], $p\bar{p}$ [5], $\gamma\gamma$ [6]).

In this thesis charm production will be studied in electron-proton collisions at HERA analysing data obtained by the H1 experiment in the years 1999 and 2000. Photoproduction events will be selected, a kinematical regime where the virtuality of the exchanged photon is very low, $Q^2 \sim 0$. Charm is tagged via reconstruction of D^* mesons from their decay products. Previous measurements by the H1 [1] and ZEUS experiment [2,7] showed that charm production cross sections can be reasonably described by the theory, taking into account the uncertainties of the data and the theory. The main production mechanism has been found to be photon-gluon fusion where the incoming photon interacts with a gluon from the proton forming a charm-anticharm pair. But particularly when requiring two jets in addition to the D^* meson, as is done in ZEUS analyses [2,8], in some regions of phase space the agreement is worse, mainly if the “resolved” contribution is enhanced, i. e. for events where the photon develops hadronic structure before the hard interaction.

Hence it is desirable to investigate the production process in more detail by tagging more than one product of the hard interaction. The statistics in data is too low to allow the reconstruction of two D^* mesons. Even the reconstruction of the second charm quark via its semileptonic decay producing a high momentum muon is very limited in statistics [9,10]. Therefore in this thesis jets are studied for the first time in charm photoproduction at the H1 experiment. In addition to the D^* meson a jet not containing the D^* is selected. Although the jet does not include a flavour tag, the correlations between the D^* meson and the jet test details of the production process.

The outline of the thesis is as follows: First an overview of the theoretical concepts is given (chapter 1) and different approaches of perturbative QCD calculations of heavy quark photoproduction are introduced (chapter 2). In chapter 3 the relevant components of the H1 detector and the algorithm to combine track and cluster measurements are described, followed by the methods to reconstruct D^* mesons and to determine their number (chapter 4). Chapter 5 presents the inclusive D^* analysis resulting in a comparison of differential cross sections with theoretical predictions. Subsequently jets are studied in chapter 6 and D^* +jet cross sections are derived and confronted with the predictions. In chapter 7 the results are summarised and discussed before the last chapter gives an outlook.

Chapter 1

Theoretical Overview

This chapter gives an overview of theoretical aspects relevant in photoproduction of D^* mesons at HERA.

First a general introduction into electron-proton (ep) collisions at HERA is given and the relevant kinematic quantities are presented. It is described how the interaction can be understood in terms of Quantum Chromodynamics (QCD), the theory of the strong interaction.

Thereafter photoproduction is described, a kinematical region where ep interactions are mediated by a quasi real photon and hence can be viewed as photon-proton collisions. Charm quark photoproduction is introduced and the charm fragmentation into observable D^* mesons is considered.

Furthermore jet algorithms are introduced along with D^* +jet pairs where the jet does not contain the D^* meson. Finally it is explained how D^* +jet quantities are related to various features of the charm production mechanism and how tests of theoretical calculations can be done.

1.1 Electron-Proton Scattering at HERA

At HERA protons and electrons (or positrons¹) collide at energies of $E_p = 920$ GeV and $E_e = 27.6$ GeV. They interact by the exchange of the virtual gauge bosons of the electro-weak force. The process is called neutral current interaction (NC) if a neutral boson, a photon γ or a Z^0 , is exchanged. In charged current interactions (CC) the charged W^\pm boson is exchanged. In this case the electron transforms into a neutrino. Both NC and CC processes are depicted in figure 1.1.

The following Lorentz invariant variables can be defined using the four-momenta of the incoming proton \mathbf{P} , the incoming electron \mathbf{k} and the scattered lepton \mathbf{k}' , respectively.

$$s = (\mathbf{k} + \mathbf{P})^2 \quad (1.1)$$

$$Q^2 = -\mathbf{q}^2 = -(\mathbf{k} - \mathbf{k}')^2 \quad (1.2)$$

$$x = \frac{Q^2}{2\mathbf{P} \cdot \mathbf{q}} \quad (1.3)$$

$$y = \frac{\mathbf{P} \cdot \mathbf{q}}{\mathbf{P} \cdot \mathbf{k}} \quad (1.4)$$

¹In the following positrons are implicitly included when electrons are mentioned.

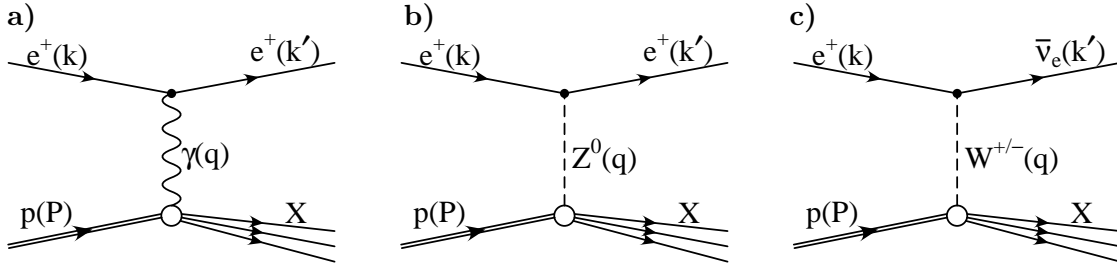


Figure 1.1: Neutral current (a,b) and charged current (c) positron-proton interactions in leading order. At HERA energies the proton generally is destroyed.

Neglecting the particle masses, the centre-of-mass energy is given by $\sqrt{s} = \sqrt{4E_p \cdot E_e} \sim 320$ GeV. The variable Q^2 is the negative four-momentum transfer squared from the lepton to the proton. In case of photon exchange it corresponds to the virtuality of the photon. In a frame with an infinite proton momentum the Bjorken scaling variable x can be identified (in the Quark Parton Model) with the fraction of the proton momentum that takes part in the interaction. In the proton rest frame the inelasticity y is the relative energy loss of the scattered lepton. Only three of these four variables are independent. Again neglecting the particle masses they fulfil

$$Q^2 = x \cdot y \cdot s. \quad (1.5)$$

Due to their large mass the Z^0 and the W^\pm exchange can be safely neglected for $Q^2 < 1000$ GeV². The differential neutral current cross section as a function of x and Q^2 can be calculated in Quantum Electrodynamics (QED) without taking into account the weak interaction,

$$\frac{d^2\sigma(e^\pm p \rightarrow e^\pm X)}{dx dQ^2} = \frac{4\pi\alpha^2}{xQ^4} \cdot \left[y^2 x F_1(x, Q^2) + (1-y) \cdot F_2(x, Q^2) \right]. \quad (1.6)$$

Here α is the electromagnetic coupling constant. The structure functions $F_1(x, Q^2)$ and $F_2(x, Q^2)$ parametrise the interaction of the exchanged photon with the proton without any knowledge of the nature of the interaction. Introducing the longitudinal structure function

$$F_L = F_2 - 2xF_1, \quad (1.7)$$

which is related to the exchange of a longitudinally polarised photon, eq. 1.6 can be written as

$$\frac{d^2\sigma(e^\pm p \rightarrow e^\pm X)}{dx dQ^2} = \frac{2\pi\alpha^2}{xQ^4} \cdot \left[(1 + (1-y)^2) \cdot F_2(x, Q^2) - y^2 \cdot F_L(x, Q^2) \right]. \quad (1.8)$$

The contribution from F_L is kinematically suppressed compared to F_2 except for very large inelasticities y and can be neglected elsewhere since it is smaller than F_2 (eq. 1.7).

1.2 Factorisation and Parton Evolution

In the naive Quark Parton Model (QPM), assuming the proton to consist statically of quarks and antiquarks, the structure function $F_2(x, Q^2)$ does not depend on Q^2 and eval-

uates as

$$F_2(x) = x \sum_i e_i^2 \cdot f_i(x). \quad (1.9)$$

The sum runs over all (anti-)quark flavours i with their electric charge e_i . The quark density $f_i(x)$ denotes the probability to find a quark i with the momentum fraction x in the proton.

In Quantum Chromodynamics (QCD) the quarks in the proton radiate gluons ($q \rightarrow qg$) and the gluons themselves can radiate further gluons ($g \rightarrow gg$) or split into quark-antiquark pairs ($g \rightarrow q\bar{q}$). The calculation of these radiations and splittings in perturbative QCD (pQCD) encounters difficulties. They are related to divergent integrals, e.g. for collinear gluon radiation. The solution is to introduce a cut-off scale μ_f , the factorisation scale, and to absorb the divergencies in parton density functions $f_i(x, \mu_f^2)$. If μ_f is large enough, $\mu_f \gg \Lambda_{QCD}$, reliable pQCD calculations are possible.

Also ultra violet divergencies occur in pQCD. They are absorbed into the running of the strong coupling constant $\alpha_s(\mu_r^2)$ which depends on the renormalisation scale $\mu_r \gg \Lambda_{QCD}$. At a scale $\mu_r = \Lambda_{QCD}$ the coupling α_s diverges and the perturbative expansion cannot converge. $\Lambda_{QCD} \approx 200$ MeV has been determined experimentally.

The absorption of the divergencies into the running of α_s and the scale dependence of the parton densities lead to a factorisation of the cross sections,

$$d\sigma(ep \rightarrow eX) = \sum_{i \in p} \int_0^1 dx f_i(x, \mu_f^2) \cdot d\hat{\sigma}_i(\hat{s}, \alpha_s(\mu_r^2), \mu_r, \mu_f). \quad (1.10)$$

Here $\hat{\sigma}_i$ is the perturbatively calculable partonic cross section and $\sqrt{\hat{s}}$ is the centre-of-mass energy of the partonic system. The parton density function (PDF) $f_i(x, \mu_f^2)$ of the parton i in the proton is universal and independent of the process calculated in pQCD, according to the factorisation theorem. The PDFs depend on a factorisation scheme, e.g. the DIS scheme or the $\overline{\text{MS}}$ scheme, and the calculation of $\hat{\sigma}_i$ has to adapt to the scheme used for the PDFs.

Although pQCD does not predict $f_i(x, \mu_f^2)$, it does predict the evolution to any scale $\mu_f > \mu_0$ once $f_i(x, \mu_0^2)$ is known at the starting scale μ_0 . In fact the PDFs are obtained by fitting their input distribution at the starting scale μ_0 such that after the evolution $F_2(x, Q^2)$ data from HERA and fixed target experiments are described. Here Q^2 is the relevant scale and $\mu_f^2 = Q^2$ is used. The evolution equations are derived considering the possible gluon radiation and gluon splitting processes. Such processes can occur several times which can lead e.g. to a gluon ladder as shown in figure 1.2.

Contributions from an arbitrary number of radiations have to be summed. Different assumptions about the consecutive longitudinal momentum fractions x_i , the transverse momenta $k_{t,i}$ which are related to the virtualities k_i^2 , and the radiation angles θ_i result in different approaches to the determination of parton density functions. The DGLAP, BFKL and CCFM approaches will be briefly described in the following.

DGLAP The DGLAP approach [11–14] is the most common to describe the parton evolution. The main approximation is that the transverse momenta k_t during consecutive gluon radiation are strongly ordered, i. e. $k_{t,i}^2 \gg k_{t,i-1}^2$. Furthermore the longitudinal momenta $x_i \mathbf{P}$ are supposed to be larger than the transverse momenta which is valid

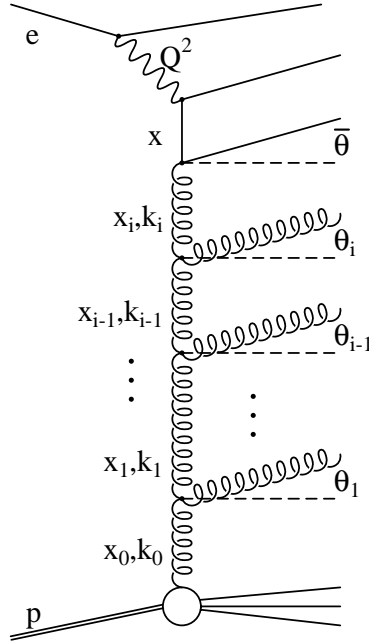


Figure 1.2: *General gluon ladder with the momentum fractions x_i , the virtualities k_i^2 and emission angles θ_i .*

for not too small x . Then the virtualities k_i^2 (related to $k_{t,i}^2$) before splitting can be neglected compared to k_{i+1}^2 after splitting and compared to the factorisation scale μ_f^2 . The calculation of the splitting functions and the partonic cross section $\hat{\sigma}$ can thus be done on-shell.

Factorisation within these approximations is called *collinear* factorisation since the k_t -dependence of the parton densities is integrated out. The picture presented so far (e. g. eq. 1.10) followed this approach.

BFKL At small x the collinear DGLAP ansatz is not appropriate. In the BFKL approach [15, 16] with $z_i = x_i/x_{i-1} \ll 1$ the longitudinal momenta are strongly ordered whereas the transverse momenta k_t are free. They can be of the same order of magnitude as the longitudinal momenta $x_i \mathbf{P}$. Since this approximation is valid only for small x , only gluons have to be taken into account in the evolution and the relevant proton momentum fraction of the gluon x_g corresponds to x_i in figure 1.2. The gluon density function now depends on k_t , $\mathcal{F}(x_g, k_t^2)$. Since $k_t \neq 0$ is considered in all steps of the calculation, the partonic cross section $\hat{\sigma}$ has to be taken off-mass-shell. The cross section can still be written in a factorised form, but now involving the k_t -dependence (k_t -factorisation).

CCFM The parton evolution according to CCFM [17–20] is an attempt of a unified description both for small and large x . Instead of ordering the gluon ladder in k_t or z , colour coherence effects motivate the approximation of an ordering in q , a quantity related to the angle θ of gluon emission. Similar to BFKL only gluons are taken into account in the parton evolution. The gluon density function $\mathcal{A}(x_g, k_t^2, \mu_f^2)$ is more

complicated and depends on k_t and the factorisation scale μ_f . The latter is related to the maximum angle \bar{q}_t possible for any emission. Also CCFM takes into account non-vanishing k_t , applying k_t -factorisation.

It has to be kept in mind that the different kinds of obtained PDFs are no physical observables in contrast to cross sections and structure functions.

The DGLAP approach has been proven to describe the structure function measurements at HERA [21, 22] successfully down to the smallest accessible x . Indications for the need of k_t -factorisation have been found so far only when considering the description of the hadronic final state at small x , e. g. for jets at large pseudorapidities $\eta = -\ln(\tan(\theta/2))$ [23].² Also heavy quark production can be affected since relatively small x -values around 10^{-3} are reached.

1.3 Photoproduction at HERA

If the virtuality Q^2 of the exchanged photon is small, it is almost real. The electron is scattered under a small angle and can be seen as the source of real photons. Experimentally photoproduction at HERA is defined by the electron being scattered into the beam pipe such that it escapes the detection in the main detector. This defines the kinematic region of photoproduction to be $Q^2 < 1 \text{ GeV}^2$, in contrast to deep inelastic scattering (DIS) with $Q^2 > 1 \text{ GeV}^2$. Since the cross section is proportional to $1/Q^4$ (eq. 1.6), photoproduction dominates the total electron-proton cross section.

The centre-of-mass energy $W_{\gamma p}$ of the photon-proton system amounts to

$$W_{\gamma p}^2 = (\mathbf{q} + \mathbf{P})^2 = y \cdot s - Q^2 \approx y \cdot s \quad (1.11)$$

where again \mathbf{P} is the proton and \mathbf{q} the photon four-momentum. For photoproduction at high centre-of-mass energies $\sqrt{s} \sim 320 \text{ GeV}$, Q^2 is negligible. The energy of the photon “beam” differs from event to event, depending on the inelasticity y which corresponds to the fraction of the energy of the incoming electron carried by the photon. The flux of photons with the energy fraction y and up to a virtuality Q_{max}^2 can be calculated using the Weizsäcker-Williams approximation

$$f_\gamma(y, Q_{max}^2) dy = \frac{\alpha}{2\pi} \left[\frac{1 + (1-y)^2}{y} \log\left(\frac{Q_{max}^2}{Q_{min}^2}\right) - 2m_e^2 y \left(\frac{1}{Q_{min}^2} - \frac{1}{Q_{max}^2}\right) \right] dy. \quad (1.12)$$

The fine structure constant is denoted as α and $Q_{min}^2 = \frac{m_e^2 y}{1-y}$ is the lower kinematic limit.

The quasi real photon can fluctuate into a quark-antiquark pair before the perturbatively calculable hard interaction. The quark-antiquark pair is subject to gluon radiation and gluon splitting like partons in a hadron. Thus the photon acquires a hadronic structure and parton density functions can be determined.

If a parton from the photon fluctuation takes part in the hard interaction, the process is called *resolved* photoproduction in contrast to *direct* photoproduction where the photon as a whole interacts. Both cases are sketched in leading order in figure 1.3. At next-to-leading order (NLO) there is no unique distinction between direct and resolved processes.

²The pseudorapidity η is an approximation of the rapidity $\hat{y} = \frac{1}{2} \ln\left(\frac{E+p_z}{E-p_z}\right)$. Both are identical for massless particles with $E = p$.

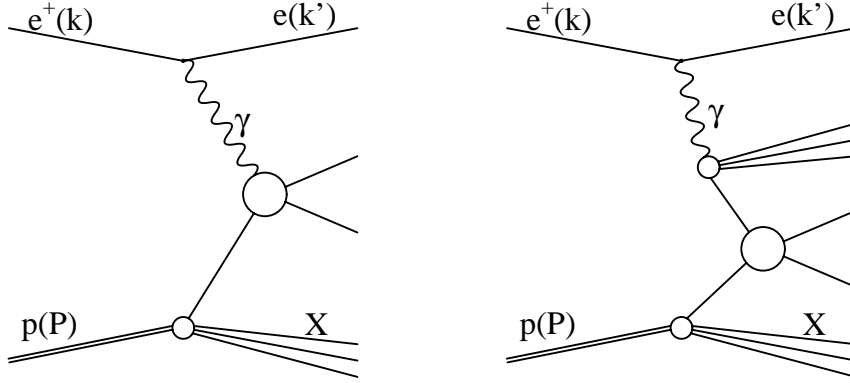


Figure 1.3: *Direct* (left) and *resolved* (right) photoproduction in leading order.

For example the splitting of the photon into a quark-antiquark pair ($\gamma \rightarrow q\bar{q}$) parametrised in the photon density followed by a leading order process $qg \rightarrow qg$ leads to the same final state as the NLO photon-gluon fusion process $\gamma g \rightarrow q\bar{q}g$. Thus only the sum of direct and resolved photoproduction is a physical observable.

The cross section calculation in photoproduction is assumed to factorise into the cross section $\hat{\sigma}_{ij}$ between the partons i and j , the parton densities in the proton $f_{i/p}$ and the parton density in the photon $f_{j/\gamma}$,

$$d\sigma_{\gamma p} = \sum_{i \in p} \sum_{j \in \gamma} \int_0^1 \int_0^1 dx_p dx_\gamma f_{i/p}(x_p, \mu_f^2) \cdot f_{j/\gamma}(x_\gamma, \nu_f^2) \cdot d\hat{\sigma}_{ij}(\hat{s}, \alpha_s(\mu_r^2), \mu_r, \mu_f, \nu_f). \quad (1.13)$$

Here μ_f and ν_f are the factorisation scales on the proton and on the photon side, respectively. For direct photoproduction the parton j in the photon γ is the photon itself and the momentum fraction x_γ is one.

1.4 Photoproduction of D^* Mesons

In this analysis charged D^* mesons³ are used to tag events with charm or anticharm quarks. Therefore this section will first describe how charm or, more generally, heavy quarks are produced in photon-proton collisions at HERA. Since bare quarks cannot be observed due to confinement in QCD, they must fragment into hadrons like the D^* meson. The transition from partons to hadrons and the main theoretical concepts to describe this fragmentation process will be discussed in the second part of this section.

1.4.1 Heavy Quark Production

Heavy quark production in the context of this thesis always means open charm and beauty production in pairs of quarks and antiquarks. Open charm production means that charm and anticharm are not bound in a single hadron as is the case e.g. in the J/Ψ meson.

³ $D^{*\pm}$ mesons with positive and negative charge are not treated separately. Therefore “ D^* meson” denotes both charged mesons throughout this thesis.

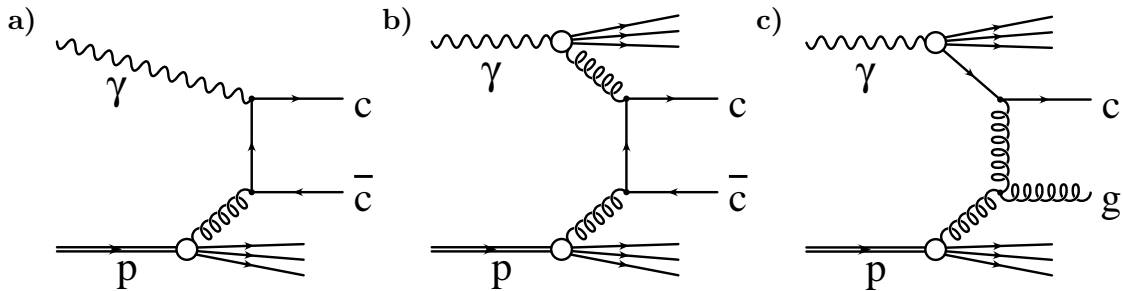


Figure 1.4: *Leading order diagrams of charm production in direct (a) and resolved (b) photon-gluon fusion and in charm excitation (c).*

The top quark is too heavy to be pair-produced at HERA, $2 \cdot m_t > \sqrt{s}$.⁴ Thus for top quarks the dominant standard model production mechanism is single top production via W^\pm exchange which has a very low cross section.

The advantage of considering heavy quark production is that the heavy quark mass always provides a hard scale $m_{\text{HQ}} \gg \Lambda_{\text{QCD}}$ and perturbative QCD calculations are possible down to very low Q^2 or transverse momenta p_t . On the other hand it complicates the calculation if at least one of these additional scales is present [24]. Therefore heavy quark production is an excellent testing ground of perturbative QCD.

The cross section for beauty quarks is about two orders of magnitude smaller than for charm quarks due to their larger mass, $m_b \approx 4.75$ GeV compared to $m_c \approx 1.5$ GeV, and their smaller charge, $|q_b| = 1/3$ versus $|q_c| = 2/3$. A further consequence of the larger beauty mass is that perturbative QCD calculations are expected to be more reliable since the mass provides a larger scale. The larger scale results in a smaller coupling constant α_s leading to a faster convergence of the perturbative expansion.

The first H1 measurement of D^* meson cross sections [25] indicated that photon-gluon fusion (PGF) shown in figure 1.4a) is the dominant charm production process in DIS for $Q^2 > 10$ GeV². A recent ZEUS measurement of dijet angular distributions in charm events [8] indicates that in photoproduction a sizeable contribution to the cross section originates from processes like the one shown in figure 1.4c). In leading order collinear factorisation these processes are treated as charm *excitation*, i. e. resolved processes where a charm quark from the photon side interacts with a gluon from the proton. The leading order picture given in the ZEUS analysis is supported by very recent massless NLO calculations [26]. Gluon splitting $g \rightarrow q\bar{q}$ in the fragmentation as a source of heavy quark production is negligible at HERA due to the large quark masses.

Chapter 2 introduces different leading and next-to-leading order calculations which the data of this analysis will be compared to, and their different approaches to handle the multi-scale problem present in heavy flavour production.

1.4.2 Fragmentation

About 23.5% of the produced charm quarks can be observed as D^* mesons as has been measured in electron-positron collisions [27]. The transition from coloured partons to

⁴Throughout this thesis natural units are used with $c = 1$. As a consequence factors of c are dropped and eV is the unit of energy, momentum and mass.

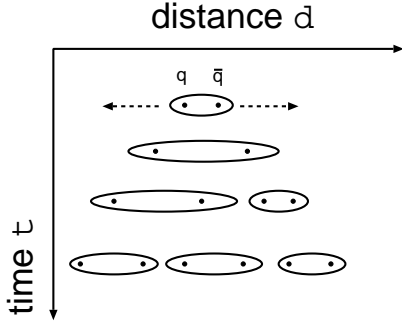


Figure 1.5: *Break up of colour strings according to the Lund model.*

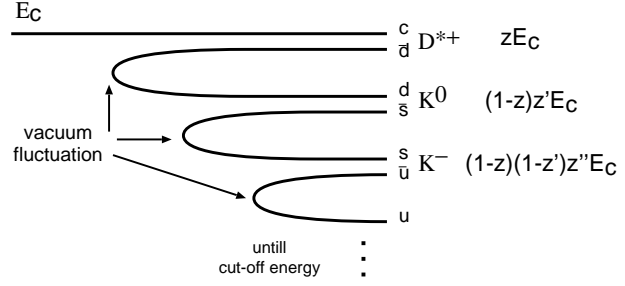


Figure 1.6: *Creation of quark-antiquark pairs in independent fragmentation.*

colourless, observable hadrons is called fragmentation. Sometimes the process is more precisely divided into the fragmentation process, meaning radiation of the outgoing partons of the hard process until their virtuality is small, and hadronisation, meaning the transition of the partons into hadrons after radiation. The first step is calculable in perturbative QCD, using parton showering similar to the evolution of the incoming partons. For the second step non-perturbative models must be used. This section introduces the fragmentation models used in the theoretical calculations that will be introduced in chapter 2.

One of the most successful fragmentation models is the Lund string model [28]. It is usually applied after the perturbative final state parton showering in leading order calculations. Colour strings connect quarks and antiquarks that move apart from each other. Due to the QCD potential the energy stored in the string increases with increasing distance. The string breaks up producing a quark-antiquark pair if the energy is large enough, depicted in figure 1.5. Gluons create kinks in the strings.

A much simpler approach for charm and beauty quarks is the independent fragmentation with the Peterson fragmentation function [29]. In this thesis it is implemented in massive NLO calculations (cf. section 2.3). The basic idea is that the heavy quark picks up a light antiquark from a fluctuation of the vacuum into a quark-antiquark pair. The hadron formed by the heavy quark and the light antiquark loses energy with respect to the bare heavy quark. Figure 1.6 shows the principle of the independent fragmentation if extended to a cascade of vacuum fluctuations also for the remaining light quarks. The process is continued until a cut-off energy is reached.

The relation between the heavy quark and hadron energies is expressed by a fragmentation function $D_Q^H(z)$. It denotes the probability of the heavy hadron H to retain the energy fraction⁵ $z = E_H/E_Q$ of the heavy quark Q . The Peterson fragmentation function [29]

$$D_Q^H(z) = \frac{N_A}{z} \left(1 - \frac{1}{z} - \frac{\epsilon_Q}{1-z} \right) \quad (1.14)$$

is deduced considering the energies before and after the fragmentation. Although the parameter $\epsilon_Q = m_q^2/m_Q^2$ relates the masses of the heavy quark and the light antiquark, in fact it is adjusted to describe the data. It is smaller (meaning harder fragmentation)

⁵The exact definition of z depends on the details of the implementation.

if following an NLO calculation compared to following a leading order calculation since in NLO the possibility of one gluon radiation is already included. N_A normalises the fragmentation function summing over all possible hadrons H and integrating over all z . A different parametrisation of heavy quark fragmentation is the one according to Kartvelishvili [30].

The independent fragmentation model is not Lorentz invariant and needs an *ad hoc* treatment of the remaining light quark and its colour. In general it does not describe the full hadronic final state, but the Peterson function reproduces the heavy quark fragmentation function quite well. Thus the Peterson fragmentation function is sometimes used in conjunction with the Lund string model, e. g. in the leading order calculations compared to data in this thesis (cf. section 2.1).

Fragmentation can also be described by fragmentation functions constructed like the PDFs of hadrons. They depend on a scale μ^{fr} and can be evolved according to perturbative evolution equations (here mainly DGLAP with collinear factorisation is used), but now from higher scales down to a small scale μ_0^{fr} . This evolution is responsible for the so called final-state parton shower already mentioned in conjunction with the Lund model. The NLO calculation in the zero-mass variable-flavour-number scheme (cf. section 2.2) apply fragmentation functions derived in [31]. Their functional form at the scale μ_0^{fr} is again chosen to be Peterson-like.

1.5 Jets and Jet Algorithms

From a simple point of view a jet is just a bunch of particles which move into almost the same direction. This bunch is related to a parton produced in the hard interaction which splits into several hadrons in the fragmentation and subsequent particle decay. But the picture gets less clear considering events with more or very broad bunches. How far away from each other are sub-bunches to be split into two independent jets? How close should two bunches be to be combined into one jet instead of two? To get a clear definition, a well defined jet algorithm is applied. The algorithm groups the particles and defines the four-momenta of the resulting jets.

Such an algorithm is also needed to compare the data with QCD calculations that do not provide a set of colourless objects, but only a few coloured partons, usually two or three. Figure 1.7 illustrates how this is done. In the data the algorithm is applied to the measured objects which are a combination of tracks and clusters as will be described in section 3.7. In the parton level calculation the algorithm is applied to the partons, e. g. two quarks and a gluon. Here the algorithm mainly decides whether the radiated gluon has to be merged with one of the quarks.

The connection between the data and the calculation is achieved using a simulation that provides a full set of generated colourless particles (“hadron level”), tracks and clusters resulting from the simulated interaction of these particles with the detector (“detector level”) and the coloured partons before the hadronisation (“parton level”). The jet algorithm is applied to all three sets of objects and an unfolding of the detector effects, e. g. inefficiencies or energy smearing, as well as an unfolding of the effect of the hadronisation is possible. Thus a comparison of data and theory at the “hadron level” can be achieved.

A good jet algorithm features a good correlation between the parton and hadron jets and is *infrared* and *collinear* safe. Infrared and collinear safety mean that the output

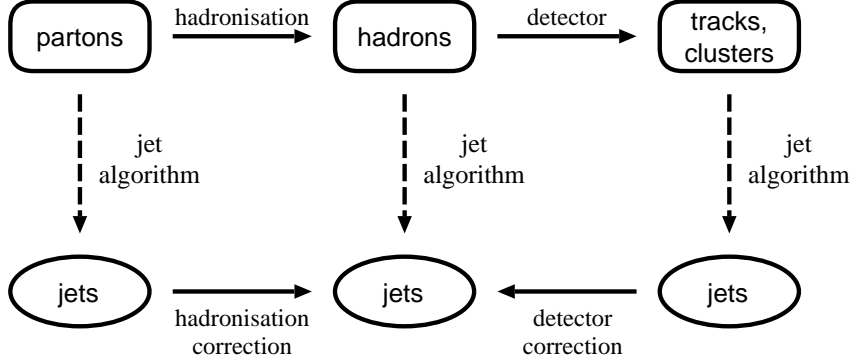


Figure 1.7: Application of a jet algorithm on different objects and its use to compare detected data with parton level calculations.

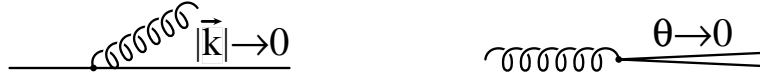


Figure 1.8: Infrared radiation (left) and collinear splitting (right).

of the algorithm, i.e. the set of jets and their four-momenta, must not be changed by processes like radiation of a soft gluon or collinear splitting as depicted in figure 1.8.

The divergent cross section contribution of a process with infrared radiation $|\vec{k}| \rightarrow 0$ or collinear branching $\theta \rightarrow 0$, cancels in NLO calculations with virtual corrections that produce the same final state as a similar process without the radiation. Diagrams of involved cross section contributions are illustrated in figure 1.9. For $|\vec{k}| \rightarrow 0$ and $\theta \rightarrow 0$ they must contribute to the same jet configuration since the result of the jet cross section calculation must not depend on the cut-off parameter chosen to avoid the divergencies.

In this analysis the inclusive k_t -jet algorithm [32] is applied using the ΔR -resolution and the p_t -weighted recombination scheme. The algorithm will be explained in detail

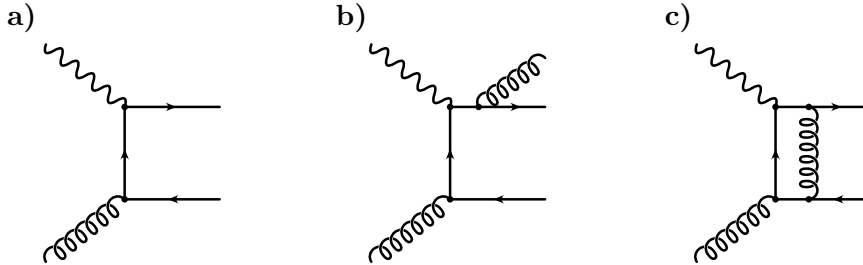


Figure 1.9: Feynman diagrams of leading order PGF (a), PGF with a radiated gluon (b) and PGF with a virtual correction (c). The interference of a) and c) belongs to the NLO contributions and leads to a negative contribution to the scattering amplitude. Divergencies of b) cancel with the negative divergencies of this interference.

below. It is infrared and collinear safe and – neglecting particle masses – invariant under Lorentz boosts along the z -axis. Since in photoproduction the centre-of-mass system of the hadronic system can be transformed into the laboratory frame by a longitudinal Lorentz boost along the z -axis, the jet algorithm is applied in the laboratory frame.

The algorithm successively combines objects, so-called protojets, if they are close to each other in pseudorapidity η and azimuth angle ϕ . The distance in η - ϕ space (ΔR) is weighted with their transverse momenta p_t such that low energetic objects are combined first. If no other protojet is close, the protojet is considered as a jet. The algorithm starts with all input objects as protojets and an iterative procedure follows⁶:

1. For each protojet i and each pair of protojets ij the distances

$$d_i = p_{t,i}^2 \quad (1.15)$$

$$d_{ij} = \min(p_{t,i}^2, p_{t,j}^2) \cdot [(\eta_i - \eta_j)^2 + (\phi_i - \phi_j)^2] / R_0^2 \quad (1.16)$$

are calculated. R_0 is related to the opening angle of the jets. In this analysis $R_0 = 1$ is chosen as usual.

2. The minimum d_{min} of all d_i and d_{ij} is found.
3. If d_{min} is a d_{ij} , the protojets i and j are replaced by a new protojet k with the merged kinematic quantities

$$p_{t,k} = p_{t,i} + p_{t,j}, \quad (1.17)$$

$$\eta_k = \frac{p_{t,i} \cdot \eta_i + p_{t,j} \cdot \eta_j}{p_{t,k}}, \quad (1.18)$$

$$\phi_k = \frac{p_{t,i} \cdot \phi_i + p_{t,j} \cdot \phi_j}{p_{t,k}}. \quad (1.19)$$

4. If d_{min} is a d_i , the protojet i is considered as a final jet and is removed from the list of protojets.
5. If there are protojets left, the procedure goes on with step 1.

Particle and protojet masses are neglected in all steps, resulting in massless jets. A short overview of different recombination and resolution schemes for the inclusive k_t -jet algorithm is given in [33].

1.6 D^* +Jet Double Tag

The D^* meson is used to select charm production and to approximate the kinematics of the produced charm or anticharm quark. To achieve a more detailed understanding of the charm production mechanism, it is desirable to investigate the hadronic final state. It is of special interest to reconstruct a second object that is related to the production process.

The strategy of this analysis is to find a jet not containing the D^* meson. This is described here, followed by presenting combined D^* +jet quantities which are sensitive to QCD effects related to higher orders in pQCD or to initial k_t .

⁶All equations considering the azimuth ϕ are symbolic, the rotational behaviour of ϕ is treated properly.

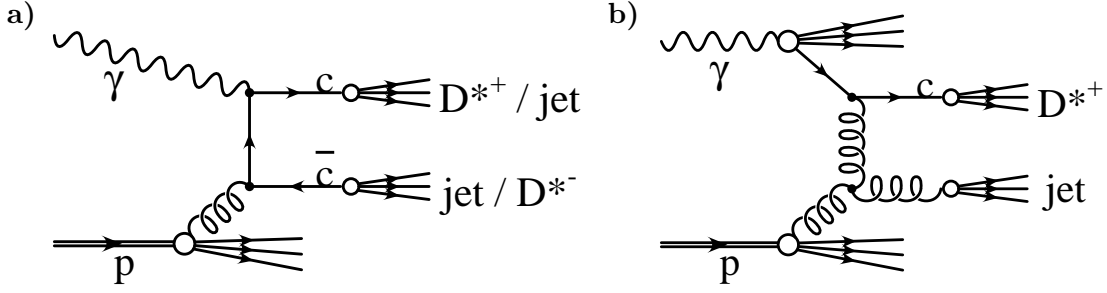


Figure 1.10: *Leading order photon-proton processes and possible reconstruction via a D^* +jet pair, photon-gluon fusion (a) and charm excitation in the photon (b).*

1.6.1 The Jet as Second Tag

Reconstruction of a second D^* meson is statistically very limited due to the small branching ratio of the used decay chain $c \rightarrow D^* \rightarrow D^0 \pi_s \rightarrow K \pi \pi_s$, cf. section 4.1. In [9] the second heavy quark of the photon-gluon fusion is reconstructed by identification of a muon track coming from the semileptonic decay of a heavy hadron. There the correlation between the D^* meson and the muon is used to separate charm and beauty, but the statistics is very limited.

In this analysis a more inclusive ansatz is chosen. Instead of identifying a second heavy quark or hadron by its decay products, a second hard outgoing parton is reconstructed by a jet. Figure 1.10 shows the dominant leading-order diagrams of charm production in collinear factorisation, direct photon-gluon fusion and charm excitation, and illustrates what kind of partons can be tagged by the D^* meson and by a jet which does not contain the D^* meson.

The jet is supposed to tag an object which is not yet tagged by the D^* and therefore should not contain the D^* meson. In case of direct photoproduction, figure 1.10a), there are two possibilities. The charm can be tagged by a D^{*+} meson and the anticharm by the jet or – vice versa – the charm is tagged by the jet and the anticharm by a D^{*-} meson. In case of charm excitation, figure 1.10b), there is only one possibility, at least as long as the second (anti-)charm quark in the photon remnant is not scattered into the central detector region.

It is not possible to distinguish whether the hard object reconstructed by the jet is a heavy or light quark or even a gluon. Therefore different processes like direct photoproduction and charm excitation cannot be distinguished. The advantage using the jet tag is the much larger statistics compared to (semi-)exclusive reconstruction for two hard final state partons.

In the following the term “jet” always designates a jet *not* containing the D^* meson, in contrast to jets containing a D^* meson which are denoted as “ D^* -jet”. “ D^* +jet” means a pair of a D^* meson and a (non- D^* -) jet.

1.6.2 Combined D^* +Jet Quantities

The measurement of a D^* +jet pair gives the possibility to test several quantities which are sensitive to the production mechanism. The assumption is that the D^* meson and the jet approximate the kinematics of a charm or anticharm quark and another parton, be it

the other (anti-)charm, a light quark or a gluon. The quantities characterising the D^* +jet system are the ϕ -distance $\Delta\phi(D^*, \text{jet})$, the transverse momentum $p_t(D^*+\text{jet})$ and the invariant mass $m(D^*+\text{jet})$ of the D^* +jet pair, the pseudorapidity difference $\eta(D^*) - \eta(\text{jet})$ and $x_\gamma(D^*+\text{jet})$, which is related to the momentum fraction of the photon carried by the parton entering the hard process.

$\Delta\phi(D^*, \text{jet})$ and $p_t(D^*+\text{jet})$

In the centre-of-mass system of the interacting partons the two outgoing partons of a $2 \rightarrow 2$ process are back-to-back. Assuming that the interacting partons do not obtain a transverse momentum k_t with respect to the colliding photon and proton, in photoproduction the difference between the laboratory frame and the frame of the partonic centre-of-mass system is a longitudinal Lorentz boost along the beam axis z . The longitudinal boost does not change the topology in the plane transverse to the boost axis.

Therefore the partons are still back-to-back in this plane, i. e. $\Delta\phi = 180^\circ$, and balanced in transverse momentum, $\vec{p}_t(1) = -\vec{p}_t(2) \Rightarrow |\vec{p}_t(1+2)| = 0$. Initial transverse momenta k_t of the incoming partons and higher order effects like gluon radiation distort these correlations. Therefore the difference in ϕ between the D^* and the jet

$$\Delta\phi(D^*, \text{jet}) = \begin{cases} |\phi(D^*) - \phi(\text{jet})| & : |\phi(D^*) - \phi(\text{jet})| < 180^\circ \\ 360^\circ - |\phi(D^*) - \phi(\text{jet})| & : |\phi(D^*) - \phi(\text{jet})| > 180^\circ \end{cases} \quad (1.20)$$

and the transverse momentum of the D^* +jet pair

$$p_t(D^*+\text{jet}) = \sqrt{(p_x(D^*) + p_x(\text{jet}))^2 + (p_y(D^*) + p_y(\text{jet}))^2} \quad (1.21)$$

test the correct description of the higher order or k_t -effects in the calculations. However, especially the transverse momentum $p_t(D^*+\text{jet})$ is smeared by the fragmentation of charm into the D^* meson leading to values different from zero, even for leading order processes that are perfectly back-to-back in ϕ .

$m(D^*+\text{jet})$

The invariant mass of the D^* +jet pair

$$m(D^*+\text{jet}) = \sqrt{(E(D^*) + E(\text{jet}))^2 - (\vec{p}(D^*) + \vec{p}(\text{jet}))^2} \quad (1.22)$$

is an approximation of the invariant mass of the tagged partonic system. Here E and \vec{p} denote the energy and the three-momenta of the D^* and the jet where $E(\text{jet}) = |\vec{p}(\text{jet})|$ for a massless jet algorithm like in this thesis. In leading order $m(D^*+\text{jet})$ corresponds to the centre-of-mass energy of the incoming partons $\sqrt{\hat{s}}$.

$x_\gamma(D^*+\text{jet})$

The quantity x_γ denotes which fraction of the longitudinal photon momentum takes part in the hard interaction, in analogy to the proton momentum fraction x_g carried by the gluon in photon-gluon fusion.

In photoproduction using energy and momentum conservation x_γ can be calculated as

$$x_\gamma = \frac{E_{t,1} \exp(-\hat{y}_1) + E_{t,2} \exp(-\hat{y}_2)}{2E_\gamma} \quad (1.23)$$

in a $2 \rightarrow 2$ process, e.g. photon-gluon fusion, neglecting the proton mass and initial transverse momenta k_t . $E_{t,i} = \sqrt{E_i^2 - p_{z,i}^2}$ are the transverse energies and $\hat{y}_i = 1/2 \ln[(E_i + p_{z,i})/(E_i - p_{z,i})]$ denote the rapidities of the outgoing partons. E_γ is the energy of the photon and is in photoproduction directly related to the electron beam energy E_e and the inelasticity y , $E_\gamma = yE_e$. This leads to $x_\gamma = 1$ in direct and $x_\gamma < 1$ in resolved processes. For processes calculated in k_t -factorisation x_γ can be smaller than 1 even without the inclusion of a resolved component.

Using the sum over all hadronic final state (HFS) particles $2yE_e = \sum_{i \in \text{HFS}} (E_i - p_{z,i})$ [34] and substituting $E_t \exp(-\hat{y})$ by $E - p_z$ results in

$$x_\gamma(D^*+\text{jet}) = \frac{\sum_{i \in D^*} (E - p_z)_i + \sum_{j \in \text{jet}} (E - p_z)_j}{\sum_{k \in \text{HFS}} (E - p_z)_k} \quad (1.24)$$

if the partons are approximated by the $D^*+\text{jet}$ pair or rather by the sum of their daughters. Using this definition of an observable quantity related to x_γ has the experimental advantage that $x_\gamma(D^*+\text{jet})$ is restricted to the physical range of $0 < x_\gamma \leq 1$ even for fluctuations in the measurement since the sums in the numerator are always a fraction of the sum in the denominator.

In the next-to-leading order parton level calculations the photon remnant is not accessible and the jet contains very often only one parton. Therefore a slightly different definition of x_γ is used on parton level,

$$x_\gamma(D^*+\text{jet}) = \frac{(E - p_z)_{D^*} + (E - p_z)_{\text{jet}}}{2yE_e}. \quad (1.25)$$

A disadvantage of $x_\gamma(D^*+\text{jet})$ compared to other x_γ definitions in charm events using two jets [8] is that it is convoluted with the $c \rightarrow D^*$ fragmentation leading to $x_\gamma(D^*+\text{jet}) < 1$ even for direct processes. But requiring only one jet increases the statistics and still resolved processes have on average significantly smaller $x_\gamma(D^*+\text{jet})$ than direct processes as will be shown.

$\eta(D^*) - \eta(\text{jet})$

Considering the D^* meson and the jet as approximations of the outgoing partons, the distribution of the pseudorapidity difference $\eta(D^*) - \eta(\text{jet})$ is in leading order sensitive to the relative contributions of the direct and resolved photon-gluon fusion, (figures 1.10a) and 1.4b), compared to charm excitation, figure 1.10b). In the latter case the jet originates from a gluon and the D^* is generally closer to the photon direction (negative pseudorapidities η) than the jet, leading to $\eta(D^*) - \eta(\text{jet}) < 0$ being preferred. In the direct process the D^* tag and the jet tag are symmetric apart from possibly different kinematical cuts.

Apart from charm excitation processes in leading order collinear factorisation, also hard gluon radiations can lead to an asymmetry. These radiations are possible in the final state parton shower, as NLO processes or due to k_t -unordered evolution of the initial parton ladder from the proton side in k_t -factorisation.

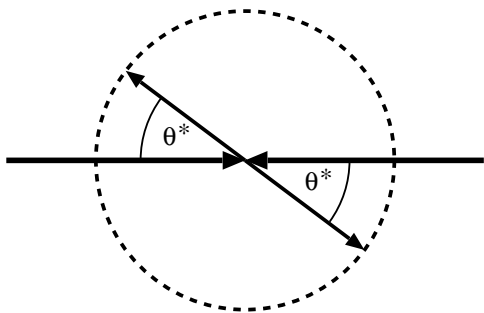


Figure 1.11: *The scattering angle θ^* in the partonic centre-of-mass system.*

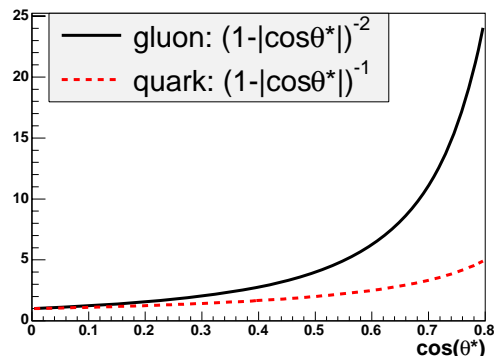


Figure 1.12: *The $\cos(\theta^*)$ distribution for spin- $\frac{1}{2}$ (quark) and spin-1 (gluon) propagators.*

The pseudorapidity difference $\eta(D^*) - \eta(\text{jet})$ is also related to the scattering angle θ^* between the collision axis and the outgoing partons in the partonic centre-of-mass system in a $2 \rightarrow 2$ process (figure 1.11),

$$\cos(\theta^*) = \tanh\left(\frac{\eta(D^*) - \eta(\text{jet})}{2}\right). \quad (1.26)$$

The $\cos(\theta^*)$ distribution depends on the nature of the propagator of the involved matrix element. For spin- $\frac{1}{2}$ propagators like the quark in the direct process the distribution rises like $(1 - |\cos(\theta^*)|)^{-1}$ for $|\cos(\theta^*)| \rightarrow 1$, e. g. $\theta^* \rightarrow 0$. For spin-1 propagators like in the case of the gluon in the charm excitation processes depicted in figure 1.10b) the distribution rises more strongly like $(1 - |\cos(\theta^*)|)^{-2}$ as indicated in figure 1.12.

The investigation of the $\cos(\theta^*)$ distribution in charmed dijet events [8] showed that a large fraction of the resolved contribution in leading order QCD has a gluon propagator and thus is due to charm excitation processes. This importance of charm compared to gluons originating from the photon is also seen in recent NLO calculations in the massless scheme [26].

In the present analysis $\cos(\theta^*)$ is not considered further since additional cuts are needed in order not to bias its distribution by the momentum and pseudorapidity cuts required for the D^* and the jet. The pseudorapidity difference $\eta(D^*) - \eta(\text{jet})$ itself will be examined since it is of its own interest as described above.

Chapter 2

QCD Calculations of D^* and $D^*+\text{Jet}$ Cross Sections

In this thesis measurements of D^* and $D^*+\text{jet}$ photoproduction cross sections are presented. QCD predictions will finally be compared to the measurements.

As described in section 1.2 there are different approaches for QCD calculations, collinear and k_t -factorisation. In collinear factorisation calculations in leading order and in next-to-leading order (NLO) are available whereas QCD predictions in k_t -factorisation have not yet been extended beyond leading order. However, k_t -factorisation implicitly contains contributions of terms that are of higher order in collinear factorisation, as nicely described in [9]. In leading order Monte Carlo simulations the calculation of the hard matrix element is usually supplemented with so-called parton showers to approximate higher order contributions. Recent theoretical developments established a procedure to match also NLO calculations with a parton shower [35,36], but such calculations are not available for HERA.

In the following different calculations will be considered in more detail. The leading order approach including parton showers will be expounded, both in collinear and k_t -factorisation. Then different NLO approaches are explained and the FMNR program is presented, a *massive* NLO calculation. Finally the contribution from beauty production is considered.

2.1 Leading Order Calculations with Parton Showers

Leading order QCD calculations are usually implemented as Monte Carlo event generators. In subsequent steps full final state events are generated. Differential cross section predictions follow from the distributions obtained from these events.

The generator steps are depicted in figure 2.1: The hard matrix element (ME) is calculated in leading order. Initial parton showers (PS) evolve the parton entering the hard process from the proton side and final parton showers simulate QCD radiation down to a cut-off scale. These perturbatively described phenomena are followed by the hadronisation of the gluons and quarks into observable mesons and baryons which is non-perturbative and has to be modelled.

In this analysis two Monte Carlo event generators are used, PYTHIA [37] and CASCADE [38, 39]. The cross section predictions of PYTHIA version 6.15 and CASCADE

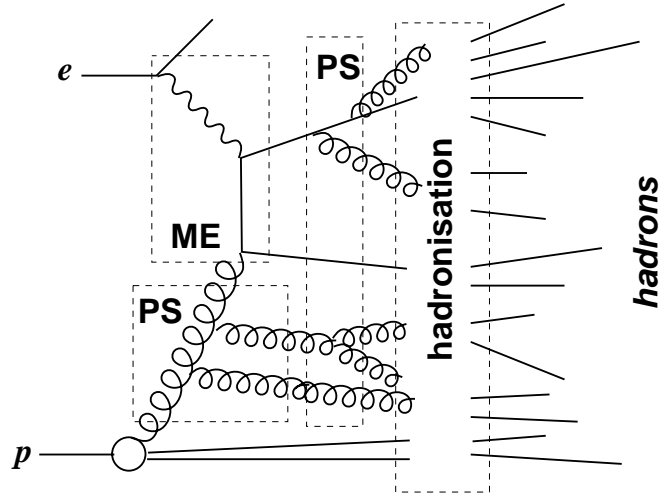


Figure 2.1: *Sketch of the subsequent steps of an event generator: Initial and final parton shower (PS), matrix element (ME) and hadronisation.*

version 1.20 [40] will be compared to the data. PYTHIA version 6.15 is used to determine the efficiency and acceptance corrections applied to the data. As a cross check these corrections will also be determined by CASCADE 1.00. Both generators use the PYTHIA implementation of the final parton shower and the hadronisation step. The partons are fragmented according to the Lund string fragmentation [28]. The heavy quark fragmentation is chosen to follow the Peterson fragmentation function [29] with the parameter $\epsilon_{pet} = 0.078$ for the $c \rightarrow D^*$ transition which is appropriate for a leading order matrix element.

PYTHIA and CASCADE differ significantly in the treatment of the matrix element and the initial parton shower. PYTHIA computes the matrix element and the initial parton shower in collinear factorisation, i. e. using the DGLAP evolution and an on-shell matrix element. Three different processes are generated separately and added afterwards: direct photon-gluon fusion, resolved processes with a light quark or a gluon from the photon and charm excitation processes where a charm quark from the photon enters the hard scatter (cf. figure 1.4). In the latter process the charm quark is treated as a massless parton like the light quarks whereas in the other processes the charm mass is set to $m_c = 1.5$ GeV. The cross section of the resolved processes with light partons from the photon is smaller by an order of magnitude in the visible range of this analysis ($p_t(D^*) > 2.0$ GeV, $|\eta(D^*)| < 1.5$, table 5.6) compared to the cross section of the other two processes. The parton density parametrisations used are CTEQ5L [41] for the proton and GRV-G LO [42] for the photon. Multiple interactions are incorporated in PYTHIA by default.

CASCADE uses k_t -factorisation. The initial parton cascade is evolved according to the CCFM equation, i. e. without ordering in k_t and considering only gluons. This leads to an unintegrated gluon density which in contrast to the integrated parton densities in collinear factorisation explicitly depends on k_t . Without the restriction of k_t ordering the virtuality of the incoming gluon cannot be neglected and the matrix element has to be calculated off-shell. Only direct photon-gluon fusion processes are taken into account, but without ordering in k_t some effects of charm excitation processes are implicitly included,

as illustrated in [9]. Multiple interactions are not treated in CASCADE.

For the CASCADE 1.20 calculations the renormalisation scale $\mu_r^2 = 4m_c^2 + p_t^2$ is chosen and the gluon density set A0 [43] is used. Since the renormalisation scale is an unphysical parameter, the full QCD calculation summing all orders of the perturbative expansion must not depend on its choice. The importance of higher order terms is estimated by using the sets A0+ and A0- instead which apply the renormalisation scale multiplied and divided by two, respectively. Separately the charm mass has been varied from the default value $m_c = 1.5$ GeV to $m_c = 1.3$ and $m_c = 1.7$ GeV. The largest deviations of these four calculations from the default set define the upper and lower bound of the uncertainties of the CASCADE calculation. In most regions of phase space considered in this analysis the mass variations have the largest effect.

The PYTHIA implementation of the hadronisation used in both generators leads to a hadronisation factor of $\mathcal{H}(c \rightarrow D^*) = 0.297$ whereas $\mathcal{H}(c \rightarrow D^*) = 0.235 \pm 0.007 \pm 0.007$ is obtained from measurements [27]. The branching ratio of D^* mesons in the analysed decay chain $D^{*\pm} \rightarrow D^0 \pi_s^\pm \rightarrow K^\mp \pi^\pm \pi_s^\pm$ is $\mathcal{BR}(D^* \rightarrow K\pi\pi) = 0.0250$ in the generators, but $\mathcal{BR}(D^* \rightarrow K\pi\pi) = 0.0257 \pm 0.0006$ is the measured world average [44]. Therefore D^* cross section predictions of PYTHIA and CASCADE will be multiplied with a correction factor f_{cor} when compared to the data to correct for these effects. For PYTHIA it is $f_{cor} = 0.813$, since only D^* mesons in the analysed decay have been generated, and for CASCADE it is $f_{cor} = 0.791$, correcting only $\mathcal{H}(c \rightarrow D^*)$.

2.2 Next-to-Leading Order Calculations

Different approaches have been followed in the literature to calculate charm photoproduction cross sections at next-to-leading order QCD in collinear factorisation. They differ mainly in the treatment of the charm mass by neglecting or resumming different higher order terms of the perturbative expansion series.

In the *massive* or *fixed-flavour-number* scheme [45,46] one assumes that only the gluon and the light quarks (u, d, s) are active flavours in the proton and in the (resolved) photon. The charm mass is explicitly taken into account, but it is assumed that the mass and the transverse momentum, i. e. the second hard scale involved, are of the same order. In this way terms $\propto \alpha_s \ln(p_t^2/m_c^2)$ are neglected and the theory should be applicable for $p_t \gtrsim m_c$ only. Details about *massive* NLO predictions by the FMNR program which will be compared to the data follow in section 2.3.

In the *zero-mass variable-flavour-number* scheme (ZMVFNS) the charm quark is treated as massless like the light flavours. In contrast to the massive scheme, the charm quark is considered also as an incoming parton of the hard matrix element, originating from the proton or the photon. Fragmentation of the charm quark into observable mesons is performed by a fragmentation function adopted to this scheme [31]. Since terms of the order m_c^2/p_t^2 are neglected, the predictions are expected to be reliable at large transverse momenta only.

Nevertheless, the cross sections obtained in this analysis will be compared with a massless calculation in this scheme [26,47]. The scales are chosen to be $\mu_r^2 = m_c^2 + p_t^2$ for the renormalisation and $\mu_f^2 = 4 \cdot (m_c^2 + p_t^2)$ for the factorisation with the charm mass $m_c = 1.5$ GeV.

The uncertainty of the calculation is estimated by considering the influence of varying

| ZMVFNS | Fragmentation | μ_f | μ_r | p -PDF | γ -PDF |
|---------------------|---------------|------------------|---------------|-------------|---------------|
| decreasing σ | BKK O [31] | $1.25 \cdot m_t$ | $2 \cdot m_t$ | MRST03 [48] | AFG04 [49] |
| default | | $2 \cdot m_t$ | m_t | | |
| increasing σ | | $4 \cdot m_t$ | m_t | | |

Table 2.1: Main parameters of the ZMVFNS next-to-leading order QCD calculation with their default settings and variations which lead to an increasing and decreasing prediction of the total visible cross section, respectively. The treatment of the charm fragmentation into D^* mesons, the factorisation and renormalisation scales μ_f and μ_r and the parton density parametrisations of the proton and the photon are given. The transverse mass is defined as $m_t = \sqrt{m_c^2 + p_t^2(D^*)}$ with the charm mass $m_c = 1.5$ GeV.

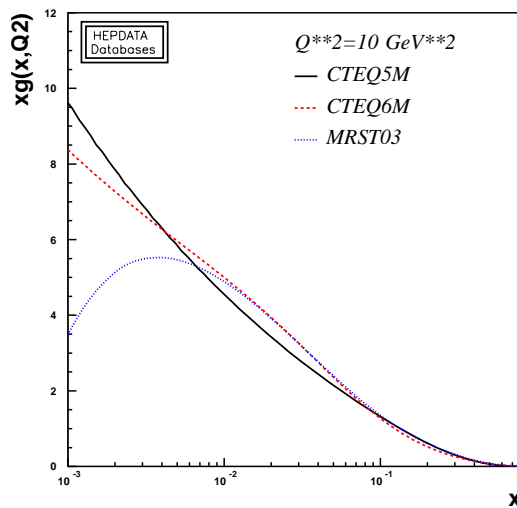


Figure 2.2: Gluon densities at a scale $\mu_f^2 = 10$ GeV². The CTEQ5M [41] and MRST03 [48] parametrisations are used in NLO calculations which will be compared to the data in this thesis. CTEQ6M [50] is given for reference only.

these scales. For this massless calculation a usual way is to multiply the scales with a factor 2 or 0.5. The largest deviations from the central choice obtained by all combinations of variations define the lower and upper bound of the uncertainties. Mostly these are the diagonal scale variations, i. e. factor 2 for μ_r combined with factor 0.5 for μ_f and vice versa. The lowest minimal transverse momentum in this analysis, $p_t(D^*) = 2$ GeV, would lead to scales smaller than the parton density parametrisations are applicable for and smaller than the perturbative expansion is expected to work with. Therefore here smaller variations are chosen. They are listed in table 2.1 with further details.

It has to be remarked that the MRST03 parton densities of the proton used in the ZMVFNS calculation differ from other parametrisations. Particularly the gluon density at lower scales and relatively small $x \approx 10^{-3}$ is lower than in other parametrisations as shown in figure 2.2. Indeed, calculations using CTEQ5M [41] instead, but all other parameters as

| FONLL | Fragmentation | $\mathcal{H}(c \rightarrow D^*)$ | μ_f | μ_r | p -PDF | γ -PDF |
|---------------------|-------------------------|----------------------------------|---------|-----------------|-------------|---------------|
| decreasing σ | Kartvelishvili [30, 54] | 0.235 | m_t | $2 \cdot m_t$ | CTEQ5M [41] | GRV [42] |
| default | | | m_t | m_t | | |
| increasing σ | | | m_t | $0.5 \cdot m_t$ | | |

Table 2.2: Main parameters of the FONLL next-to-leading order QCD calculations with their default settings and variations. The treatment of the charm fragmentation into D^* mesons, the charm hadronisation fraction, the factorisation and renormalisation scales μ_f and μ_r and the parton density parametrisations of the proton and the photon are given. The transverse mass is defined as $m_t = \sqrt{m_c^2 + p_{t,c}^2}$ with the charm mass $m_c = 1.5$ GeV.

for the central prediction, are approximately as large as the upper bound using MRST03.

As reviewed in [24], the conceptually most promising approach to calculate heavy quark cross sections is to combine the benefits of the massive and the massless scheme. In the FONLL [51, 52] approach the calculation at low momenta $p_t \approx m_c$ is effectively performed in the massive scheme and at high momenta in the massless scheme. A transition is defined to avoid double counting of common terms. A further *merged* approach compared to D^* photoproduction at HERA can be found in [53]. The inclusive differential $d\sigma/dp_t(D^*)$ cross section obtained in this analysis will be compared to a FONLL calculation. Table 2.2 shows the choice of the most important parameters.

2.3 The FMNR Program

An implementation of the massive next-to-leading order QCD calculations for heavy quark photoproduction [45, 46] has been made available to the H1 and ZEUS collaborations by the authors. The program is organised like an event generator such that it provides “events” containing kinematical information of either one heavy quark (single differential mode) or of both the heavy quark and antiquark and a possible third parton, a gluon or a light quark (double differential mode). Each event has to be taken into account with its weight which may be negative. These negative weights correspond to interference terms of leading order diagrams with virtual correction diagrams considered in next-to-leading order, cf. figure 1.9.

Two separate calculations have to be performed for the direct and the resolved part of the cross sections, only the sum is a physical observable. The following settings can be chosen by the user:

- the **heavy quark type**, i. e. charm or beauty,
- the **mass** m_Q of the heavy quark Q ,
- the **factorisation and renormalisation scales** as a multiple of the transverse mass $m_t = \sqrt{m_Q^2 + (p_{t,Q,1}^2 + p_{t,Q,2}^2)/2}$ for the double differential mode and $m_t = \sqrt{m_Q^2 + p_{t,Q}^2}$ for the single differential mode, respectively,
- the types of the **colliding beam particles**, e. g. ep or γp collisions,
- the **centre-of-mass energy** E_{cms} ,

| FMNR | μ_r | μ_f | m_c [GeV] | ϵ_{pet} | p -PDF | γ -PDF |
|---------------------|-----------------|---------------|-------------|------------------|----------|---------------|
| decreasing σ | $2 \cdot m_t$ | m_t | 1.7 | 0.042 | | |
| default | m_t | $2 \cdot m_t$ | 1.5 | 0.035 | CTEQ5M | GRV-G HO |
| increasing σ | $0.5 \cdot m_t$ | $4 \cdot m_t$ | 1.3 | 0.028 | | |

Table 2.3: Renormalisation (μ_r) and factorisation (μ_f) scales, the charm pole mass (m_c), the Peterson parameters (ϵ_{pet}) and the parton density parametrisations of the D^* cross section calculations with the FMNR program with their default settings and variations.

The transverse mass is defined as $m_t = \sqrt{m_c^2 + p_{t,c}^2}$ for single differential and $m_t = \sqrt{m_c^2 + (p_{t,c,1}^2 + p_{t,c,2}^2)/2}$ for double differential calculations.

- the **parton density parametrisations** of the colliding particles; for a correct subtraction of terms which in leading order contribute to resolved and at NLO to direct processes, the **factorisation scheme** used for the photon density, e. g. DIS or $\overline{\text{MS}}$, is needed in the direct calculation,
- the Λ_{QCD} parameter
- and the **number of iterations** of the numerical integration and the number of *events* generated to achieve the result.

For the resolved calculation in ep mode the photon density has to be folded with the photon flux from the positron (eq. 1.12) for the specific range of the inelasticity y [55]. If the information about y in the resolved calculation is needed ($d\sigma/dW_{\gamma p}$ and $d\sigma/dx_\gamma(D^*+\text{jet})$), the calculation is performed in γp mode at a photon-proton centre-of-mass energy $W_{\gamma p}$ corresponding to a fixed value of $y = W_{\gamma p}^2/s$. Then the result has to be multiplied with the integrated photon flux of a small range around the fixed y .

To take into account the fragmentation of charm quarks into D^* mesons, the final result is multiplied by the charm hadron production fraction of D^* mesons, $\mathcal{H}(c \rightarrow D^*) = 0.235$ [27]. The fragmentation of the quarks into the observable D^* mesons is performed by the Peterson fragmentation [29]. This means that the meson momentum is achieved by downscaling the quark momentum. The downscaling factor is obtained from a random distribution according to the Peterson function which depends on a single parameter ϵ_{pet} . The scaling is done in the centre-of-mass frame of the partonic system (single differential mode) and in the frame defined by $p_z(Q) = -p_z(\overline{Q})$ (double differential mode), respectively. The generation of a transverse momentum relative to the quark direction by parton radiation in the fragmentation process is neglected.

For the $D^*+\text{jet}$ analysis the inclusive k_t -jet algorithm is applied to the two or three outgoing partons. The D^* -jet is identified as the jet which contains the quark fragmenting into the D^* meson. This jet is not taken into account here since the jet is intended to tag a parton different from the D^* tagged charm quark. The effect of the transition from a jet on the parton level to jets built from observable hadrons and the necessary corrections will be studied in section 6.7.

The importance of higher order terms in the NLO calculations is estimated by varying the scales by factors 0.5 and 2. Table 2.3 shows the chosen scales and other relevant parameters for the calculation of D^* cross sections. The central choice of the renormalisa-

tion (μ_r) and factorisation (μ_f) scales and of the charm pole mass are the same as for the latest H1 publication [1] and as the choice of the FMNR authors. The default Peterson parameter ϵ_{pet} is taken from [56]. As parton densities the parametrisations CTEQ5M [41] and GRV-G HO [42] are used for the proton and the photon, respectively. The former is parametrised in the $\overline{\text{MS}}$, the latter in the DIS scheme. The Λ_{QCD} parameter is set to $\Lambda_{QCD}^{(5)} = 0.226$ GeV to match the CTEQ5M parametrisation.

In the following the effect of the negative weights occurring for interference terms and the sensitivity of the cross section calculation on the parameters will be investigated exemplarily for the $p_t(D^*+\text{jet})$ distribution.

Figure 2.3a) shows the cross section prediction of the direct and the resolved part in very small bins. The essential observation is the occurrence of the negative values for $p_t(D^*+\text{jet}) < 1$ GeV. They can be understood since negative weights of interferences of diagrams like those shown in figure 1.9a+c) belong to final states with only two outgoing partons, namely the charm and the anticharm quark. These partons must be balanced in p_t , leading to a vanishing transverse momentum of the parton-parton pair. Due to the fragmentation of one of the quarks into the D^* meson this p_t balance is deteriorated and the negative weights do not accumulate at exactly zero. This behaviour is typical for all quantities which are not “infrared safe” at next-to-leading order like $p_t(D^*+\text{jet})$ and $\Delta\phi(D^*,\text{jet})$. Nevertheless, by integrating the problematic region in larger bins a valid prediction can be made as shown in figure 2.3b). However, the effect of varying the perturbative scales is large.

Both figures 2.3a-b) show that the resolved part of the predictions is very small. In figure 2.3b) also the variation of the prediction when varying the renormalisation scale by factors of 0.5 and 2 is shown. This has a large influence on the result, indicating the importance of higher order terms. A lower renormalisation scale leads to a larger coupling constant $\alpha_s(\mu_r)$. This generally increases the cross section prediction. But in special regions in phase space the opposite behaviour can be seen: At low $p_t(D^*+\text{jet})$ the cross section decreases due to the higher probability of gluon radiation which deteriorates the p_t balance.

The figures 2.3c-f) illustrate the influence of varying the different parameters of the calculation listed in table 2.3. The relative deviation between the default values and varying each parameter individually up or down is shown. The renormalisation scale μ_r has the largest influence, up to 60%. Varying the factorisation scale μ_f leads to changes in the opposite direction of varying μ_r . A larger scale generally increases the cross section because larger scales lead to increasing parton densities. But also here there are exceptions, at low $p_t(D^*+\text{jet})$ both halving and doubling the scale leads to a slightly decreased prediction. Generally the effect is of the same order of magnitude as varying the charm mass $m_c \pm 0.2$ GeV, up to 15%. Varying the Peterson parameter ϵ_{pet} by 20% has only a negligible effect up to about 5%.

Varying these parameters qualitatively shows the same effects for all other D^* and $D^*+\text{jet}$ quantities considered in the analysis of this thesis: The renormalisation scale μ_r generally has the largest influence and varying the Peterson parameter is negligible. An exception are the inclusive D^* calculations where halving μ_f leads to a slightly lower cross section than doubling μ_r .

In the recent H1 publication measuring beauty cross sections using the semileptonic decay of B hadrons into muons [57] the uncertainties of the FMNR calculations are es-

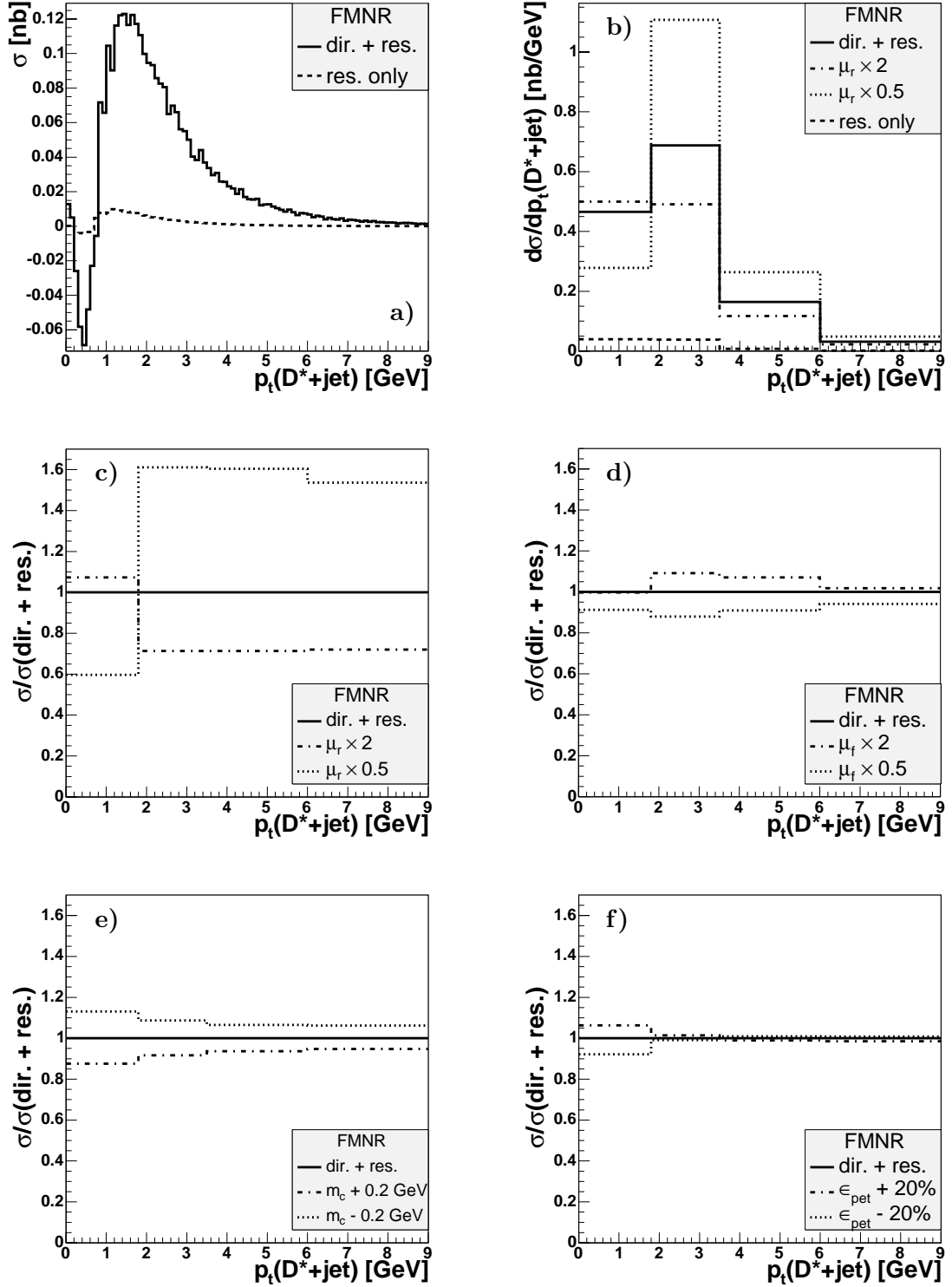


Figure 2.3: Results of the next-to-leading order QCD calculations of the FMNR program as a function of the combined $D^*+\text{jet}$ quantity $p_t(D^*+\text{jet})$ (a,b) and the relative effect of varying (cf. table 2.3) the renormalisation and the factorisation scales, the charm mass and the Peterson parameter (c-f).

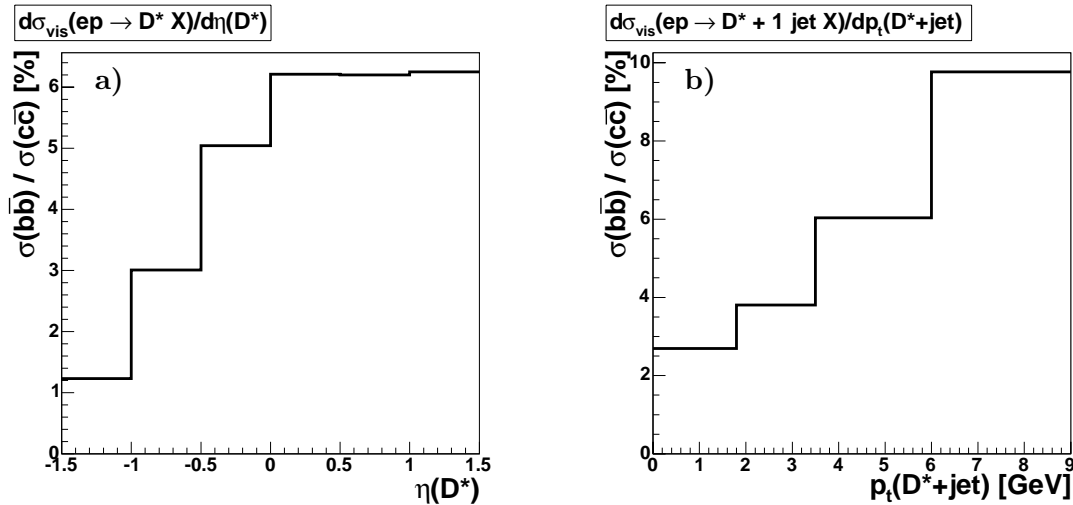


Figure 2.4: Ratio of the beauty contribution to D^* and D^* +jet cross sections in CASCADE 1.2, for the inclusive D^* cross section as a function of $\eta(D^*)$ (a) and for the D^* +jet cross section as a function of $p_t(D^*$ +jet) (b).

timated by varying both scales simultaneously up or down and varying the heavy quark mass at the same time. Also in the calculation of charm cross sections using $D^*\mu$ correlations [10] both scales are varied simultaneously, but the effect of varying the heavy quark mass only is added in quadrature. But when varying both scales simultaneously in the same direction the effects on the cross section partially cancel. On the other hand for single bins the effect of varying μ_r (which in general leads to the largest effect) can be small due to the cancellation of contrary effects as described for low $p_t(D^*$ +jet). Thus the uncertainty of the cross section prediction of the FMNR calculation will be estimated as follows: For each calculated bin the maximal deviation up- and downward obtained by individually varying the renormalisation scale, the factorisation scale and the charm mass as stated in table 2.3 define the upper and lower bound of the prediction.

2.4 Contribution from Beauty Production

D^* mesons are produced, in addition to the fragmentation of charm, in the decay of hadrons containing beauty quarks. In this way beauty production contributes to D^* and D^* +jet cross sections.

The beauty contribution is calculated in two different approaches: In the visible range of this analysis (table 5.6) CASCADE 1.2 predicts $\sigma(ep \rightarrow b\bar{b} \rightarrow D^*) = 0.20$ nb which is 3.6% of the charm prediction $\sigma(ep \rightarrow c\bar{c} \rightarrow D^*) = 5.52$ nb. This increases slightly to 5.4% considering D^* +jet cross sections. PYTHIA predicts a beauty contribution of below 3% even for D^* +jet.

As an example, figure 2.4 shows the ratio of the beauty contribution as a function of the pseudorapidity of the D^* (without jet requirement) and as a function of the transverse momentum of the D^* +jet pair. It rises in the forward direction up to 6% which is the largest value for all inclusive D^* distributions considered in this analysis. In the forward direction the charm cross section decreases, whereas in the backward direction beauty is

kinematically suppressed since its higher mass needs more energy from the photon side (larger inelasticities y) to be produced closer to the photon direction.

Larger transverse momenta of the D^* +jet pair are particularly preferred in beauty production. The decay of the beauty hadron into a D^* meson causes an additional momentum loss of the D^* relative to the initial beauty quark. This leads to a larger transverse momentum of the D^* +jet system. The reason is similar to what caused the negative dip in the FMNR calculation of this distribution (figure 2.3a)) to be not exactly at zero.

The beauty ratio in all other distributions is smaller than 10%, the largest seen at large $p_t(D^*$ +jet). An exception are medium $x_\gamma(D^*$ +jet) and large $p_t(\text{jet})$ where it reaches 15%. Compared to other uncertainties in the calculations and in the data the beauty contribution is not significant in any measured region of phase space. This is even true in case the prediction of the beauty cross section needs an extra normalisation factor of ~ 1.5 as recently measured [57]. Hence for simplicity the beauty contribution will be neglected when comparing theoretical predictions to the data.

Chapter 3

The H1 Experiment at HERA

The H1 detector is a general purpose detector, measuring energy and momentum of charged and neutral particles, production vertices, the luminosity of the colliding beams and providing information useful for particle identification. It is located at the **H**adron-**E**lectron-**R**ing-**A**nlage HERA of the DESY laboratory in Hamburg, Germany. HERA accelerates protons to energies of 920 GeV (820 GeV before 1998) and electrons (or positrons) to energies of 27.6 GeV, yielding a centre-of-mass energy of $\sqrt{s} \approx 319$ GeV. Electron and proton bunches collide every 96 ns in the two interaction regions where the experiments H1 and ZEUS are located, H1 in the northern and ZEUS in the southern hall.

A schematic side-view of the H1 detector is given in figure 3.1. The beam pipe (not shown) is surrounded by the tracking detectors which are followed by the calorimeters. The superconducting solenoid (not shown) comprises the calorimeters. It provides the magnetic field of ~ 1.15 T needed to measure momenta with the tracking detectors. In this way the amount of dead material in front of the calorimeters is reduced compared to a setup where the solenoid is placed in between the trackers and the calorimeters. The whole apparatus is surrounded by an iron yoke to return the magnetic flux of the solenoid.

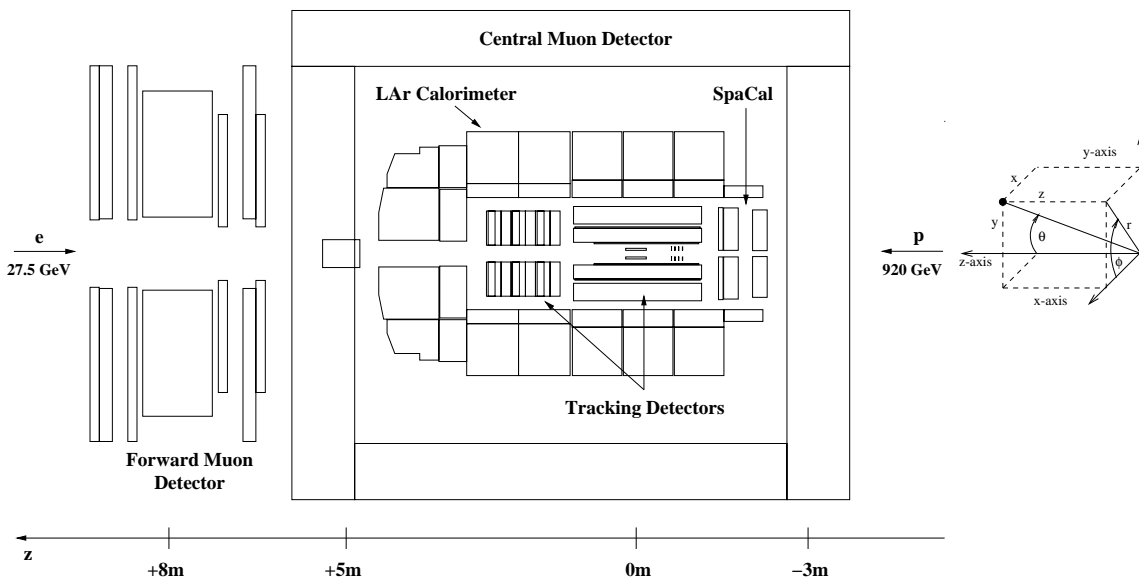


Figure 3.1: Schematic longitudinal section of the H1 detector and its coordinate system.

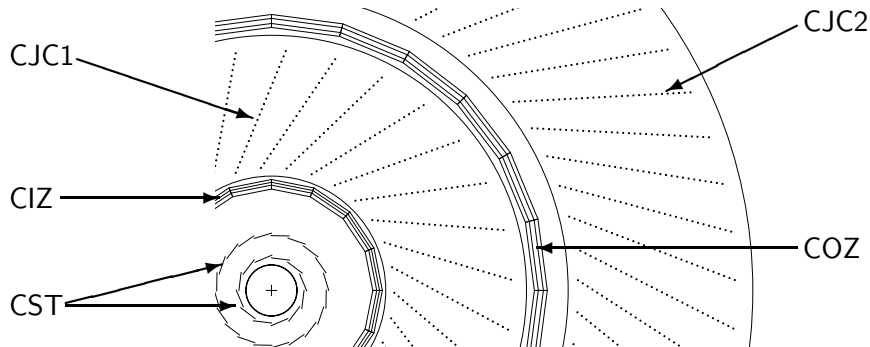


Figure 3.2: *Cut-out of the radial view of the central trackers. The CIP and the COP are not shown, they are located close to the CIZ and in between the COZ and the CJC2, respectively.*

The iron yoke is instrumented and used as central muon detector.

The z -axis of the right handed H1 coordinate system is defined by the beam axis with positive values in the direction of the colliding protons. The x -axis points towards the centre of the HERA ring and the y -axis points perpendicular upwards. The origin is the nominal interaction point. The azimuthal angle ϕ lies in the xy -plane and the polar angle θ is measured from the z -axis as depicted in figure 3.1.

Due to the different beam energies the H1 detector is instrumented asymmetrically. The forward direction, defined by positive z -values, has an enhanced instrumentation, e. g. the forward tracker, the forward muon system and finer granularity of the calorimeter. On the other side, in the backward direction, the spaghetti calorimeter SpaCal is especially designed to detect and to trigger the scattered electron in neutral current events up to $Q^2 = 100 \text{ GeV}^2$.

The H1 experiment is completed by several small detectors close to the beamline, in the forward direction to detect the scattered proton or its remnant and in the backward direction to tag electrons scattered under small angles and to measure the luminosity.

The H1 detector is described in many theses, e. g. [9, 58], and – as operational before 1995 – in [59, 60]. In the following the components relevant for this analysis will be briefly described before it will be introduced how information about particle identification can be obtained from the tracking detectors. Then some aspects of the detector simulation and of the reconstruction of the hadronic final state from tracks and energy depositions in the calorimeters will be discussed.

3.1 Central Tracking Detectors

The central tracking system consists of the central jet chamber (CJC), the central silicon tracker (CST) and the central inner and outer z -chambers (CIZ/COZ) which are shown in a radial view in figure 3.2. The central inner and outer proportional chambers (CIP/COP) are not shown. They are used for triggering only and are close to the CIZ and COZ, respectively.

The main tracking device is the CJC which consists of two gas-filled coaxial cylinders

along the beam axis from $z = -1.1$ m to $z = +1.1$ m. The inner chamber (CJC1) covers the angular range $11^\circ < \theta < 169^\circ$ and the outer chamber (CJC2) covers $26^\circ < \theta < 154^\circ$. Sense- and several kinds of field-wires are clamped parallel to the z -axis.

Charged particles traversing the CJC ionise the CJC gas. The released electrons drift towards the sense-wires and cause an electron cascade, driven by the electric field between the sense- and the field-wires. The drift velocity and the time at which the charge collected by the sense-wires is measured, define the position of the hits in the $r\phi$ -plane. A resolution of $\sigma_{r\phi} = 130 \mu\text{m}$ is achieved [61]. The charge is read out at both ends of the sense-wires. In this way the z -position of a hit can be determined using the principle of charge division. The resolution is not as good as in the $r\phi$ -plane and reaches $\sigma_z = 22$ mm.

The magnetic field of the solenoid is parallel to the z -axis and the trajectory of a charged particle follows a helix. Pattern recognition is applied to find tracks. Helices are fitted to the measured hits to determine the track parameters. Effects like multiple scattering and energy loss in the traversed matter or slight inhomogeneities of the magnetic field result in small deviations from the helix. They are taken into account in the determination of the track momentum at the event vertex. Constraining the tracks to such a common vertex improves the momentum resolution significantly.

To further improve the z -resolution, hits in the CIZ and the COZ are taken into account in the track reconstruction. They are located inside the CJC1 and in between the CJC1 and CJC2, respectively. Their signal-wires are perpendicular to the z -axis resulting in a z -resolution better by two orders of magnitude compared to the CJC alone.

The central silicon tracker (CST) [62] is the innermost track detector. It consists of two layers with a polar coverage of $30^\circ < \theta < 150^\circ$. In $r\phi$ a hit resolution of $\sigma_{r\phi} = 12 \mu\text{m}$ is achieved. This allows the reconstruction of secondary vertices e.g. from D^0 decays [63], a feature that is not exploited in this analysis. But including the precise CST $r\phi$ -hits in the track fit improves the transverse momentum resolution due to the good hit resolution and due to the extension of the measured arc length in the $r\phi$ -plane.

3.2 Calorimeters

The two most important calorimeters of the H1 experiment are the liquid argon calorimeter (LAr) and the spaghetti calorimeter (SpaCal).

The LAr calorimeter [64] encloses the forward and the central part of the detector with a polar coverage of $4^\circ < \theta < 154^\circ$. It is a sampling calorimeter with absorbers of lead in the inner electromagnetic and of stainless steel in the outer hadronic part. The electromagnetic and hadronic parts of the calorimeter can be seen in figure 3.3 in a longitudinal section of the upper half of the LAr. Altogether it has more than 44000 readout channels, called calorimeter cells.

The LAr is a non-compensating calorimeter, it has on average a larger response for electromagnetic compared to hadronic energy depositions. A software weighting algorithm is applied to correct for the electromagnetic shower fraction of energy depositions caused by hadrons, examining shower shapes. Since the shape of low energetic hadronic depositions is irregular, for energy depositions below $\sim 7 - 10$ GeV in a specific cone weighting factors are applied without detailed analysis of the shower shape.

The reconstruction software provides energy measurements with and without this correction of hadronic energies. The *hadronic* energy level applies the individual hadronic

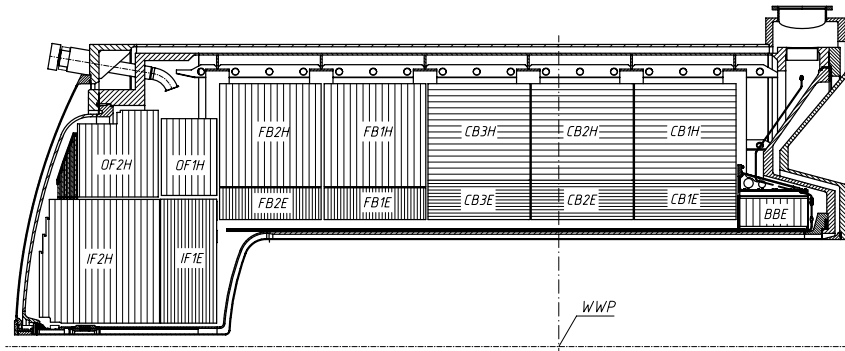


Figure 3.3: The upper half of the LAr calorimeter. The names of electromagnetic sections end with “E”, those of hadronic sections with “H”. The horizontal and vertical lines indicate the orientation of the absorber plates.

weighting factor for each calorimeter cell. The *electromagnetic* energy level assumes the energy deposition to be purely electromagnetic and only corrections for dead material in front of the calorimeter are applied. Finally the cells are grouped into clusters.

An energy resolution of $\sigma(E)/E \sim 12\%/\sqrt{E/\text{GeV}} \oplus 1\%$ in the electromagnetic part and of $\sigma(E)/E \sim 50\%/\sqrt{E/\text{GeV}} \oplus 2\%$ in the hadronic part is achieved.

The SpaCal [65] completes the calorimetric coverage in the backward direction with an angular acceptance of $153^\circ < \theta < 178^\circ$. It is a lead/scintillating fibre calorimeter with an electromagnetic and a hadronic layer. The SpaCal is designed to trigger, detect and identify the scattered electron in neutral current DIS events reaching $Q^2 = 100 \text{ GeV}^2$. An energy resolution of $\sigma(E)/E = 7.1\%/\sqrt{E/\text{GeV}} \oplus 1.0\%$ is reached in the electromagnetic section [66].

3.3 Luminosity System and Electron Taggers

The luminosity system of H1 consists of TlCl/TlBr crystal Čerenkov calorimeters located close to the beam pipe further away from the H1 detector in direction of flight of the electrons. The luminosity is measured by detection of Bethe-Heitler processes $ep \rightarrow ep\gamma$ for which the cross section is precisely known. Electrons are detected in the electron tagger at $z = -33.4 \text{ m}$ (ET33), photons in the photon detector at $z = -102.9 \text{ m}$ (PD). For an online determination of the luminosity the rate of coincident detection in both detectors is used. After offline calibration the luminosity is determined more precisely from the photon rate in the PD only [67]. A precision better than 1.5% is reached for the data set analysed in this thesis.

The ET33 is also used to trigger and to detect electrons in photoproduction events where the electrons are scattered under a very small angle. Electrons in events with $Q^2 < 0.01 \text{ GeV}^2$ and $0.2 \lesssim y \lesssim 0.7$ can reach the ET33. Further electron taggers are placed at $z = -43.2 \text{ m}$ and $z = -8.0 \text{ m}$ accepting lower and higher inelasticities y , respectively. Their acceptance is not understood as well as that of the ET33 and therefore they are not used in this analysis.

3.4 The Trigger System

Electron and proton bunches collide every 96 ns leading to a rate of 10.4 MHz. The rate of physically interesting ep reactions is much lower. The total photoproduction cross section $\sigma_{\gamma p}^{tot} \approx 165 \mu\text{b}$ [68] combined with a luminosity $L = 1.5 \cdot 10^{31} \text{ cm}^{-2}\text{s}^{-1}$, reached in 2000 data taking, leads to an event rate of the order of kHz. The rate of DIS events is much lower, in the order of a few Hz. In addition there is a rate of about 50 kHz from beam-gas collisions.

Since it is not possible to read out the total detector within 96 ns and to select the interesting events afterwards, fast hardware and software algorithms have to decide whether to keep an event or not. This is done by a multilevel trigger system which selects the relevant ep events and reduces the background rates in several steps. The input rate decreases from about 100 kHz at the first level (L1) down to 50 Hz at the fourth level (L4) which has a maximal output rate of 10 Hz.

The H1 trigger system consisted of the following trigger levels when the data analysed in this thesis have been recorded:

L1: The L1 decision is based on special trigger signals of various detector components. These 256 so-called trigger elements are logically combined to 192 subtriggers. An event is kept at L1 if at least one of the 192 subtriggers gives a positive decision. To allow sufficient time to acquire the individual signals, they are first fed into a pipeline, bunch crossing by bunch crossing. The decision to keep an event comes 24 bunch crossings later. The pipelines are stopped if the decision is positive. Until the pipelines are restarted, so-called dead time accumulates in which no data can be collected.

If a specific subtrigger has a too large rate, it can be scaled down by a factor n . This means that only every n -th positive decision of this subtrigger is taken into account, effectively reducing the integrated luminosity seen by the subtrigger.

The L1 output rate is of the order of a few kHz.

L2: Neural networks and topological triggers are implemented on L2. Within 20 μs the decision has to be made whether to start the full detector readout or to reject the event and to restart the pipelines. The L1 subtriggers selected in this analysis do not require an L2 condition to be fulfilled.

The L2 output rate has to be below 50 Hz since L3 was not yet operational for the data analysed here.

L4: On the fourth trigger level an online event reconstruction is performed. This does not contribute further to the dead time since an asynchronous event buffer is used.

If the L1 and L2 trigger decisions can be validated, the events are classified into L4 classes. They belong to at least one of the physics event classes if they provide a “hard scale”, e. g. a scattered electron with a sufficiently large Q^2 , or if specific final state finders select them. There are event classes selecting e. g. “high Q^2 ”, “diffraction” or “open charm” events. All events assigned to physics classes are kept. The remaining events are downscaled. For the kept fraction of the downscaled events an according weighting factor is stored, the L4-weight. The maximal allowed decision time of L4 is 100 ms.

L5: A complete offline event reconstruction is performed and its output is permanently stored on tapes.

3.5 Particle Identification using Energy Loss: dE/dx

Moderately relativistic charged particles other than electrons lose energy passing matter primarily by ionisation and atomic excitation. Their mean energy loss per path is given by the Bethe-Bloch equation [44]

$$-\left\langle \frac{dE}{dx} \right\rangle = 4\pi N_A r_e^2 m_e c^2 z^2 \frac{Z}{A} \frac{1}{\beta^2} \left[\frac{1}{2} \ln \frac{2m_e c^2 \beta^2 \gamma^2 T_{max}}{I^2} - \beta^2 - \frac{\delta}{2} \right]. \quad (3.1)$$

N_A denotes Avogadro's number, r_e the classical electron radius, m_e the electron mass, z the charge of the incident particle in units of the elementary charge, Z (A) the atomic number (mass) of the traversed matter and $T_{max} = \frac{2m_e c^2 \beta^2 \gamma^2}{1 + 2\gamma m_e/M + (m_e/M)^2}$ is the maximum kinetic energy that can be imparted to a free electron in a single collision of the particle with mass M and I is the mean excitation energy. The Lorentz variables $\beta = p/E$ and $\gamma = 1/\sqrt{1 - \beta^2}$ are defined as usual. The density effect correction $\delta/2$ is introduced to account for polarisation effects that effectively truncate the electric field extension of high energetic particles.

Measuring the energy loss dE/dx of particles allows to identify them because the dE/dx value in a given medium depends only on β but not independently on their mass and momentum. The energy loss according to the Bethe-Bloch equation always shows the same behaviour, namely a steep decrease at low $\beta\gamma$ before the minimum value is reached, followed by a slow increase at large $\beta\gamma$. The curve as a function of the momentum differs for particles with different masses, mainly at relatively low momenta.

The dE/dx of a track can be determined from the dE/dx values of the track hits. The process of energy loss is of stochastic nature. The probability density function of losing the energy ΔE while passing through a material of thickness x , $f(\Delta E, \beta\gamma, x)$, is usually called the Landau distribution. This distribution has a very long tail towards high values of ΔE due to possible single collisions with high energy transfer and the mean value is significantly higher than the most probable value. This effect is prominent especially for a small thickness x and thus complicates the determination of the dE/dx value of a track from the single hit values.

The dE/dx value in the CJC is measured by combining the measured charge collected by those hits of a track that fulfil certain quality criteria. A mean dE/dx value of the track is determined by transforming the distribution of energy depositions of single hits like $dE/dx \rightarrow 1/\sqrt{dE/dx}$ and finally re-transforming the mean of this more symmetric distribution. To take into account the path length of a track that contributes to the collected charge of each hit, the obtained value has to be multiplied with $\sin \theta$ where θ is the polar angle.

The obtained dE/dx values do not obey the Bethe-Bloch equation exactly for several reasons. The mean value may be distorted due to a threshold requirement in the hit acceptance. The values are improved by run dependent constants and instead of the Bethe-Bloch equation the dE/dx parametrisation [69]

$$f_{\frac{dE}{dx}} = p_1 \cdot \frac{z^2}{\beta^{p_2}} \left[1.0 + p_3 \cdot e^{-p_4 \cdot \log_{10}(0.25 + \beta\gamma)} \right] \quad (3.2)$$

is used. The dE/dx values are normalised such that $f_{dE/dx} = 1$ for minimum ionising particles (m.i.p.). If a track has less than 10 hits usable for the dE/dx measurement, the

dE/dx value cannot be determined reliably. Figure 3.4a-b) shows the measured values for tracks in events with a selected D^* meson in the signal region together with the parametrisation eq. 3.2 for pions, kaons and protons.

The likelihood of a track to be a specific particle can now be defined via the integral of the χ^2 density for one degree of freedom

$$LH = \frac{1}{\sqrt{2\pi}} \int_{\chi^2}^{\infty} e^{-t/2} \cdot \frac{1}{\sqrt{t}} dt, \quad (3.3)$$

$$\chi^2 = \frac{\left(dE/dx - f_{\frac{dE}{dx}}(p, m)\right)^2}{s_{dE/dx}^2 + s_p^2}, \quad (3.4)$$

$$s_{dE/dx} = \sigma_{dE/dx} \cdot f_{\frac{dE}{dx}}(p, m),$$

$$s_p = \left(f_{\frac{dE}{dx}}(p + \sigma_p, m) - f_{\frac{dE}{dx}}(p - \sigma_p, m)\right)/2.$$

The absolute uncertainty of the momentum measurement, σ_p , is obtained from the track fit and the relative resolution of the dE/dx measurement, $\sigma_{dE/dx}$, depends on the number of hits used and is parametrised as in [69]. Therefore $s_{dE/dx}$ and s_p represent the uncertainty contribution of the dE/dx and the momentum measurement, respectively. The latter usually is small.

A flat distribution of LH is expected for particles that have been assigned the correct mass hypothesis. Wrong particle hypotheses accumulate close to zero. This behaviour can be clearly seen in the figures 3.4c-d) which show the LH distribution for the tracks of the kaon and pion from the decay of the D^0 for D^* candidates in the signal region.

3.6 Detector Simulation

The efficiency of reconstructing and triggering D^* mesons and D^* +jet pairs will be determined with a simulation of the H1 detector using Monte Carlo event generators.

Events are generated e. g. by PYTHIA resulting in four-vectors and particle types of the produced particles. For these particles decay and passage through the detector and the corresponding detector response is simulated by the standard H1 detector simulation which is based on GEANT 3 [70]. The trigger response is also simulated. The resulting detector signals are passed through the same reconstruction program that is also used for the data.

In this way the reconstructed events can directly be compared to the “real” (generated) events. Efficiencies can be determined as the ratio between the number of reconstructed and generated events in the considered kinematical region. To apply this simple unfolding method it has to be ensured that the data are well described by the reconstructed quantities of the simulation.

The simulation has to take into account that the status of the detector may differ slightly from run period to run period. This is achieved by simulating for each such period a fraction of the generated events that is proportional to the integrated luminosity for which the detector condition is valid. In this way e. g. temporarily broken sectors of the CJC affecting the track reconstruction in a specific region are properly taken into account.

An exception is the electron tagger ET33. Frequent small variations of the beam conditions have a strong influence on the acceptance of the ET33. For this reason it is

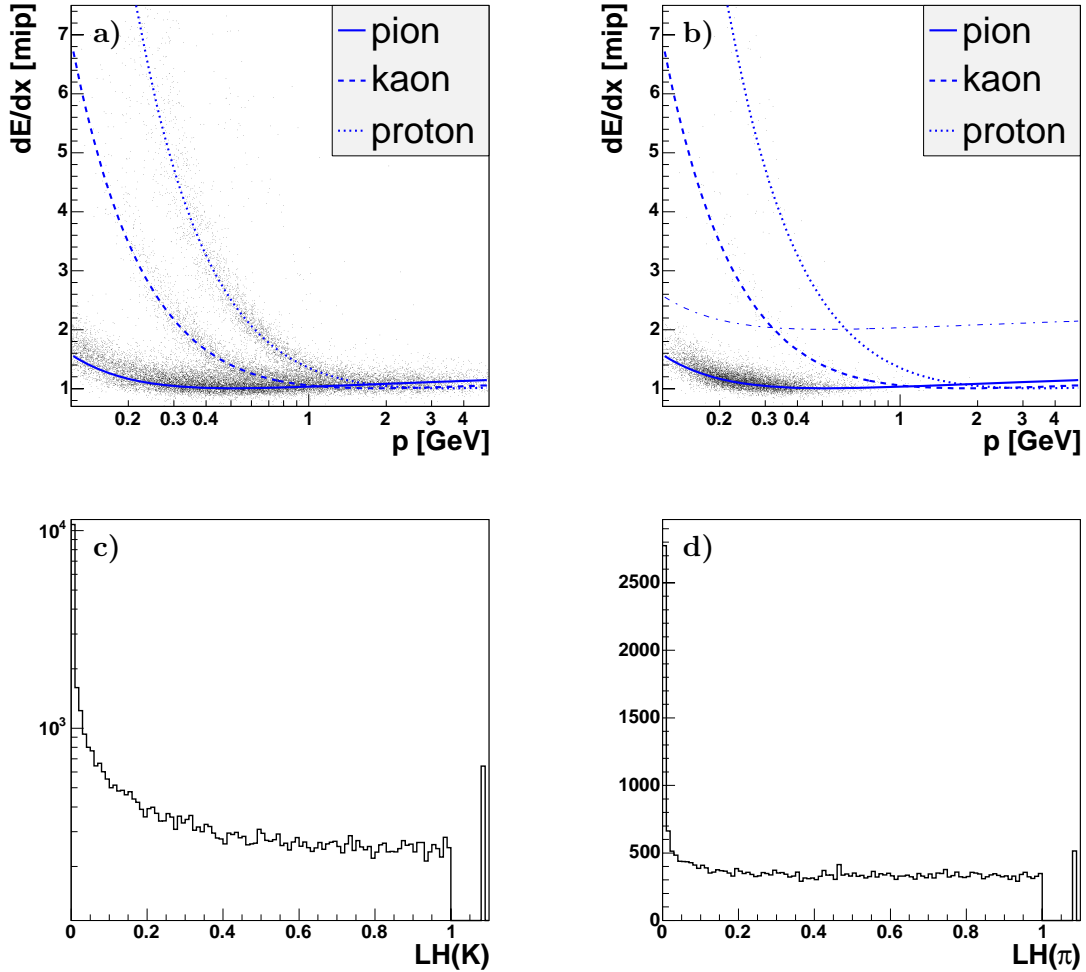


Figure 3.4: Measured dE/dx values for central tracks in events with a reconstructed D^* candidate in the signal region $143 < \Delta m < 148$ MeV (a) and for tracks taken as the slow pion π_s (b). The dash-dotted line indicates the cut which will be applied to remove those particles that obviously are not pions.

For the kaon tracks of the D^0 candidates the distribution of the resulting likelihood values to be a kaon, $LH(K)$, is shown in a logarithmic scale (c) and in an analogous manner $LH(\pi)$ of the pion tracks of the D^0 candidates in a linear scale (d). Values above one indicate tracks without a dE/dx measurement. For the D^* selection see section 4.2.

not fully simulated in the H1 simulation software and no reliably reconstructed energy deposition in the ET33 is available. The H1 collaboration has determined the acceptance of the ET33 as a function of the inelasticity y and averaged over certain run ranges as will be shown in figure 5.2. This finite acceptance of the electron tagger is taken into account by applying weights to the simulated events according to the acceptance function.

3.7 Combining Tracks and Clusters

Measuring particles as tracks in the tracking chambers or as energy depositions in the calorimeters has different advantages. In general tracks can be measured precisely in the regime of relatively low transverse momenta p_t up to a few GeV. The precision decreases with increasing p_t . Only charged particles can be detected, thus on average about one third of the produced particles are not detected. In contrast both charged and neutral particles (except neutrinos) can be detected in the calorimeters and the uncertainty of their energy measurement decreases with increasing energy.

To exploit the full energy and momentum range the measurements of both kinds of detectors are combined. An important requirement of an algorithm providing this combination is to avoid double counting of energy. This problem arises from particles which both are detected in the tracking detectors and deposit energy in the calorimeters.

In this analysis the HADROO2 [71] algorithm is used to define so-called Hadronic Final State (HFS) objects. These HFS objects are built as combinations of tracks and energy clusters which are identified to belong to the same particle. An HFS object can be built either from a combination of a track with clusters, from a track only or from clusters only.

For each combined HFS object the algorithm decides whether the transverse momentum measurement of the track or the cluster energy defines the four-vector. For track measurements the pion mass is assumed¹. For measurements from clusters the treatment of the mass of the resulting HFS object depends on whether the cluster is found to be hadronic or electromagnetic. If it is hadronic, the cluster four-vector is calculated as the four-vector sum of its cells which are assigned no mass. This results in massive cluster four-vectors. For electromagnetic clusters the momentum is scaled to the measured energy leading to massless clusters.

The main steps of the algorithm are the following:

- selection of tracks without double counting of different track hypotheses,
- removal of clusters which are identified as noise,
- temporary removal of tracks and clusters which are already identified as leptons,
- loop over the tracks starting with the lowest p_t ,
- extrapolation of each track into the calorimeters,
- matching of clusters to the extrapolated track,
- comparison of the track and cluster measurements including a check whether they agree with each other within their uncertainties,
- build an HFS object according to the comparison and the cluster properties,
- if clusters are left after extrapolation of all tracks, build HFS objects for them,

¹The mass for tracks matched with clusters has erroneously been set to zero in the H1 analysis software.

| <i>Track selection</i> |
|--|
| reconstructed with CJC, CST, CIZ, COZ fitted to a vertex prefer primary vertex hypothesis |
| $p_t > 120 \text{ MeV}$ $20^\circ \leq \theta \leq 160^\circ$ $d'_{ca} \leq 2 \text{ cm}$ $r_{start} \leq 50 \text{ cm}$ $r_{end} - r_{start} > 10 \text{ cm} (\theta < 150^\circ)$ $r_{end} - r_{start} > 5 \text{ cm} (\theta > 150^\circ)$ |

Table 3.1: *Selection criteria for tracks considered by the HFS algorithm HADROO2. The distance of closest approach d'_{ca} is calculated in the $r\phi$ -plane as the distance of the non vertex fitted hypothesis of a track to the vertex which the track is fitted to, r_{start} and r_{end} and are the radii of the first and the last CJC hit of a track.*

- add all identified leptons to the list of HFS objects².

The track selection is based on vertex fitted tracks reconstructed in the central tracking detectors.³ The selection is based on [72], the details are listed in table 3.1. If a track has several hypotheses fitted to the primary vertex and to secondary vertices, the primary vertex hypothesis is chosen.

Only the LAr and the SpaCal calorimeters are used. The reconstructed clusters still contain noise. The main noise suppression algorithm on top of the global reconstruction code is to remove clusters which consist of one cell only or which have an energy deposition measured on the electromagnetic scale of $E_{clu} < 0.2 \text{ GeV}$ in the LAr and $E_{clu} < 0.1 \text{ GeV}$ in the SpaCal, respectively. More advanced algorithms suppress isolated clusters below a θ dependent energy threshold and clusters which show beam halo or cosmic patterns.

The track parameters at the vertex are extrapolated assuming a constant magnetic field along the z -axis and neglecting multiple interaction and energy loss in the traversed matter. The extrapolation stops at the surface of the calorimeters. If a track can be extrapolated more than half the circumference of the projection of its helix in the $r\phi$ -plane without reaching the calorimeter surface, it defines an HFS object by itself. This happens for a track with such a low transverse momentum that it cannot reach the calorimeter radius. The mathematical helix extrapolation would lead to a track impact in the SpaCal or the IF wheel of the LAr, depending on the sign of p_z .

All tracks that reach the calorimeter are first classified as *good* or *bad*. *Good* tracks are those where the error on the track energy, propagated from the track fit assuming the pion mass, is smaller than the error of the expected energy deposition of the track in the calorimeter. Then the measurement of the track is assumed to be more reliable than that of the calorimeter. The energy of a track is $E_{tr} = \sqrt{p_{tr}^2 + m_\pi^2}$ and the uncertainty $\sigma_{E_{tr}}$ is propagated from the track parameters. Since the uncertainty of the energy measured in

²Since in this analysis photoproduction events are identified by detection of the scattered electron in an electron tagger, even an electron erroneously identified as scattered electron inside the main detector is added to the HFS.

³The original HADROO2 also uses tracks from the forward tracker and combined fits from both.

the (LAr-) calorimeter has been determined to behave like $\sigma_E/E \approx 0.5/\sqrt{E/\text{GeV}}$ [60], a track is *good*, if it fulfils

$$\frac{\sigma_{E_{tr}}}{E_{tr}} < \left(\frac{\sigma_E}{E}\right)_{LAr}^{expect.} = \frac{0.5}{\sqrt{E_{tr}/\text{GeV}}}, \quad (3.5)$$

and *bad* otherwise. Tracks up to $p \approx 20$ GeV mostly are *good*.

Clusters are matched to an extrapolated track if they lie in a cylinder around the track direction at the calorimeter surface. The cylinder radius is 25 cm for clusters in the electromagnetic and 50 cm for clusters in the hadronic part of the calorimeter.

If the track is *good* or if the track energy is below the measured cluster energy or compatible with it, an HFS object is created based on the track measurement. The track energy is called compatible with or below the cluster measurement, if

$$E_{tr} < E_{cl} + 1.96 \cdot \sigma_{E_{cl}} = E_{cl} + 1.96 \cdot \left(0.5 \sqrt{E_{cl}/\text{GeV}} \text{ GeV}\right). \quad (3.6)$$

This means that the probability of E_{cl} being fluctuated upwards from E_{tr} is below 2.5%, assuming a Gaussian distribution based on the cluster measurement.

Now if in addition the probability that E_{cl} is an upward fluctuation of the “real” energy E_{tr} , based on the track measurement, is below 2.5%,

$$E_{cl} < E_{tr} \left[1 + 1.96 \cdot \sqrt{\left(\frac{\sigma_{E_{tr}}}{E_{tr}}\right)^2 + \left(\frac{0.5}{\sqrt{E_{tr}/\text{GeV}}}\right)^2} \right], \quad (3.7)$$

all clusters in the considered cylinder are not used further in the algorithm. Otherwise the energy difference $E_{cl} - E_{tr}$ probably belongs to an additional neutral particle or is caused by another track extrapolated into the same calorimeter region. To avoid double counting the track energy must be subtracted from the matched clusters and only the remaining energy $E_{cl} - E_{tr}$ is made available for further use in the algorithm.

If a track is *bad*, the cluster energy in the cylinder behind the extrapolated track defines the HFS object using the hadronic energy scale.

Neutral HFS objects are created for the remaining clusters which no track could be matched with. If more than 95% of the energy of a cluster is deposited in the electromagnetic part and more than 50% in the first two layers of the calorimeter, the cluster may be a photon and an HFS object is created using the electromagnetic energy scale. Otherwise the hadronic scale is applied.

The Hadronic Final State algorithm as described above is well suited to be applied to an analysis that covers the central detector region and is kinematically dominated by relatively low energies as is the case in charm production. This is illustrated in figure 3.5 which shows the correlation between the total generated and reconstructed energies in the central detector region $30^\circ < \theta < 150^\circ$. The energy of generated particles is counted only if either they have an energy above the noise threshold or they are charged particles in the central region above the minimal transverse momentum required for the track selection. Neutrinos are excluded as well. The generated energy can be reconstructed quite well, the ratio E_{rec}/E_{gen} is close to one.

A drawback of the HADROO2 algorithm presented above is the fact that the matching of clusters and tracks depends on the sequence in which the tracks are treated. If

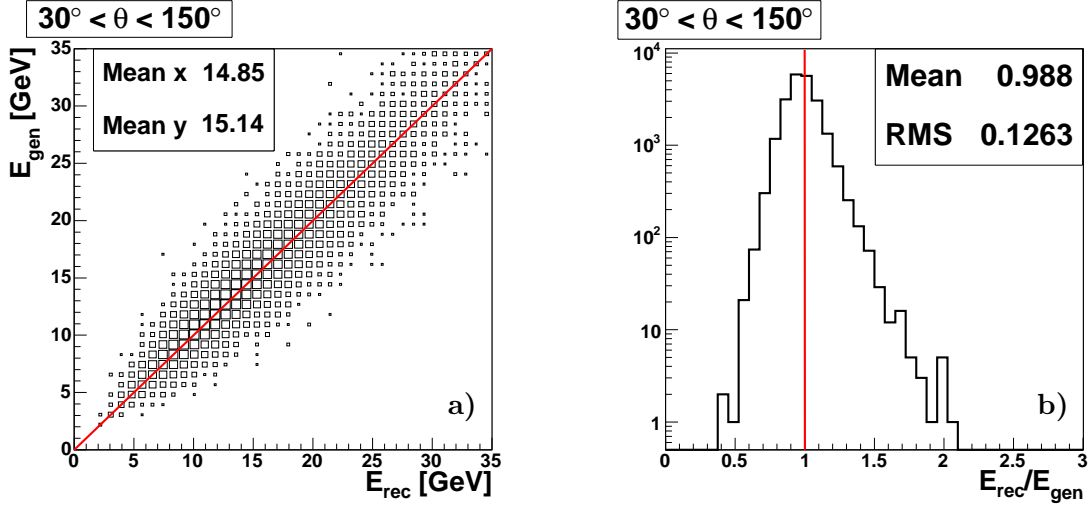


Figure 3.5: Correlation between the total generated and reconstructed energy the central detector region for HADROO2 in in charm events generated with CASCADE. Note that the box sizes increase logarithmically.

the extrapolation cylinders of two tracks overlap, a cluster may be associated to the track treated first, although it was caused by the second track. For the total energy flow this is problematic if the cluster falsely associated with the first track is interpreted as an upward fluctuation leaving no cluster to be matched with the second track. But only if this coincides with the second track being *bad*, the energy is lost for the total energy flow. For particle identification the association of clusters to a wrong track is more problematic, especially if the cluster shape is used for the identification. Therefore in [73] an HFS algorithm has been developed which is independent of the order of the track cluster matching. It is used for the identification of electrons within jets to select heavy quark events. For these events also the reconstruction of the inelasticity y , based on the hadronic final state, is slightly better compared to HADROO2.

Chapter 4

Reconstruction of D^* Mesons

This chapter describes how D^* mesons are selected in the data collected with the H1 detector. First a short overview over the decay of the D^* meson is given, followed by the chosen D^* reconstruction method. Finally the determination of the number of reconstructed D^* mesons in the data and in the Monte Carlo simulations is discussed in detail.

4.1 Decay of D^* Mesons

The probability that a charm quark hadronises into a D^{*+} meson is experimentally determined to be [27]

$$f(c \rightarrow D^{*+}) = (0.235 \pm 0.007 \pm 0.007). \quad (4.1)$$

The D^{*+} (D^{*-}) meson is an excited $c\bar{d}$ ($\bar{c}d$) state with a mass of $m(D^*) = 2010.0 \pm 0.5$ MeV [44].¹ It decays via the strong interaction leading to a very short lifetime. The decay channels and branching ratios are listed in table 4.1. The D^* mainly decays into a D^0 meson and a charged pion. The mass difference between the D^* and the D^0 , $m(D^*) - m(D^0) = 145.421 \pm 0.010$ MeV [44], is only slightly above the pion mass

¹In the following charge conjugated states are always implicitly included.

| D^{*+} | | D^0 | |
|-------------|--------------------|----------------------------|--------------------|
| Channel | \mathcal{BR} [%] | Channel | \mathcal{BR} [%] |
| $D^0\pi^+$ | 67.7 ± 0.5 | $K^-\pi^+\pi^0$ | 13.0 ± 0.8 |
| $D^+\pi^0$ | 30.7 ± 0.5 | $\bar{K}^0\pi^+\pi^-\pi^0$ | 10.9 ± 1.3 |
| $D^+\gamma$ | 1.6 ± 0.4 | $K^-\pi^+\pi^+\pi^-$ | 7.46 ± 0.31 |
| | | $\bar{K}^0\pi^+\pi^-$ | 5.4 ± 0.4 |
| | | $K^-\pi^+\pi^+\pi^-\pi^0$ | 4.0 ± 0.4 |
| | | $K^-\pi^+$ | 3.80 ± 0.09 |
| | | $K^-e^+\nu_e$ | 3.58 ± 0.18 |
| | | $K^-\mu^+\nu_\mu$ | 3.19 ± 0.17 |

Table 4.1: Decay channels and branching ratios \mathcal{BR} of the D^{*+} and of the D^0 meson [44]. For the D^0 only a selection is given.

$m(\pi^\pm) = 139.57018 \pm 0.00035$ MeV [44]. Therefore the pion has a very small momentum in the restframe of the decaying D^* , a fact which is transferred into the laboratory frame [74]. For this reason the pion of this D^* decay channel is usually referred to as “slow” pion and denoted as π_s^\pm .

The D^0 meson decays via the weak interaction. Several important decay channels are listed in table 4.1. They involve a charged or neutral kaon carrying the strange quark which the charm has decayed into via radiation of a W^\pm boson. In this thesis only the decay into a negatively charged kaon and a positively charged pion is considered. For other decays into more charged particles an increased combinatorial background is expected. Furthermore the systematic uncertainty due to an imperfect knowledge of the track reconstruction efficiency increases. Reconstructing neutral D^0 decay products in events with a relatively large particle multiplicity typical for D^* events is difficult ($\pi^0 \rightarrow \gamma\gamma$) or results in an even smaller overall branching ratio ($K^0 \rightarrow K_S^0 \rightarrow \pi^+\pi^-$). Thus the decay channel $D^0 \rightarrow K^-\pi^+$ is a good compromise despite its low branching ratio $\mathcal{BR} = 3.80 \pm 0.09\%$.

Altogether the branching ratio obtained for D^* mesons decaying via the chosen decay channel amounts to

$$\mathcal{BR}(D^{*+} \rightarrow K^-\pi^+\pi_s^+) = \mathcal{BR}(D^{*+} \rightarrow D^0\pi_s^+) \cdot \mathcal{BR}(D^0 \rightarrow K^-\pi^+) = (2.57 \pm 0.06)\%. \quad (4.2)$$

Reconstructing charm via the D^* meson rather than via other charmed mesons like the D^0 exhibits a special advantage due to the small mass difference $m(D^*) - m(D^0)$. This will become clear in the next section.

4.2 D^* Meson Selection

The D^* mesons are reconstructed via the decay chain $D^{*+} \rightarrow D^0\pi_s^+ \rightarrow K^-\pi^+\pi_s^+$ and the charge conjugate process. The decay particles K , π and π_s are reconstructed as tracks in the central tracking devices CJC, CIZ/COZ and CST. Only tracks fitted to the primary vertex are taken into account. In each event, tracks with opposite charges are combined in pairs, one assigned the pion, one the kaon mass. The invariant mass, $m(K\pi)$, is calculated. If the result is consistent with the D^0 mass $m_{D^0} = 1.8646 \pm 0.0005$ GeV [44] within the detector resolution, the remaining tracks with an opposite charge to that taken as a kaon are added assuming the pion mass to form a D^* candidate. The D^* candidate is accepted if it lies in the central region $|\eta(D^*)| < 1.5$, has a minimal transverse momentum of $p_t(D^*) \geq 2.0$ GeV and if the mass difference $\Delta m = m(K\pi\pi_s) - m(K\pi)$ is not too far above the nominal mass difference $\Delta m = 145.421 \pm 0.010$ MeV [44].

The track selection is based on the selection used for the construction of the hadronic final state objects (cf. table 3.1). Table 4.2 lists the additional cuts applied for the D^* decay tracks and the cuts for the D^* candidates. The cuts on the transverse momentum of the D^* meson and its decay tracks reduce the combinatorial background [74]. The signal of D^* mesons is visible in the Δm distribution shown in figure 4.1 whereas the signal would be less clear in the invariant mass distribution $m(K\pi\pi_s)$, as first exploited in [75]. The mass difference between the D^* and the D^0 meson is only a few MeV above the pion mass restricting the phase space for combinatorial background. The signal in Δm sits on top of a relatively small (but unfortunately steeply rising) background. Effects of the finite track resolution of the kaon and the pion from the D^0 decay partly cancel in the mass difference resulting in a small width of the signal.

| <i>Additional track selection</i> | |
|---|---|
| | primary vertex tracks |
| K, π | $r_{end} - r_{start} > 17$ cm $p_t > 300$ MeV |
| π_s | $r_{end} - r_{start} > 11$ cm |
| <i>D^* candidate selection</i> | |
| D^0 | $ m(K\pi) - m(D^0) < 80$ MeV |
| D^* | $\Delta m = m(K\pi\pi_s) - m(K\pi) < 167.5$ MeV $p_t(D^*) \geq 2.0$ GeV $ \eta(D^*) < 1.5$ |

Table 4.2: Selection criteria in addition to table 3.1 for the tracks considered as decay products of the D^* meson and for the D^* candidate itself. The radii r_{start} and r_{end} are those of the first and the last CJC hit of a track.

4.3 Determination of the Number of D^* Mesons

The number of D^* mesons is determined by fitting the function

$$f(\Delta m) = \frac{N(D^*)}{\sqrt{2\pi}\sigma} \exp\left(-\frac{(\Delta m - \mu)^2}{2\sigma^2}\right) + \frac{u_n}{N_{norm}} \cdot (\Delta m - m_\pi)^{u_e} \cdot (1 - u_s \cdot (\Delta m)^2) \quad (4.3)$$

to the measured Δm distribution. The function is a sum of a Gaussian for the signal and a background term. $N(D^*)$ represents the number of D^* mesons, σ and μ are the width and the mean of the signal.² The background term starts at the phase space border m_π and rises with an exponent u_e which is a free parameter of the fit. A quadratic correction term with the parameter u_s improves the description of the data in the high- Δm region [61]. This is important since otherwise the background parameters would be strongly influenced by the high- Δm region, leading to a bias in the region below the signal. The normalisation $1/N_{norm}$ depends on the background parameters such that the parameter u_n represents the number of D^* candidates in the background up to the fit limit.³ The fit is performed as a Likelihood-fit in the range $m_\pi < \Delta m < 167.5$ MeV, the result can be seen in figure 4.1.

In the following the signal-to-background ratio of this D^* fit is calculated as the ratio of the integrals of the resulting Gaussian and the background term within 2σ around the mean value of the Gaussian.

The Δm distributions of small subsets of the data often have low statistics. In this case a fit of all six parameters may give unreasonable results for the signal width σ which strongly influences the resulting number of D^* mesons $N(D^*)$. Therefore fits in subsets of the data are performed with fixed parameters μ , σ and u_s . If the number of entries in a Δm distribution is less than 200, also u_e is fixed. The fixed values are taken from a fit to a reference distribution. If not quoted differently, the inclusive D^* photoproduction sample is used as this reference.

Other methods to determine $N(D^*)$ will be discussed later.

²Since the function is fitted to a binned distribution, the Gaussian term needs as additional factor the bin width to make the fit parameter $N(D^*)$ represent the real number of D^* mesons.

³Also the background term needs the bin width as additional factor. The upper fit limit m_u leads to $N_{norm} = (1 - u_s m_\pi^2) \frac{(m_u - m_\pi)^{u_e + 1}}{u_e + 1} - u_s \left(\frac{(m_u - m_\pi)^{u_e + 3}}{u_e + 3} + \frac{2m_\pi (m_u - m_\pi)^{u_e + 2}}{u_e + 2} \right)$.

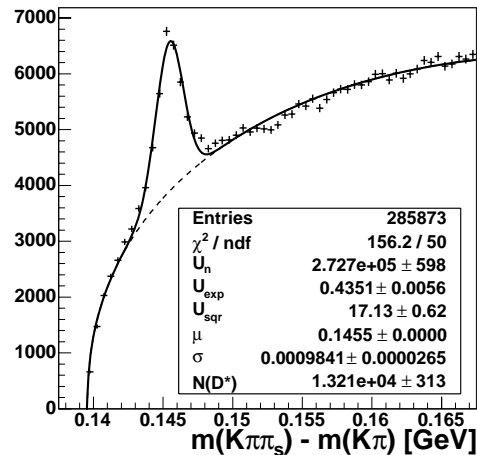


Figure 4.1: *Distribution of the difference Δm between the invariant mass of the D^* candidate and the D^0 candidate. No photoproduction or trigger selection is applied. The number of D^* mesons $N(D^*)$ is determined by the fit as described in the text.*

4.3.1 Monte Carlo Treatment

Events from the Monte Carlo generators are usually fed into the simulation only if at least one generated D^* meson in the decay channel $D^{*\pm} \rightarrow K^\mp \pi^\pm \pi_s^\pm$ has been generated. Therefore the reconstructed Δm distribution contains only a very small background from random combinations. For this distribution the fit as described above is not adequate. A first ansatz to determine the number of reconstructed D^* mesons would be to determine the signal width in the simulation and integrate over all bins within three standard deviations σ . Unfortunately the combinatorial background is too large to be neglected in this way. Therefore also in the simulation a fit is performed, but modified such that the background parameter $u_s = 33.0$ is fixed. The result of such a fit in almost background free Monte Carlo distributions is verified with an inclusive Monte Carlo sample of deep inelastic scattering, $Q^2 > 1 \text{ GeV}^2$, containing the combinatorial background. Figure 4.2a) shows the Δm distribution from the total sample, figure 4.2b) only those D^* candidates contribute that have a generated D^* meson with the same minimal cuts as applied in the usual simulated Monte Carlo data sets. The left distribution is fitted like the real data and the right with $u_s = 33.0$ fixed. The fit of the backgroundless distribution does not describe the distribution very well, resulting in a very large χ^2 value compared to the number of degrees of freedom.

The assumption of a simple Gaussian signal in the Δm fit is a simplification. Tails on both sides of the signal can be seen. This indicates that the signal is a composition of track combinations from tracks with different resolutions. The same effect is also visible in the inclusive Monte Carlo distribution and in real data, but less prominent due to statistical fluctuations of the background. Therefore it is neglected because the fitted number of D^* mesons of the background free Monte Carlo distribution satisfactorily reproduces the number obtained from the fit with background. This is also valid when comparing fit results in differential distributions.

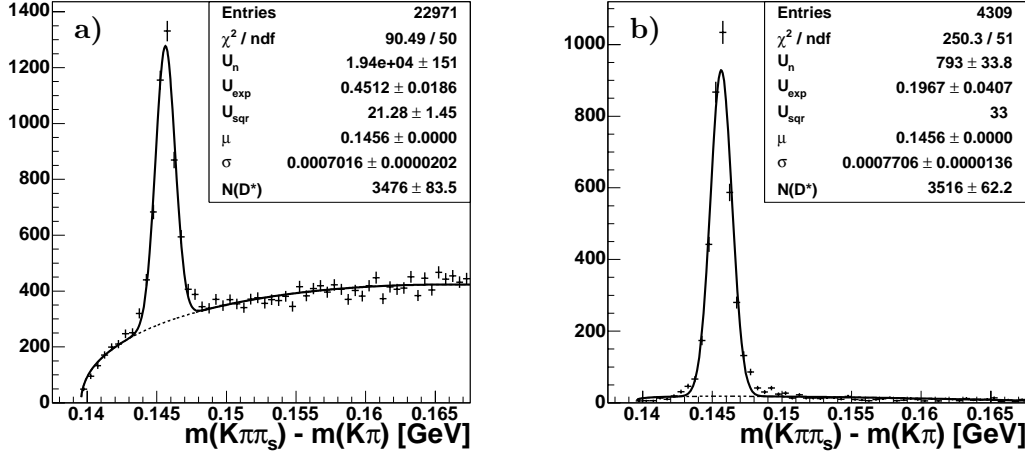


Figure 4.2: *Inclusive Monte Carlo sample: Δm distributions without (a) and with (b) requiring a generated D^* meson. The numbers of reconstructed D^* mesons resulting from the fits differ by 1%, but are compatible within their uncertainty.*

The signal width in the Monte Carlo simulation is slightly smaller than in the data (figure 4.1 and figure 5.4 for the final D^* photoproduction sample). This indicates that the track resolution in the simulation is overestimated. Fortunately this has no influence on the fit result as the width is a free parameter.

As described in section 5.4 Monte Carlo distributions are corrected for the acceptance of the electron tagger by applying event weights. For that reason a Likelihood fit is not applicable because the entries of the histogram bins do not follow the Poisson statistics. A χ^2 fit is used instead where the error of each bin is the square root of the sum of squares of the filled weights. In order to take account of the information from empty bins in distributions with low statistic, the error of these bins is set to the mean of the error of the next non-empty bins. The decision whether to fit with more fixed parameters is based on the effective number of entries in the histogram, $N_{\text{eff}} = (\sum w_i)^2 / \sum (w_i^2)$, where w_i are the filled weights.

4.3.2 Alternative Methods

To get a better handle on the shape of the background distribution, especially below the D^* signal, one could make use of so called “wrong charge” D^* candidates. Instead of combining a positively and a negatively charged track to form the D^0 meson, two like sign tracks are taken and combined with a third, now oppositely charged track as slow pion: $K^\pm \pi^\pm \pi_s^\mp$ instead of $K^\mp \pi^\pm \pi_s^\pm$. This “wrong charge” combinations in principle yield a similar distribution like the background in the real Δm distribution because the combinatorics is almost the same: If N^+ and N^- are the number of positively and negatively charged tracks, there are $N^+ \cdot (N^+ - 1) + N^- \cdot (N^- - 1)$ possibilities to combine two random tracks with the same charge to build a “wrong charge” D^0 candidate compared to

$N^+ \cdot N^+ + N^- \cdot N^-$ in the correct charge combination.⁴ The amount of real D^0 mesons combined with a random track as slow pion is negligible. Unfortunately these wrong charged combinations are not considered at the L4 trigger level. Thus events of the background type are only accepted if they have been triggered by another D^* -independent trigger. Therefore the number of events is significantly smaller even if the L4 trigger requirement is omitted. Nevertheless one can make use of this “wrong charged” Δm distribution in two ways. The first is to fit both the wrong charged and the real Δm distribution simultaneously with an additional parameter for the relative normalisation. The additional data points from the wrong charge combinations reduce the uncertainty of the fitted parameters. The second way is to scale the wrong charge combinations such that the integral of both distributions match in a Δm region far from the signal, say $153 < \Delta m < 167.5$ MeV. Then one can subtract the wrong from the correct charged distribution in the signal range $143 < \Delta m < 148$ MeV and the resulting number of D^* mesons is independent of the exact shape of the signal. Since it is not possible to select correct and wrong charged distributions triggered in a similar way, both these ansätze are not chosen here.

Besides the simple wrong charge subtraction method mentioned above there is a further way of determining the number of D^* mesons that is less dependent on the exact signal shape than a fit assuming a Gaussian form as in eq. 4.3. Instead of taking the number directly from the fit it can be calculated as the difference of the number of D^* candidates and the integral of the background term of the fitted function within e. g. three standard deviations around the fitted mean value. This method will be used to estimate the systematic uncertainty of the signal extraction.

⁴The slow pion has another momentum spectrum and so plays a minor role in this combinatorial consideration.

Chapter 5

Inclusive D^* Meson Measurements

This chapter presents the inclusive D^* meson analysis. The selection of data taking periods and the calculation of the integrated luminosity is presented, followed by the basic selection of photoproduction events. It is described how the achieved D^* signal can be improved, for example by particle identification. To derive cross section measurements from the obtained number of D^* mesons, correction factors have to be applied. The procedure to obtain these factors is explained in detail.

Finally the resulting cross section in the visible range and differential cross sections as a function of the transverse momentum $p_t(D^*)$, the pseudorapidity $\eta(D^*)$ and the photon-proton centre-of-mass energy $W_{\gamma p}$ are compared with several QCD calculations.

5.1 Run Selection and Luminosity Determination

This analysis uses data recorded with the H1 detector in the years 1999 and 2000 when HERA collided positrons of 27.6 GeV with protons of 920 GeV. Data taking periods with non standard operation like a shifted interaction point or a minimum bias trigger setup are excluded as well as runs declared “poor”. A run is considered as “poor” if either the liquid argon calorimeter (LAr), the spaghetti calorimeter (SpaCal), the luminosity system or both the central jet chambers (CJC1 and CJC2) and the central silicon tracker (CST) are out of operation. A few further runs in the beginning of the 1999 data taking are excluded because of missing output of the level 4 trigger (L4) used in this analysis.

For all events considered, the following detector components have to be operational in terms of read out and high voltage settings: CJC1 and CJC2, central and forward proportional chambers (CIP, COP and FPC), LAr, time-of-flight system (ToF) and the whole luminosity system (Lumi) including the electron taggers (ET).

As the positron and proton beams also contain so called satellite bunches before and after the colliding bunches, a cut on the z -coordinate of the reconstructed primary vertex is applied. The z -distance of the vertex from the nominal interaction point has to be smaller than 35 cm. This cut suppresses background events from interactions in the satellite bunches. The loss of events is corrected for in the luminosity calculation.

For all the remaining runs the integrated luminosity is calculated. Each run with a luminosity $\mathcal{L}^{int} > 0.1 \text{ nb}^{-1}$ is taken. Lower integrated luminosities are not accurately measured. The total integrated luminosity amounts to 59.3 pb^{-1} . Table 5.1 summarises the run selection and the resulting integrated luminosity.

| | |
|---------------------------------|--|
| Data taking period | 1999, 2000 nominal e^+p |
| Quality of runs | medium or good |
| Operational detector components | CJC, CIP, COP, FPC, LAr, ToF, Lumi, ET |
| Removal of satellite bunches | $ z_{vtx} - z_{nom} < 35$ cm |
| Minimal luminosity of runs | $\mathcal{L}^{int}(\text{run}) > 0.1$ nb $^{-1}$ |
| Total integrated luminosity | $\mathcal{L}^{int} = 59.3$ pb $^{-1}$ |
| Prescale corrected luminosity | $\mathcal{L}_{pc}^{int} = 51.1$ pb $^{-1}$ |

Table 5.1: *Basic run and event selection and resulting integrated luminosity. The last line shows the luminosity after correcting for trigger prescales as described in section 5.2.*

5.2 Photoproduction Selection and Trigger Requirements

Photoproduction is selected through detection of an energy deposition in the electron tagger at $z = -33.4$ m (ET33). This means that the positron is scattered by a very small angle ($\pi - \theta_{e'}$) < 5 mrad, such that the kinematic variables of the event can be reconstructed using the reconstructed energy of the scattered positron $E_{e'}$ and the positron beam energy E_e ,

$$Q_e^2 = 4 \cdot E_e \cdot E_{e'} \cdot \cos^2\left(\frac{\theta_{e'}}{2}\right) < 0.01 \text{ GeV}^2, \quad (5.1)$$

$$y_e = 1 - \frac{E_{e'}}{E_e} \cdot \sin^2\left(\frac{\theta_{e'}}{2}\right) \approx 1 - \frac{E_{e'}}{E_e}. \quad (5.2)$$

To get a reliable measurement of $E_{e'}$ the energy deposition must be fully contained in the ET33. This is assured if the x -coordinate of the deposited energy fulfils $|x_{33}| < 6.5$ cm [68].

The events are selected by the subtrigger S83. It is a combination of level 1 (L1) trigger elements from the z -vertex trigger, the DCRPh trigger and the luminosity system without any level 2 (L2) conditions:

The **z -Vertex Trigger** is based on the CIP, COP and the FPC to provide a rough information about the z -vertex position of an event. This is done by building rays from the hits of the 16 ϕ -sectors of the chambers. The intersections of these rays with the z -axis are filled into a histogram. Rays from real particles from a real interaction end up in the same or adjacent bins whereas combinatorial background is randomly distributed as can be seen from figure 5.1. More details can be found in [76, 77]. The subtrigger S83 uses the trigger element `zVtx_sig_1` which fires if the histogram shows a significant peak.

The **DCRPh Trigger** uses 10 wire layers of the CJC. The signals of these wires are compared with predefined track masks corresponding to charged particle trajectories in the $r\phi$ -plane. The number of negative and positive tracks above two programmable transverse momentum thresholds are counted separately. The DCRPh trigger is described in more detail in [78, 79]. The subtrigger S83 requires the trigger element `DCRPh_Tc` which fires if at least three track masks above $\gtrsim 450$ MeV are found.

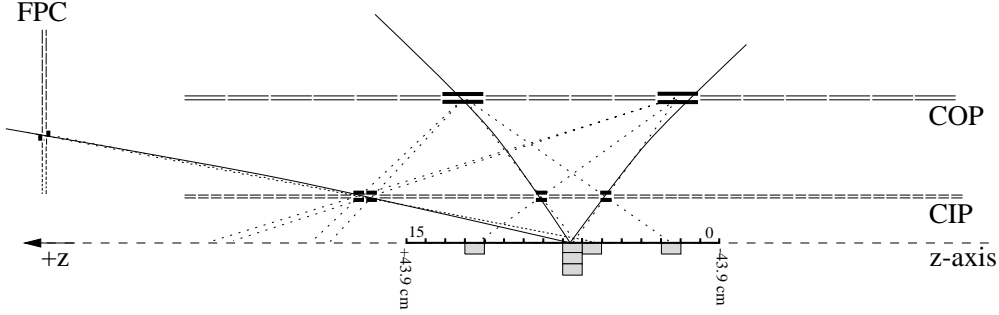


Figure 5.1: *The z-vertex trigger: Particle trajectories (full lines) cause hits in the double layers of CIP, COP and FPC. Rays through the pads (dotted lines) are extrapolated to the z-axis. Only rays from particle trajectories form a significant peak in the z-vertex histogram.*

The **Luminosity System Trigger** provides the trigger elements LU_ET and LU_PD_low.

The former fires if an energy deposition above a variable threshold ($E_{thr} \approx 6-9$ GeV) is found in the ET33. The latter is related in a similar way to energy in the photon detector, here the threshold is $E_{thr} \approx 5-7$ GeV. To trigger events with a scattered positron in the ET33 and to veto events from Bethe-Heitler processes, S83 uses (LU_ET && \neg LU_PD_low).

In addition the subtrigger S83 contains trigger elements from the time-of-flight system as a veto to suppress background from beam-gas and beam-wall events coming from outside the interaction region.

Because of high rates a prescale factor p is applied to the subtrigger 83. This means that only every p -th time the subtrigger has fired the event is accepted. The mean prescale in the analysed data is $\langle p \rangle = 1.16$. This is taken into account by downscaling the luminosity by this factor leading to a prescale corrected integrated luminosity of $\mathcal{L}_{pc}^{int} = 51.1$ pb $^{-1}$, as already mentioned in table 5.1.

Due to geometry and beam optics the ET33 has only a limited acceptance for positrons from photoproduction events. Besides the restriction of $Q^2 < 0.01$ GeV 2 due to the small scattering angle this acceptance is highly dependent on the inelasticity y and the exact beam parameters. A parametrisation of the acceptance has been determined by the H1 collaboration for several run periods as in [68] and is available for analysis from the H1 database. Figure 5.2 shows the y -dependence of the acceptance for all run periods considered in this analysis. Due to different beam conditions the acceptance has been slightly lower in 2000 than in 1999. Requiring $0.29 < y_e < 0.65$ assures that the acceptance is above 10% for all events in all run periods.

In the fourth trigger level (L4) the subtriggers from L1 and L2 are verified and the “open charm finder” HQSEL [80] is applied. Among various D mesons and the Λ_c in different decay channels, the D^* meson is searched for in the channel used in this analysis: $D^{*\pm} \rightarrow D^0 \pi_s^\pm \rightarrow K^\mp \pi^\pm \pi_s^\pm$. The vertex fitted tracks reconstructed from the CJC and the inner and outer z -chambers (CIZ, COZ) are used without using information from the CST. Different sets of cuts are applied for DIS and photoproduction. In this analysis events are accepted if a D^* candidate is found in the proper decay channel in the tagged

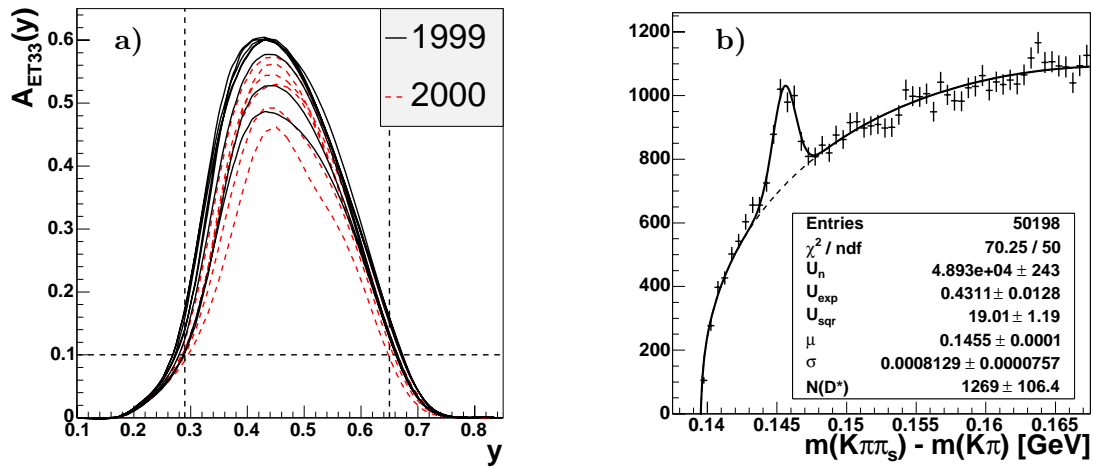


Figure 5.2: a) Acceptance of the ET33 for different run periods as a function of the inelasticity y . The parametrisations include also inefficiencies due to requiring the trigger elements (LU_ET && \neg LU_PD_low) and due to the cut $|x_{33}| < 6.5$ cm. Vertical lines indicate the selected y -region to achieve $A_{ET33} > 10\%$, shown as horizontal line. b) Distribution of the difference Δm between the invariant mass of the D^* candidate and the D^0 candidate after photoproduction selection and trigger requirements.

photoproduction mode. The applied cuts are listed in table 5.2. In the Monte Carlo simulation no L4 condition is required because the electron taggers are not fully simulated and therefore the prerequisite of HQSEL, significant energy in any of the electron taggers, cannot be properly taken into account. Therefore the L4 efficiency has to be determined from data.

Table 5.3 summarises all trigger and photoproduction conditions that an event must fulfil to be analysed further. Figure 5.2b) shows the resulting Δm distribution. The signal is on top of a high background. In section 5.3 it will be shown how the signal-to-background ratio can be improved by particle identification and further cuts on the D^* decay products and the event topology.

5.3 Improving the D^* Signal

5.3.1 Cuts Based on Particle Identification

The principles of particle identification using the specific energy loss per path dE/dx have been introduced in section 3.5. The likelihood LH of a track to be a specific particle has been defined in eq. 3.3.

To suppress combinatorial background from tracks assigned an obviously wrong mass hypothesis a cut on the LH values is applied for the tracks from the D^0 decay: $LH(K, \pi) > 0.01$. For kaons with momenta $0.8 < p(K) < 2.0$ GeV the cut is lowered to $LH(K) > 0.002$ as will be explained in section 5.5.4. Because the parametrisation of eq. 3.2 does not describe the dE/dx -spectrum of pions with low momenta very well (figure 3.4b)) and

| <i>Prerequisites</i> | |
|---|--|
| subtrigger | 1, 2, 4, 43, 44, 45, 61, 82, 83, 84, 100 or 108 |
| tagged γp | $E_{33} > 3 \parallel E_{44} > 5 \parallel E_8 > 5 \text{ GeV}$ |
| z -vertex | $ z < 40 \text{ cm}$ |
| <i>Track requirements</i> | |
| K, π | $ d'_{ca} < 4 \text{ cm}$ $r_{end} - r_{start} > 15 \text{ cm}$ $\chi_{xy}^2 < 50$ $p_t > 200 \text{ (250) MeV}$ |
| π_s | $r_{end} - r_{start} > 10 \text{ cm}$ $p_t > 100 \text{ MeV}$ |
| <i>D^* decay selection</i> | |
| D^0 | $1.764 < m(K\pi) < 1.964 \text{ GeV}$ |
| D^* | $p_t > 1.4 \text{ GeV}$ $\Delta m = m(K\pi\pi_s) - m(K\pi) < 170 \text{ MeV}$ |

Table 5.2: Cuts of the L4 open charm finder HQSEL applied in tagged photoproduction mode for the channel $D^{*\pm} \rightarrow D^0\pi_s^\pm \rightarrow K^\mp\pi^\pm\pi_s^\pm$. The higher p_t -cut on K and π tracks shown in brackets has been applied during the main part of 1999 data taking. Besides the χ^2 of the track fit in the xy plane all cuts are softer than in the final analysis where the cut on the energy E_{33} in the ET33 is achieved implicitly by the cut on y_e .

| | | |
|-----------|---|---|
| ET33 | $Q^2 < 0.01 \text{ GeV}^2$ $0.29 < y_e < 0.65$ | implicit by small scattering angle achieves $\mathcal{A}_{\text{ET33}} > 10\%$ |
| | $ x_{33} < 6.5 \text{ cm}$ | reliable $E_{e'}$ for y measurement |
| L1: S83 | zVtx_sig_1 DCRPh_Tc LU_ET -LU_PD_low | significant peak in z -vertex histogram 3 track masks with $p_t \gtrsim 450 \text{ MeV}$ energy in ET33 no Bethe-Heitler process |
| L4: HQSEL | $D^{*\pm} \rightarrow D^0\pi_s^\pm \rightarrow K^\mp\pi^\pm\pi_s^\pm$ | in tagged γp mode |

Table 5.3: Photoproduction selection and required trigger conditions.

because around 10% of them have no dE/dx measurement, no cut is applied on $LH(\pi_s)$. To remove obvious kaons and protons, tracks with a very high dE/dx value are rejected, $dE/dx(\pi_s) < f_{dE/dx}(p(\pi_s), m_\pi) + 1$ (cf. figure 3.4b)). Tracks without a reliable dE/dx measurement, i. e. with less than 10 usable hits, are always accepted.

The signal-to-background ratio improves from 0.26 (figure 5.2b)) to 0.34 (figure 5.4a)). The dE/dx -cuts are not applied in the Monte Carlo simulation because no appropriate dE/dx simulation was available. Their efficiency will be determined from data.

5.3.2 Further Background Suppression

If D^* mesons evolve from charm quarks produced in the hard interaction, they carry a major part of the produced transverse energy. This event property can be used to

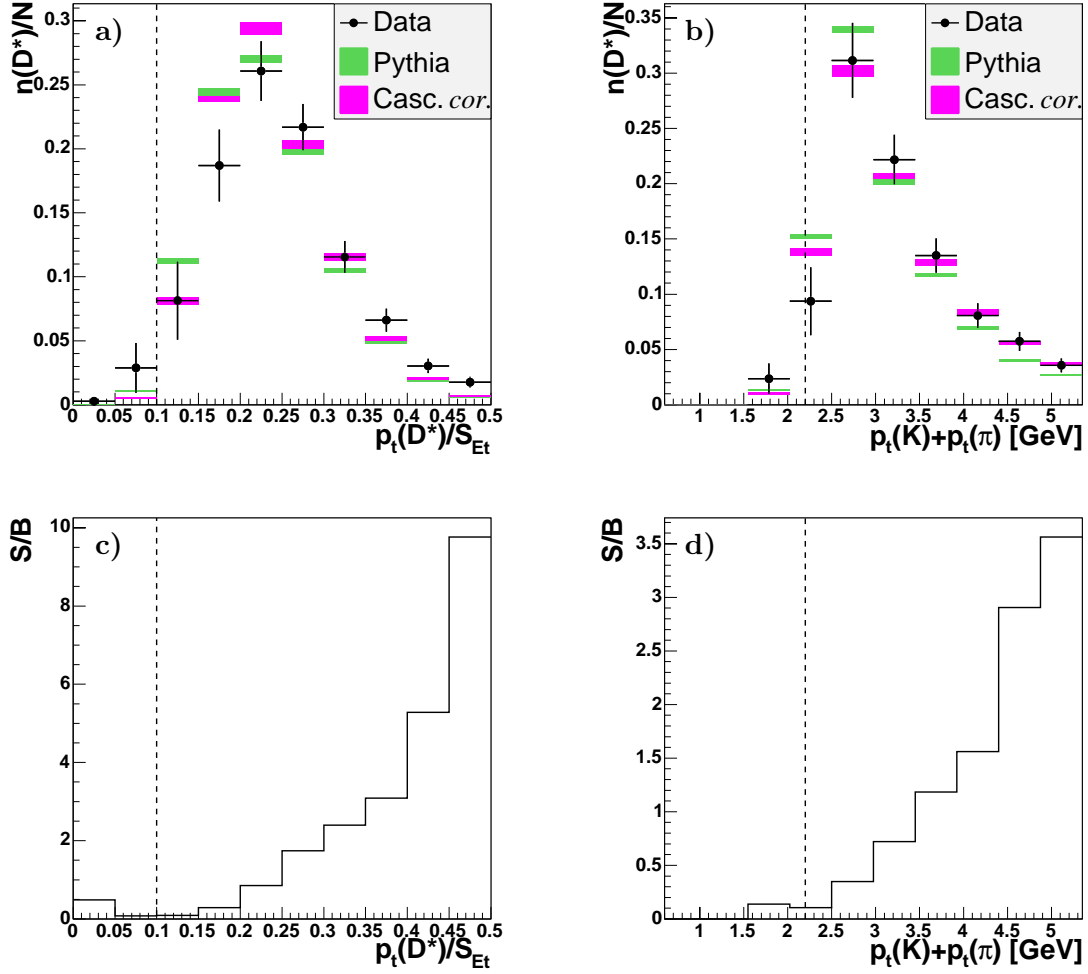


Figure 5.3: *Distribution of the values $p_t(D^*)/S_{Et}$ (a) and $p_t(K)+p_t(\pi)$ (b) after the cut on the other quantity, normalised to the total number of D^* mesons. The cuts are indicated by dashed vertical lines. The signal-to-background ratios of the D^* fits of the data in each bin are shown in (c) and (d).*

The CASCADE distributions are corrected as introduced in the next section.

distinguish combinatorial background from the signal. Therefore the scalar sum of the transverse energy of all particles in the hadronic final state (HFS),

$$S_{Et} = \sum_{HFS}^{\theta > 10^\circ} \sin \theta_i E_i, \quad (5.3)$$

is compared with the transverse momentum of the D^* candidate [7], as shown in figure 5.3a). In order not to pick up any proton remnant, the sum is restricted to HFS particles with $\theta > 10^\circ$. Without losing much of the signal the cut $p_t(D^*)/S_{Et} > 0.10$ is applied to the D^* candidates.

| <i>Particle identification</i> | |
|---------------------------------------|--|
| K | $LH > 0.002, \quad 0.8 < p(K) < 2.0 \text{ GeV}$ $LH > 0.01, \quad p(K) < 0.8 \parallel p(K) > 2.0 \text{ GeV}$ |
| π | $LH > 0.01$ |
| π_s | $dE/dx(\pi_s) < f_{dE/dx}(p(\pi_s), m_\pi) + 1$ |
| <i>D^* properties</i> | |
| $p_t(D^*)/S_{Et} > 0.10$ | |
| $p_t(K) + p_t(\pi) > 2.2 \text{ GeV}$ | |

Table 5.4: Summary of the cuts applied to improve the D^* signal. The cuts for particle identification are applied only to tracks with a dE/dx measurement.

As the π_s carries only a small fraction of the transverse D^* momentum, most of it has to come from the K and π tracks as shown in figure 5.3b). For that reason a requirement on the scalar sum of their transverse momenta, $p_t(K) + p_t(\pi) > 2.2 \text{ GeV}$, further suppresses background [81].

Data and Monte Carlo distributions of both quantities agree satisfactorily within the uncertainties. In the figures 5.3c-d) the signal-to-background ratios of the D^* fits resulting in the distributions of the figures 5.3a-b) can be seen. It indicates a small loss of real D^* mesons for the proposed cuts. Together with the fact of a large background at low values of $p_t(D^*)/S_{Et}$ and $(p_t(K) + p_t(\pi))$ an improvement in the overall signal-to-background ratio is achieved. This can be seen comparing the figures 5.4a-b) which show the Δm distributions before and after both cuts.

Tightening these cuts would further increase the background suppression. But the quantities are not very well reproduced by the simulations and even behave slightly different for PYTHIA and CASCADE. To avoid a systematic dependence of the resulting cross sections, the proposed soft cuts are chosen. The signal-to-background ratio improves from 0.34 (figure 5.4a)) to 0.47 (figure 5.4b)).

Table 5.4 summarises the cuts applied to improve the D^* signal. The final D^* sample with all cuts applied that are listed in the tables 3.1, 4.2, 5.3 and 5.4 is shown in figure 5.4b). In total 24578 D^* candidates satisfy the cuts, resulting in 1154 ± 84 D^* mesons from the fit.

5.4 Comparison of Data and Simulation

To determine the efficiencies of the D^* reconstruction and the L1 triggers a simulation of the H1 detector is used as described in section 3.6. Therefore it has to be ensured that the simulation describes the data.

In this section first the track resolution is investigated by means of the D^0 width and then the distribution of quantities relevant for reconstruction efficiencies is compared between data and simulation.

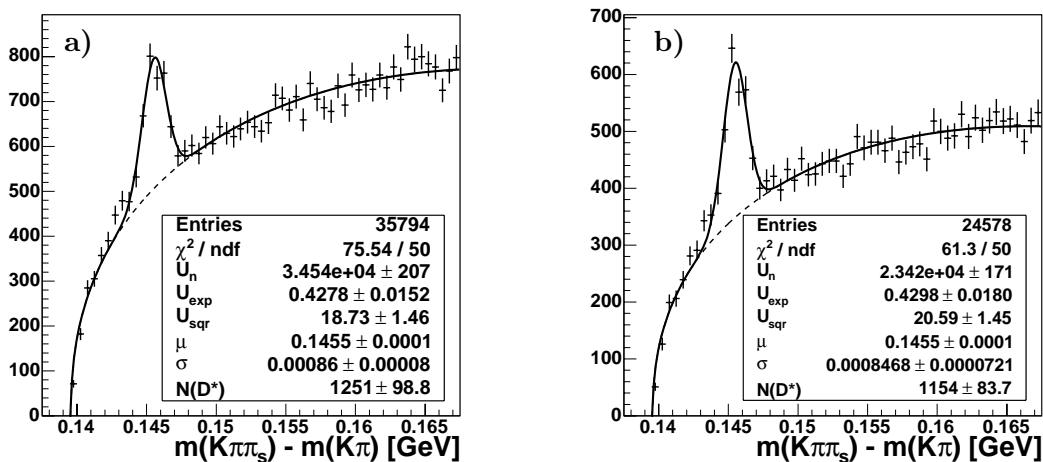


Figure 5.4: Distributions of Δm and results of the D^* fit: after the cuts for particle identification, but before the cuts on $p_t(D^*)/S_{Et}$ and $p_t(K) + p_t(\pi)$ (a), and for the final D^* meson selection (b).

5.4.1 Track Resolution: D^0 Width

The D^* and D^0 mesons both have widths far below the experimental resolution. From the D^* signals in the Δm distributions in simulation and data (see figures 4.2 and 5.4) it can be deduced that the track resolution is overestimated in the simulation. This influences the width of the D^0 signal, shown in figure 5.5. In order not to bias the distribution in data by the cut on $m(K\pi)$, applied in the L4-finder HQSEL (cf. table 5.2), for this comparison events in data are taken only if on L4 they have been triggered independently of HQSEL.

The standard deviation of the Gaussian D^0 signal is fitted to be $\sigma = 27.7 \pm 2.7$ MeV in the data and $\sigma = 23.7 \pm 0.7$ MeV in the simulation, as can be seen in figure 5.5. The cut of ± 80 MeV around the nominal D^0 mass is almost three times larger than the width of the data. Assuming a perfect Gaussian signal, only less than 0.5% of the signal is cut in data and in the simulation the smaller width leads to a loss smaller than 0.1%. This difference is negligible compared to other uncertainties and is not considered further.

5.4.2 Quality of D^* and Track Simulation

In this section distributions of D^* and track quantities are compared between data and the simulation of events generated by the Monte Carlo generators PYTHIA and CASCADE.

The events in the data are selected as described above. In the simulation the acceptance of the electron tagger is taken into account as described in section 3.6. Additional weights are applied to take into account the different mean prescale factors of the sub-trigger 83, averaged for each period that has its own acceptance parametrisation. This is needed since the assignment of a specific amount of generated events to be simulated under specific detector conditions as described in 3.6 takes into account the luminosity without considering prescales. After applying these additional weights the generated events finally are effectively distributed over the different run periods in the same way as the luminosity

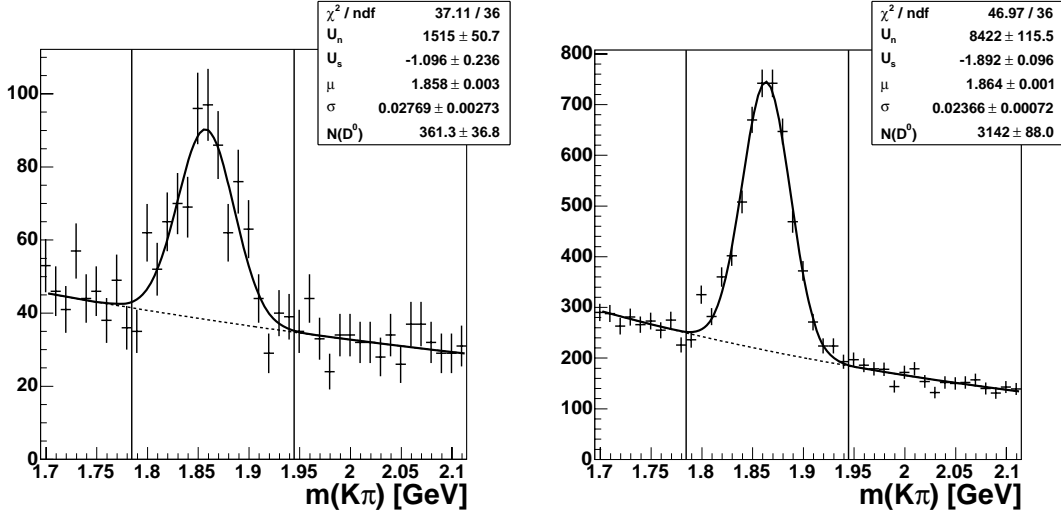


Figure 5.5: The D^0 signal in the invariant mass distribution of the kaon-pion pair of an $L4$ -unbiased sample in data on the left and in the inclusive Monte Carlo simulation on the right. Vertical lines indicate the cut ± 80 MeV around the nominal D^0 mass applied in the D^* selection. The distribution is fitted to a Gaussian for the signal and an exponential for the background.

of the data. The mean prescale factors vary between 1.02 and 1.38 and are $\langle p \rangle = 1.04$ for 1999 and $\langle p \rangle = 1.20$ for 2000.

Since the parametrised tagger acceptance includes the efficiency of the trigger elements of the luminosity system, LU_ET and LU_PD_low, only the trigger elements zVtx_sig_1 and DCRPh_Tc are required in the simulation. The level 4 trigger requirements are also ignored since the $L4$ efficiency is quite flat as shown in section 5.5.2.

For the PYTHIA generator, different charm production processes have been generated separately, i. e. direct, resolved and excitation. For the comparison of the combined sample with the data, the Δm distributions for each process and each analysis bin are normalised to the individual cross section of the process¹ and then added. The number of reconstructed D^* mesons per luminosity, $N(D^*)/\mathcal{L}$, is determined for each bin by the fit described in section 4.3.1.

Finally a shape comparison of the data and the Monte Carlo is achieved by normalising all distributions to the total number of reconstructed D^* mesons, $N(D^*)$ and $N(D^*)/\mathcal{L}$ respectively.

In figure 5.6a) the $p_t(D^*)$ distribution is shown and compared to predictions of the CASCADE and PYTHIA event generators. CASCADE produces a harder spectrum than the data. Therefore the prediction of CASCADE is modified.

The modification is obtained by calculating the cross section as a function of $p_t(D^*)$ and fitting an exponential function to the ratio of the result and the CASCADE prediction. The correction factor lies between 1.2 for $p_t(D^*) \approx 2$ GeV and 0.2 for $p_t(D^*) \approx 14$ GeV and is applied as an additional event weight for the events simulated by CASCADE.

¹This is done by dividing through the integrated luminosity \mathcal{L} which is calculated from the total number of generated events and the total cross section computed by the Monte Carlo generator.

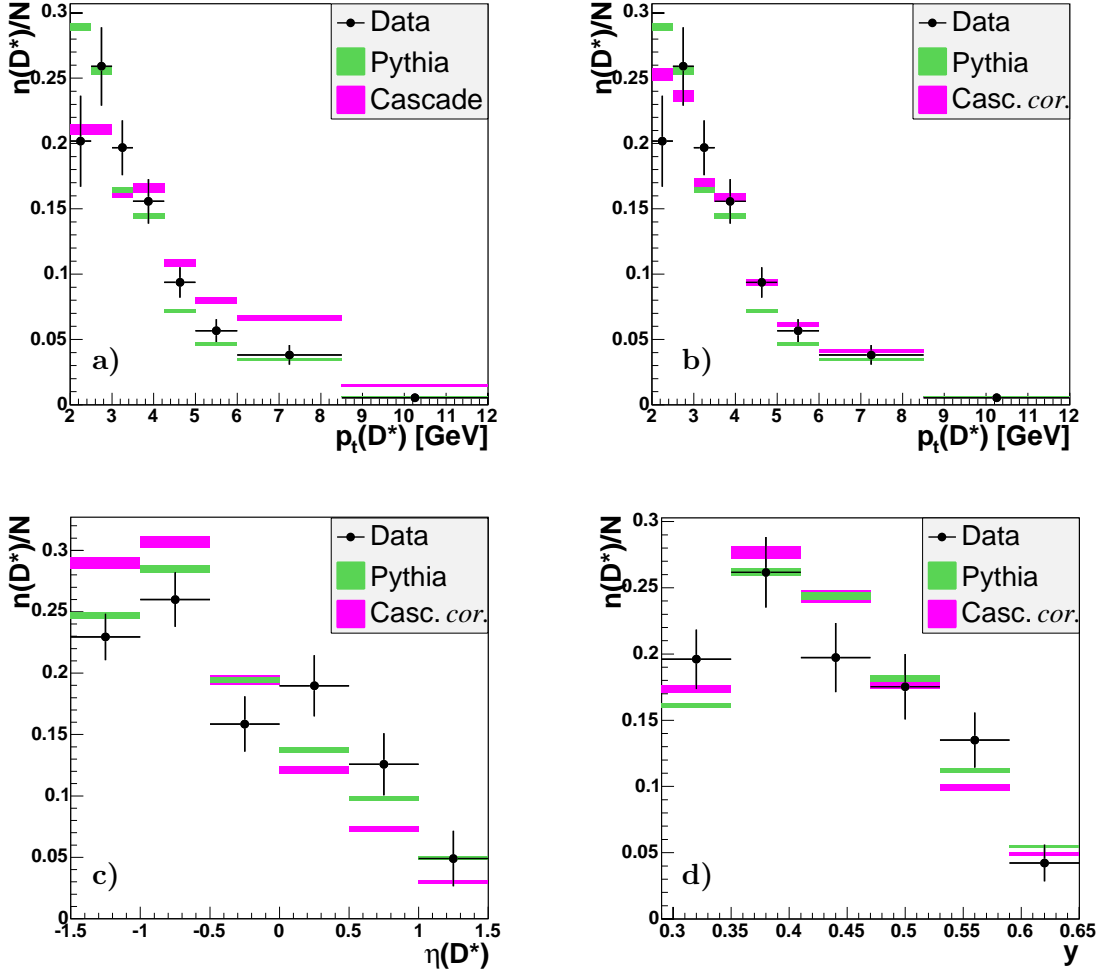


Figure 5.6: Comparison of $p_t(D^*)$, $\eta(D^*)$ and inelasticity y in the data and in the simulations *PYTHIA* and *CASCADE*. Figure (a) shows $p_t(D^*)$ before the correction of the *CASCADE* simulation that is applied in the other shown distributions.

Figure 5.6b) shows the $p_t(D^*)$ distributions of the data and the simulations after the correction for *CASCADE*. Better agreement of *CASCADE* with the data is achieved, the largest remaining difference is seen in the lowest p_t bin, for both *PYTHIA* and *CASCADE*. In the following, all distributions of reconstructed quantities of the *CASCADE* simulation use this correction.

Figure 5.6c-d) compare the distributions of the pseudorapidity $\eta(D^*)$ and the inelasticity y of the data and the simulations. The inelasticity is well reproduced by the simulations, but mainly *CASCADE* falls too steeply towards high η . This effect is a little more pronounced after the p_t -correction.

To test the detector simulation and the *PYTHIA* and *CASCADE* models in more detail, in figure 5.7a-d) the distributions of the radial track length, the azimuthal and the polar angles and the transverse momentum of the kaon track in the data are compared

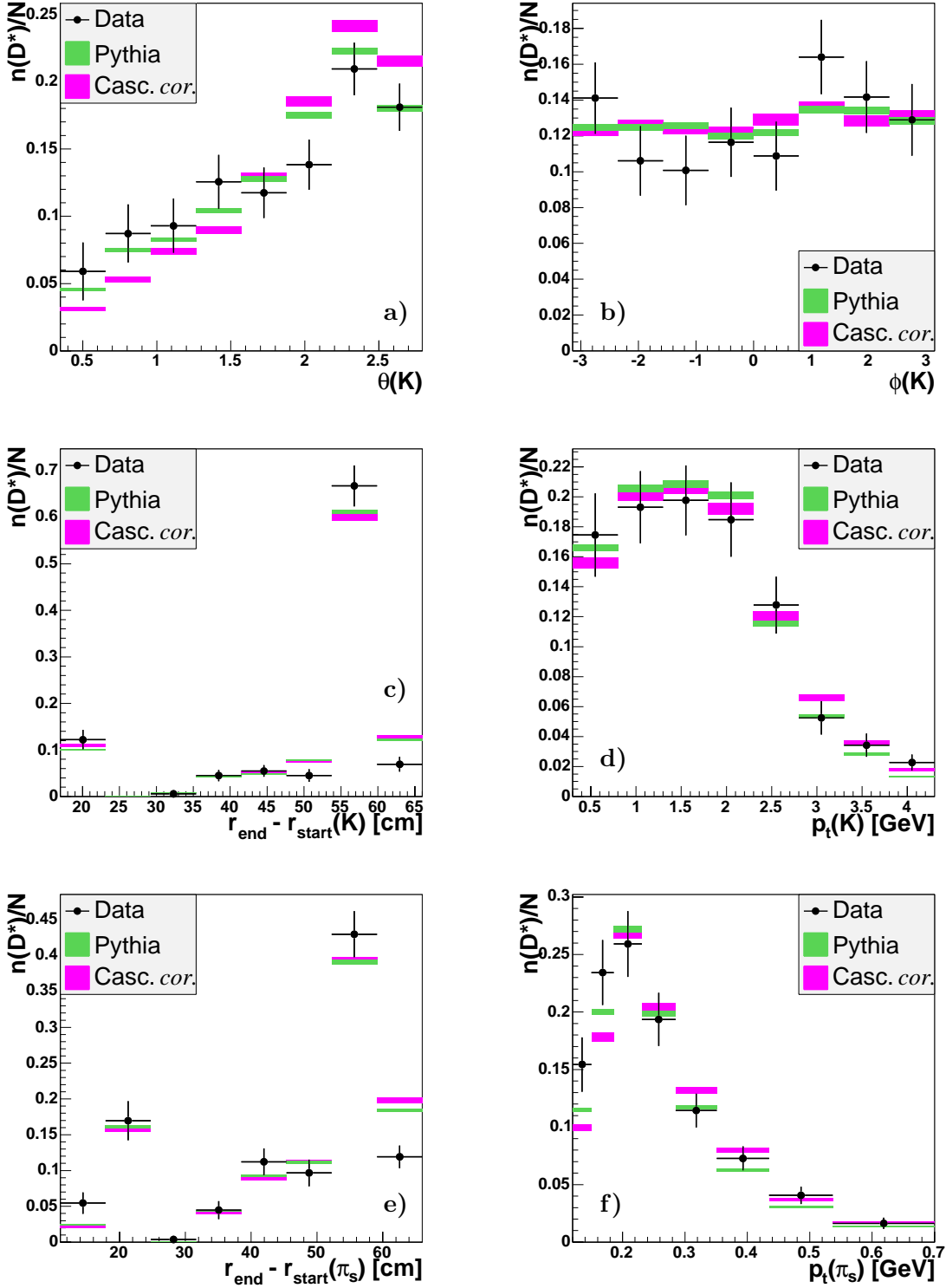


Figure 5.7: The polar angle θ , the azimuthal angle ϕ , the radial length $r_{\text{end}} - r_{\text{start}}$ and the transverse momentum p_t of the kaon track are shown in (a-d). Figures (e-f) show the radial length and the transverse momentum of the slow pion track.

with the simulations of both Monte Carlo event generators PYTHIA and CASCADE. Since the pion track from the D^0 decay shows similar properties as the kaon, it is not shown separately. However, the slow pion track has a different momentum range and its track length and transverse momentum distributions are shown in figure 5.7e-f).

All distributions are reasonably reproduced by the simulations, PYTHIA is closer to the data than CASCADE. The $\phi(K)$ distribution is almost flat as expected. A small asymmetry of the simulated distribution is caused by taking into account temporary broken sectors of the central tracking detectors.

The majority of the kaon tracks are longer than 50 cm, thus passing both parts of the CJC. Due to lower momenta this effect is less prominent for slow pion tracks. The tendency that tracks are shorter in data than in the simulations might be caused by problems in linking track segments in CJC1 with segments in CJC2 due to imperfect alignment of the chambers.

The p_t and mainly the θ distributions of the tracks show differences between both simulations. For CASCADE the p_t -spectrum is slightly harder than for PYTHIA, but both are consistent with the data. The fact that both simulations have a steeper rise towards large $\theta(K)$ than the data reflects that $\eta(D^*)$ falls more steeply towards large η . Both effects are less prominent for PYTHIA than for CASCADE.

Finally it can be concluded that the Monte Carlo simulation based on the PYTHIA generator describes the data reasonably well and can be used to determine efficiencies. CASCADE generates a transverse momentum distribution for the D^* meson that is too hard and has to be adjusted to the data. The pseudorapidity distribution falls too steeply towards higher η in both simulations.

5.5 Correction Factors

To obtain cross section measurements from the selected D^* mesons, their number has to be corrected for inefficiencies in triggering, reconstruction and event selection and due to the limited acceptance of the electron tagger. This will be done by applying the efficiency ϵ obtained by a combination of the different sources:

$$\epsilon = \epsilon_{L1} \cdot \epsilon_{L4} \cdot \epsilon_{rec} \cdot \mathcal{A}_{ET33}. \quad (5.4)$$

Here ϵ_{L1} and ϵ_{L4} are the efficiencies of the trigger levels L1 and L4, respectively, ϵ_{rec} is the reconstruction efficiency and \mathcal{A}_{ET33} the acceptance of the ET33. They are determined in the following.

Whenever a quantity is determined from Monte Carlo simulation, the PYTHIA sample is used and the different processes are combined as described in section 5.4.

5.5.1 L1 Trigger Efficiency

The level 1 trigger efficiency ϵ_{L1} covers the efficiency of the trigger elements `zVtx_sig_1` and `DCRPh_Tc`. The trigger elements of the luminosity system are contained in the electron tagger acceptance and the veto trigger elements are assumed to be 100% efficient.

The trigger efficiency is determined from the simulation as the ratio of the number of reconstructed D^* mesons with a positive trigger decision and the number of reconstructed

D^* mesons in total. The combinatorial background in Monte Carlo is small and has similar kinematic properties as the signal because it also comes from charm production events. Therefore, and to avoid possible fluctuations from the D^* fit, all reconstructed D^* candidates in the signal region, $143 < \Delta m < 148$ MeV, are taken into account.

To cross check the trigger simulation with data, events are selected that have been triggered by one of the subtriggers 50, 67 or 101. These subtriggers are mainly based on energy depositions in the LAr and the SpaCal. Since the L4 finder HQSEL is not applied to these subtriggers, it is ensured that the events passed L4 independent of HQSEL. Otherwise the event sample would not be independently triggered. Due to the low statistics, all D^* candidates up to $\Delta m < 165$ MeV are counted. As the background events of the data have other event signatures and possibly slightly different trigger efficiencies, the selected sample is only a rough cross check.

The total trigger efficiency in data is $\epsilon_{L1}^{data} = (93.3_{-1.1}^{+1.0})\%$ which is slightly higher than the result obtained from Monte Carlo, $\epsilon_{L1}^{mc} = 90.9\%$. This effect is also observed in figure 5.8 which shows efficiencies of both trigger elements, `zVtx_sig_1` and `DCRPh_Tc`, separately as functions of $p_t(D^*)$, $\eta(D^*)$ and $W_{\gamma p}$. This discrepancy cannot be attributed to one trigger element or to a specific region of phase space. It could well be due to different kinematic properties of the independent reference sample and the selected D^* data or even due to statistical fluctuations in the reference data sample.

A systematic uncertainty of 4% is attributed to the trigger efficiency determined from the PYTHIA simulation. This covers the observed difference between data and simulation of the total efficiency as well as fluctuations relevant for different regions of phase space.

5.5.2 L4 Trigger Efficiency

The tracks available for this analysis are improved by offline calibration of the tracking devices and by including CST hit information in the track fit. Thus they differ slightly from the tracks which the software filter HQSEL uses for triggering on level 4 (L4) and some events are lost on L4.

The efficiency that a D^* meson is found in HQSEL in the decay chain used is determined from the data as a global factor. A reference sample of D^* events is defined that have been triggered on L4 independently from HQSEL. This is done by selecting events that belong to at least one of the event classes 4, 8 or 13. Class 4 (“high Q^2 ”) and 8 (“high p_t central”) both require a hard scale in the event and class 13 (“diffraction”) selects events with a rapidity gap.

The number of D^* mesons in the reference sample and in the subset with a positive HQSEL decision is determined by a D^* fit with fixed parameters μ , σ and u_s . The result is $\epsilon_{L4} = (96.9 \pm 3.9)\%$. To calculate the error, the correlation between the fitted number of D^* mesons with and without the positive HQSEL decision is taken to be $\rho = \sigma_{with}^2 / \sigma_{w/o}^2$. In addition the uncertainty from binomial statistics is added in quadrature.

The application of a global efficiency ϵ_{L4} is valid only if the efficiency is independent of quantities like the transverse momentum or the pseudorapidity of the D^* meson. To verify this figure 5.9 shows the result of a determination of ϵ_{L4} as a function of these quantities. Due to low statistics in the data the efficiency is calculated once in the same way as the overall efficiency and once by just counting events in the signal region instead of performing a D^* fit. The values determined in the signal region are below the values from the fits, but the latter are close to the global value. This indicates that the efficiency is

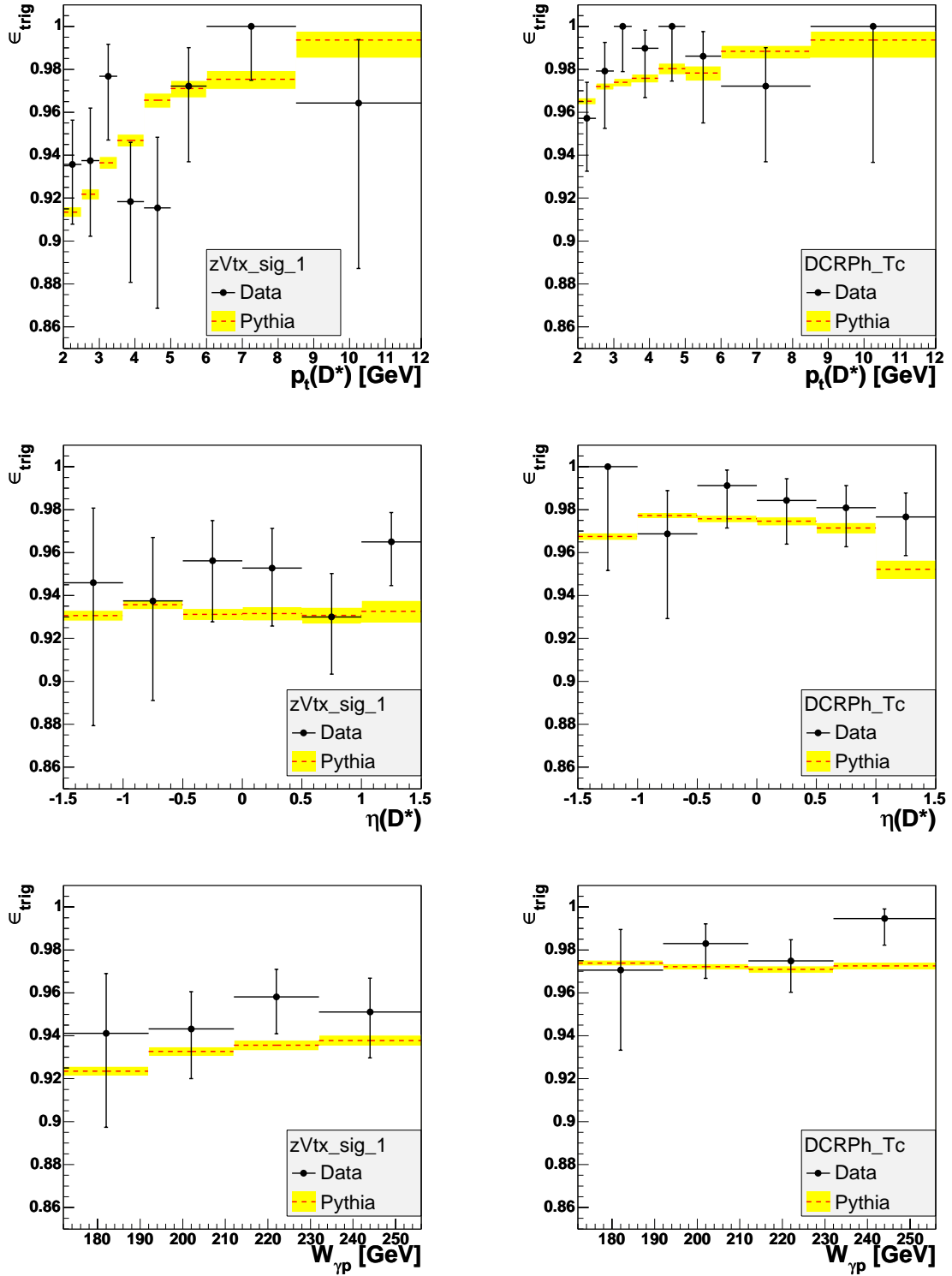


Figure 5.8: Trigger efficiencies as determined from Monte Carlo compared with the cross checks obtained from data, trigger element `zVtx_sig_1` on the left and `DCRPh_Tc` on the right. Note that the ordinate starts at 0.85.

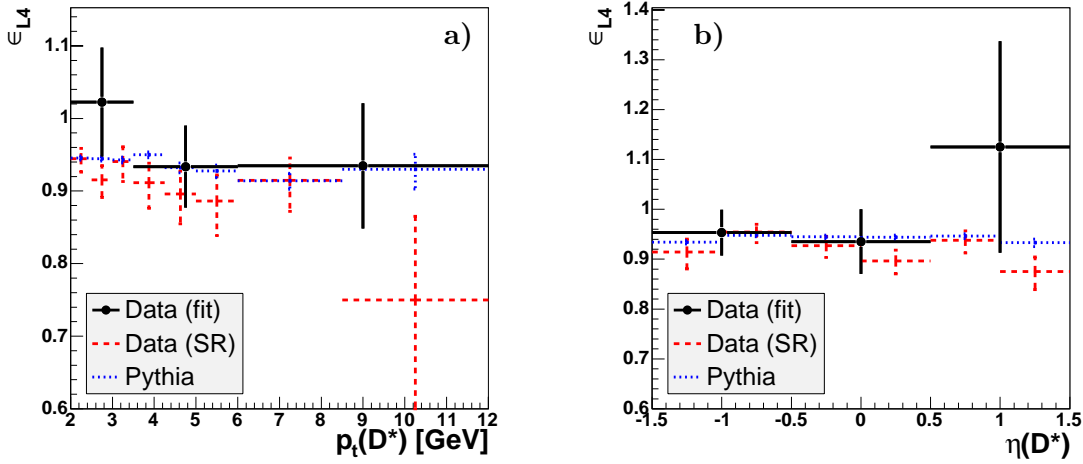


Figure 5.9: Efficiencies of the trigger level 4 as a function of $p_t(D^*)$ (a) and $\eta(D^*)$ (b) determined from data by D^* fits and by counting events in the signal region (SR) compared with the result of the PYTHIA simulation. Note the suppressed 0 on the scales of the y-axes.

lower for the background: Random track combinations in the background can migrate out after the improved track reconstruction and calibration, but new random combinations can hardly migrate in because they have already been lost at L4.

At high η and low p_t the efficiency determined by fits reaches unphysically high values $\epsilon_{L4} > 1$. These are the regions with the worst signal-to-background ratios and the largest relative uncertainties of the fit result. This leads to large uncertainties of ϵ_{L4} such that even these unphysical values are consistent with the global value.

Concluding, the assumption of ϵ_{L4} being independent of other quantities is valid within the stated error. This is also confirmed by the efficiency determined from the PYTHIA simulation which is also shown in figure 5.9.

The systematic uncertainty assigned is the error which results from the fits and is propagated as stated above, i. e. it amounts to 4%.

5.5.3 Electron Tagger Acceptance

The acceptance of the electron tagger is calculated as a mean acceptance by integrating the acceptance function over the visible range (cf. table 5.6) using a Monte Carlo event generator:

$$\mathcal{A}_{\text{ET33}} = \frac{\sum_{N^{gen}} w_i \cdot a_{33}(y_i, r_i)}{\sum w_i}. \quad (5.5)$$

Here N^{gen} is the number of generated events in the considered kinematic region, a_{33} is the acceptance parametrised as a function of the inelasticity y and the run period r (cf. figure 5.2). This acceptance includes inefficiencies of the trigger elements LU_ET and LU_PD_low. The inelasticity and the run period of the generated event are denoted y_i and

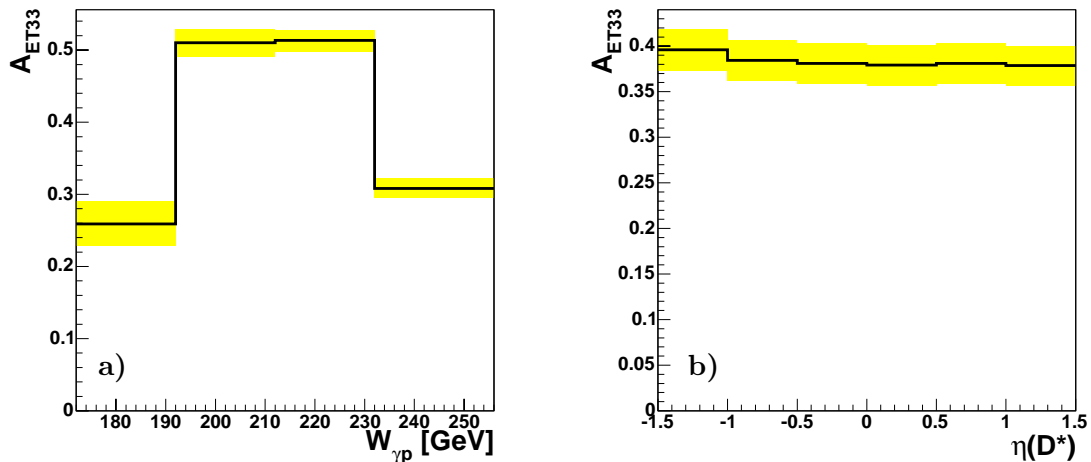


Figure 5.10: Mean acceptance of the electron tagger in bins of the centre-of-mass energy $W_{\gamma p}$ (a) and the pseudorapidity $\eta(D^*)$ (b). The systematic uncertainties are indicated as error bands.

r_i . The weights w_i are the inverse mean prescale factors of S83 for each run period. Thus the generated events are effectively distributed over the different run periods in the same way as the luminosity of the data.

The total acceptance in the visible range amounts to $\mathcal{A}_{\text{ET33}} = 38.6\%$. Figure 5.10 shows the acceptance in bins of $W_{\gamma p}$ and $\eta(D^*)$. The former reflects the trivial relation between y and $W_{\gamma p}$ and the latter indicates that the pseudorapidity distribution also depends slightly on y . Other $\mathcal{A}_{\text{ET33}}$ distributions are flat.

The uncertainty of the absolute energy scale of the electron tagger, $\sigma(E_{e'})/E_{e'} \approx 1.5\%$, and uncertainties in the knowledge of the exact beam optics of the HERA machine lead to a systematic uncertainty of the tagging acceptance. Its size is determined by varying the energy scale and the beam parameters within their errors as described in [68]. The result is a systematic uncertainty of 5.8% for the visible range in total and varies between 2.9% and 11.9% for bins in $W_{\gamma p}$ as indicated in figure 5.10a).

5.5.4 Reconstruction Efficiency

The reconstruction efficiency is determined as a product of efficiencies, $\epsilon_{rec} = \epsilon'_{rec} \cdot \epsilon_{\text{dEdx}}$. Here ϵ_{dEdx} denotes the efficiency of the cuts for particle identification which is determined from the data and ϵ'_{rec} is the efficiency of all other selection cuts and the event reconstruction itself. It is determined from the simulation as

$$\epsilon'_{rec} = \left. \frac{N^{rec}}{N^{gen}} \right|_{vis}. \quad (5.6)$$

Here N^{rec} is the number of reconstructed D^* mesons determined by the D^* fit as described in section 4.3.1 and N^{gen} is the number of generated D^* mesons in the analysed decay chain. Both numbers are determined in the visible range (table 5.6) and for differential

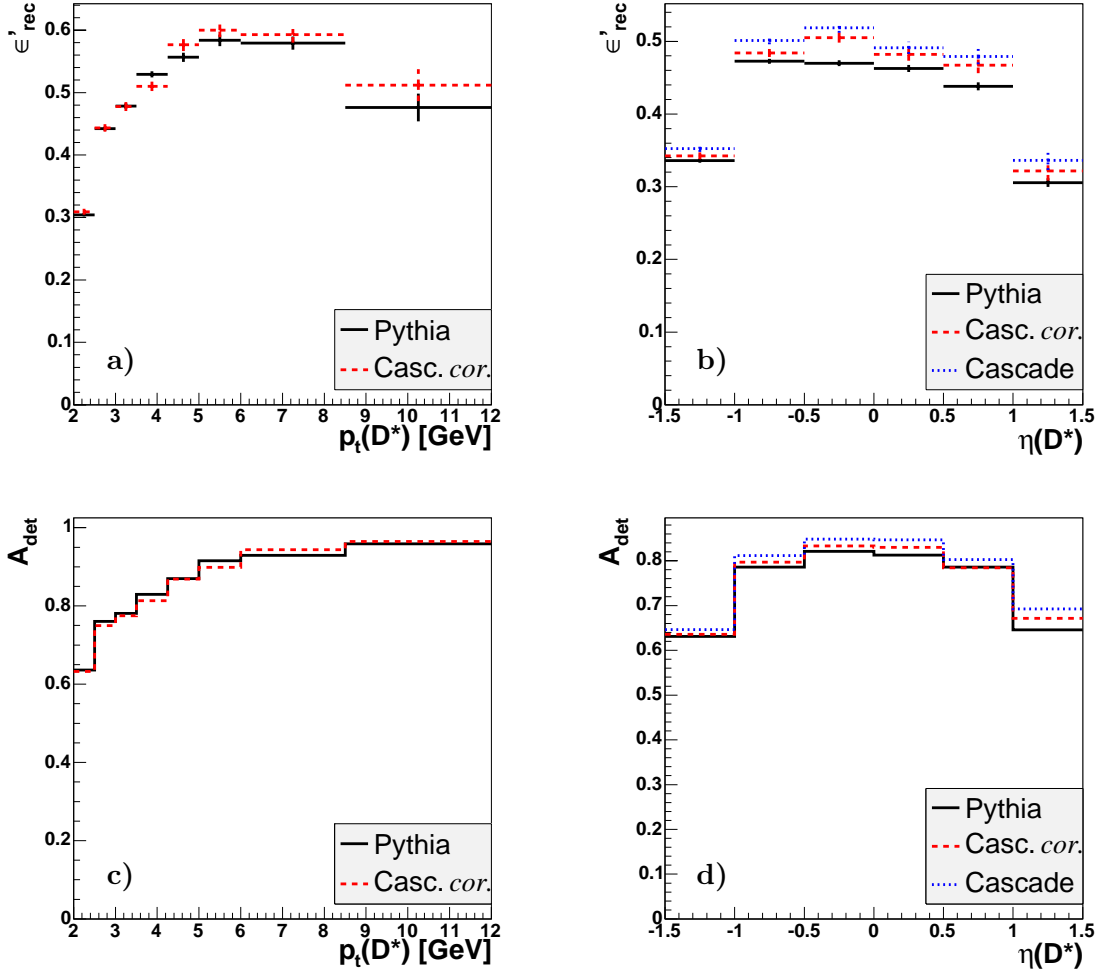


Figure 5.11: *Reconstruction efficiencies as determined from the PYTHIA and the CASCADE simulations in bins of $p_t(D^*)$ (a) and $\eta(D^*)$ (b). The error bars indicate the uncertainty of the number of reconstructed D^* mesons obtained by the D^* fit. The detector acceptance which is a part of the efficiency is shown in (c) and (d).*

efficiencies in the corresponding bin. In this way possible migration effects are also taken into account, though they are small and of the order of a few per cent for D^* quantities.

The chosen definition of the reconstruction efficiency corrects simultaneously for two effects, the efficiency of reconstructing vertex fitted tracks and the limited detector acceptance for D^* mesons due to the cuts on the transverse momenta p_t and the polar angles θ of the D^* decay tracks.

The acceptance only, $A_{det} = N_{gen}^{acc}/N_{gen}$, is shown as a function of $p_t(D^*)$ and $\eta(D^*)$ in the figures 5.11c-d). N_{gen}^{acc} denotes the number of those generated D^* mesons whose decay tracks fulfil the momentum and angular requirements (cf. table 4.2). The acceptance is lowest ($\approx 60\%$) at low $p_t(D^*)$ where the decay tracks also have low momentum and do not fulfil the minimal transverse momentum cuts. The acceptance is also reduced at large and

small pseudorapidities since the decay tracks can have polar angles θ outside the required region $20^\circ < \theta < 160^\circ$. The acceptance as a function of $\eta(D^*)$ has been calculated with CASCADE before and after the p_t correction. The result is shown in figure 5.11d). The effect of the correction is of the same size as the difference that remains between PYTHIA and the corrected CASCADE, but is apparent for all $\eta(D^*)$. As expected the p_t correction has no effect on the acceptance as a function of $p_t(D^*)$. Here PYTHIA and CASCADE agree with each other very well (figure 5.11c)).

The reconstruction efficiency in the total visible range amounts to $\epsilon'_{rec} = 41.1\%$ if determined with the PYTHIA simulation and to $\epsilon'_{rec} = 42.2\%$ if determined with the p_t -corrected CASCADE simulation (43.7% without the p_t correction).

The figures 5.11a-b) show the reconstruction efficiency as a function of the transverse momentum $p_t(D^*)$ and the pseudorapidity $\eta(D^*)$. Comparing the efficiencies and the detector acceptances, the inefficiencies of the track reconstruction and of the track quality requirements can be deduced. In general between one half and one third of the inefficiency is due to the limited detector acceptance. The track reconstruction efficiencies are largest at low transverse momentum and large absolute values of the pseudorapidity. Low momentum tracks can be lost due to multiple interaction or fail in the vertex fit. At large $|\eta(D^*)|$ the D^* decay tracks can have small radial lengths and either fail to be reconstructed or do not fulfil the track length requirement. At large $p_t(D^*)$ D^* candidates fail the selection due to the cut around the D^0 mass due to reduced track resolution.

The uncertainty of the simulation is taken into account by assigning a systematic uncertainty of 11%. This value is taken from [81] and results from the following consideration: In the simulation about 6% of charged particles in the momentum range of the kaon and pion from the D^0 decay and about 10% of charged particles in the momentum range of the π_s are not reconstructed due to interaction with matter or because the vertex fit is not acceptable. To account for these effects being properly described by the simulation, half of the inefficiency is taken as systematic uncertainty. Assuming these values are maximally correlated they have to be added to derive the uncertainty of the reconstruction efficiency of D^* mesons.

The detector acceptances and therefore the reconstruction efficiencies differ between both simulations CASCADE and PYTHIA. Since it is unknown which model is correct, an uncertainty has to be assigned on the decision to use PYTHIA to determine the efficiency. This model uncertainty includes also the (small) model dependencies of the determination of the trigger efficiencies and the electron tagger acceptances and is quantified in section 5.6.

Efficiency of the dE/dx Cuts

The cuts on dE/dx and the likelihood LH derived from dE/dx are designed to remove only obviously misidentified particles without losing any signal.

From figure 3.4b) it can be seen that the cut on the dE/dx value of the π_s does not reject real pions and thus its efficiency is 100%.

This is different for the LH values. Assuming that the parametrisation given in eq. 3.2 exactly describes the mean values of dE/dx for all momenta p , the LH values of correctly identified pions and kaons are equally distributed between 0 and 1. Thus a cut at $LH > 0.01$ would be 99% efficient for each particle type.

To test that the LH distribution for correctly identified particles is really flat, the

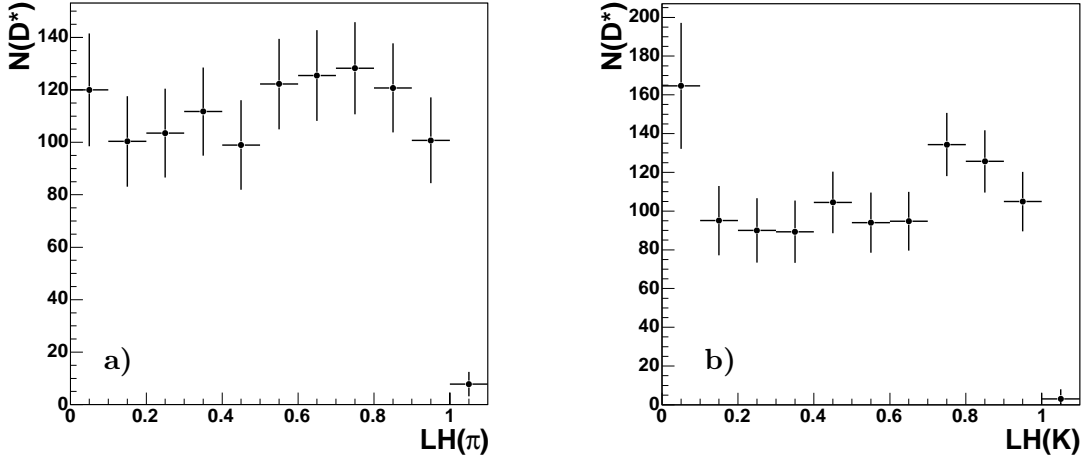


Figure 5.12: Number of D^* mesons obtained by the D^* fit in bins of the LH value for pions (a) and kaons (b). The number of D^* mesons with a pion or kaon track without a valid dE/dx measurement, represented by values above 1, can be neglected.

number of D^* mesons is determined by the D^* fit in bins of LH . The result² is shown in figure 5.12. For pions a flat distribution is achieved, which has been verified also in different ranges of the pion momentum $p(\pi)$ separately. However, for too many kaons a low LH value is determined. This indicates that eq. 3.2 is a worse approximation for kaons than for pions. Further investigations reveal that the excess of kaons with $LH < 0.1$ mainly has momenta between $0.8 < p(K) < 2.0$ GeV. The number of D^* mesons in this momentum range is determined by the D^* fit once for $0 < LH < 0.1$ and once for $0.01 < LH < 0.1$. The difference reveals that about 5% instead of only 1% of the kaons have $LH < 0.01$. To approximately compensate this effect, the LH cut is chosen to be $LH > 0.002$ for $0.8 < p(K) < 2.0$ GeV whereas it is $LH > 0.01$ for kaons with other momenta and for pions.

Thus the efficiency of both pions and kaons can be estimated to be 99% leading to $\epsilon_{dE/dx} = 0.98$. This will be applied as an overall factor. Fitting the number of D^* mesons before and after the dE/dx cuts without fixing any fit parameter gives the same result. The systematic uncertainty introduced by the determination of $\epsilon_{dE/dx}$ is assigned a value of 2%. It covers the uncertainty based on the fact that all tracks without a dE/dx measurement are accepted and that eq. 3.2 turned out to be a worse approximation for kaons than for pions.

5.6 Systematic Uncertainties

In addition to the statistical uncertainty resulting from the D^* fit, several effects exist that lead to further, systematic uncertainties of the resulting cross sections. In the following those effects will be discussed that have not yet been mentioned in the previous sections.

²To get more stable fit results, $\frac{p_t(D^*)}{S_{Et}} > 0.15$ is required.

| source | $\sigma_{sys}[\%]$ | |
|--|--------------------|--------------|
| | total | differential |
| L1 trigger | 4 | |
| L4 trigger | 4 | |
| ET33 acceptance | 6 | 3 .. 12 |
| D^* reconstruction | 11 | |
| particle identification | 2 | |
| $\mathcal{BR}(D^{*+} \rightarrow K^- \pi^+ \pi_s^+)$ | 2.5 | |
| reflections | 1.5 | |
| signal extraction | 3 | |
| model dependence | 1 | 1 .. 3 |
| luminosity \mathcal{L} | 1.5 | |
| in total | 14.5 | 13.5 .. 18 |

Table 5.5: *Relative systematic uncertainties of the total and the differential cross sections. Sources above the line have already been quantified in section 5.5.*

Table 5.5 summarises all different sources of systematic uncertainties. They are added in quadrature and result in a systematic uncertainty of 15% for the total sample and vary between 14 and 18% for the differential distributions.

D^* Branching Ratio

The D^* meson is reconstructed in the decay chain $D^{*+} \rightarrow D^0 \pi_s^+ \rightarrow K^- \pi^+ \pi_s^+$ and its charge conjugate. To achieve D^* cross sections the number of D^* mesons has to be corrected for the branching ratio of this specific decay chain. The branching ratio is measured to be $\mathcal{BR}(D^{*+} \rightarrow K^- \pi^+ \pi_s^+) = (2.57 \pm 0.06)\%$ (eq. 4.2), resulting in a relative uncertainty of 2.5%.

Reflections

Decay channels other than $D^* \rightarrow D^0 \pi_s \rightarrow K \pi \pi_s$ can contribute to the Δm signal. For example in a $D^0 \rightarrow K^+ K^-$ decay one of the kaon tracks can be wrongly identified as a pion. Despite the wrong mass assignment it is possible that the resulting D^0 mass $m(K\pi)$ fulfils the cut of ± 80 MeV around the nominal D^0 mass and the decay produces an entry in the Δm distribution. The decay modes that can wrongly contribute to the signal are summarised as *reflections*. In [1,58] their contribution to the signal has been determined to be $r = (3.5 \pm 1.5)\%$. The number of D^* mesons obtained from the fit will be corrected, the systematic uncertainty of this correction is 1.5%.

Signal Extraction

The D^* fit as described in section 4.3 assumes a single Gaussian for the signal. To estimate the uncertainty of the determination of the number of D^* mesons in data that is introduced by this assumption, the number of D^* mesons has been determined with the method described in the end of section 4.3.2, i. e. by subtracting the integral of the fitted background function from the number of entries in the signal region of the Δm distribution. The resulting number is 6% higher, to be compared with 7%

relative statistical uncertainty from the fit. In bins of η , p_t and $W_{\gamma p}$ the deviation of the number of D^* mesons determined by this subtraction method is always consistent with the statistical uncertainty, although the same tendency to higher values than from the fit can be observed.

The systematic uncertainty is taken to be 3%, i. e. half of the deviation for the total sample. No distinction is made between the total sample and the differential distributions.

Model Dependence

The L1 trigger efficiency ϵ_{L1} , the reconstruction efficiency ϵ'_{rec} and the electron tagger acceptance \mathcal{A}_{ET33} are determined from the simulation based on the PYTHIA event generator. Using the corrected CASCADE instead gives a total cross section that is smaller by 2%. The largest deviations observed in bins of η , p_t and $W_{\gamma p}$ is 6%, reached at large p_t and medium η .

The systematic uncertainty is assigned half of the deviation (in bins at least half of the deviation of the total sample), i. e. 1% for the total sample and 1% to 3% for the differential distribution.

Luminosity

The measurement of the integrated luminosity at the H1 experiment has a precision of 1.5%.

5.7 Cross Sections

The number of events N and the cross section σ of a process are related via the integrated luminosity \mathcal{L} , $N = \sigma \cdot \mathcal{L}$. To measure the cross section of a distinct process via the number of observed events, this number has to be corrected for effects like inefficiencies, acceptances and migrations. The visible cross section of D^* meson production can be calculated from $N(D^*)$, the number of D^* mesons obtained in the fit,

$$\sigma_{vis}(ep \rightarrow e' D^* X) = \frac{N(D^*) \cdot (1 - r)}{\mathcal{BR}(D^* \rightarrow K\pi\pi_s) \cdot \mathcal{L} \cdot \epsilon}. \quad (5.7)$$

Here $(1 - r)$ denotes the correction for reflections from other D^0 decays in the Δm distributions, $\mathcal{BR}(D^* \rightarrow K\pi\pi_s)$ is the branching ratio of the analysed D^* decay chain, \mathcal{L} is the integrated luminosity after correction for trigger prescales and ϵ is the product of the efficiencies of the reconstruction, triggering and the electron tagger acceptance as introduced in section 5.5.

The D^* cross section in the visible range, described in table 5.6, amounts to

$$\sigma_{vis}(ep \rightarrow e' D^* X) = (6.20 \pm 0.45 \pm 0.90) \text{ nb}. \quad (5.8)$$

The first error represents the statistical and the second the systematic uncertainty. All contributing factors are summarised in table 5.7.

In table 5.8 the result is compared with the predictions of the collinear leading order calculation supplemented with parton showers of PYTHIA, the k_t -factorisation approach in CASCADE 1.2 and collinear next-to-leading order calculations in the *massive* scheme (FMNR) and in the *massless* scheme (ZMVFNS). The predictions and their uncertainties

| Visible range | | |
|--|-----|----------------------|
| Q^2 | $<$ | 0.01 GeV^2 |
| $0.29 < y < 0.65$ | | |
| $(\Rightarrow 171 < W_{\gamma p} < 256 \text{ GeV})$ | | |
| $p_t(D^*)$ | $>$ | 2.0 GeV |
| $ \eta(D^*) $ | $<$ | 1.5 |

Table 5.6: Visible range of the D^* measurement.

| | | | | |
|-----------------|-----------------|-------------------|-------------------------|----------------------|
| $N(D^*)$ | $(1 - r)$ | \mathcal{BR} | $\mathcal{L} [pb^{-1}]$ | ϵ |
| 1154 ± 84 | 0.965 | 0.0257 | 51.1 | 0.137 |
| ϵ_{L1} | ϵ_{L4} | ϵ'_{rec} | ϵ_{dEdx} | \mathcal{A}_{ET33} |
| 0.909 | 0.969 | 0.411 | 0.980 | 0.386 |

Table 5.7: Summary of the factors contributing to the total visible cross section. The first row shows all factors mentioned in eq. 5.7. The efficiency ϵ is decomposed into the different contributions in the second row.

| $\sigma_{vis}(ep \rightarrow e'D^*X) \pm s_\sigma$ [nb] | s_σ/σ | PDF | | scales | | |
|---|----------------------------|--------------------|--------|----------|------------------|-----------|
| Data | $(6.20 \pm 0.45 \pm 0.90)$ | $\pm 16\%$ | p | γ | μ_r^2 | μ_f^2 |
| FMNR | $(5.4^{+2.1}_{-1.3})$ | $+39\%$ -24% | CTEQ5M | GRV | m_t^2 | $4m_t^2$ |
| ZMVFNS | $(9.0^{+2.8}_{-3.4})$ | $+31\%$ -38% | MRST03 | AFG04 | m_t^2 | $4m_t^2$ |
| CASCADE 1.2 | $(5.52^{+0.73}_{-0.66})$ | $+13\%$ -12% | A0 | – | $4m_c^2 + p_t^2$ | – |
| PYTHIA | 8.0 | | CTEQ5L | GRV | m_t^2 | m_t^2 |

Table 5.8: The total visible D^* cross section $\sigma_{vis}(ep \rightarrow e'D^*X)$ and their uncertainty s_σ compared with theoretical predictions. The parton densities of the proton and the photon and the chosen scales are given for the calculations which all use the charm mass $m_c = 1.5 \text{ GeV}$. The transverse mass is defined as $m_t = \sqrt{m_c^2 + p_t^2}$. For the relative uncertainties s_σ/σ the statistical and systematic uncertainties of the data are added in quadrature.

are determined as described in chapter 2. For FMNR the charm mass and the chosen factorisation and renormalisation scales have been varied independently as summarised in table 2.3. This results in an upper bound from $\mu_r/2$ and a lower bound from $\mu_f/2$ where μ_r and μ_f denote the renormalisation and factorisation scales, respectively. For ZMVFNS the scales have been simultaneously varied as described in table 2.1. For CASCADE varying the charm mass has a larger effect than varying the renormalisation scale and therefore sets the upper and lower uncertainty. No uncertainties have been determined for PYTHIA.

The FMNR and CASCADE predictions are slightly below the data, but they agree with the data within the experimental and theoretical uncertainties. The central value of the ZMVFNS prediction is far above the data. But since its uncertainty is very large – a factor two between the lower and the upper bound – it is still compatible with the data. The PYTHIA prediction is almost two standard deviation above the data.

5.7.1 Differential Cross Sections

The bin averaged differential cross section in a variable Y is calculated in analogy to eq. 5.7,

$$\frac{d\sigma_{vis}(ep \rightarrow e'D^*X)}{dY} = \frac{N(D^*) \cdot (1 - r)}{\Delta Y \cdot \mathcal{BR}(D^* \rightarrow K\pi\pi_s) \cdot \mathcal{L} \cdot \epsilon}. \quad (5.9)$$

ΔY stands for the width of the considered bin and $N(D^*)$ is the number of D^* mesons in this bin.

Figure 5.13 shows the differential cross sections $d\sigma/dp_t(D^*)$, $d\sigma/d\eta(D^*)$ and $d\sigma/dW_{\gamma p}$ in comparison with predictions from PYTHIA, CASCADE and next-to-leading order calculations in the *massive* (FMNR) and in the *massless* (ZMVFNS) scheme. The inner error bars of the data indicate the size of the statistical uncertainties from the D^* fit and the outer error bars represent the statistical and systematic uncertainties added in quadrature. The shaded and hatched areas indicate the uncertainty bands of the CASCADE, ZMVFNS and FMNR calculations. They are obtained as described in chapter 2.

The measured cross section steeply falls with increasing $p_t(D^*)$. Also the pseudorapidity distribution generally falls towards larger $\eta(D^*)$, but at $\eta(D^*) \approx 0.5$ it is slightly higher than for a continuously falling distribution. For $d\sigma/dW_{\gamma p}$ a slow decrease with increasing photon-proton centre-of-mass energies $W_{\gamma p}$ is observed. This can be understood as a convolution of the photon-proton cross section which slightly increases with increasing energies $W_{\gamma p}$, with the decreasing photon flux for increasing inelasticities $y = \sqrt{W_{\gamma p}}/s$.

For the leading order calculations the same tendencies can be observed as in the direct comparison of the number of reconstructed D^* mesons in section 5.4.2.³ In $d\sigma/dp_t$ the spectrum predicted by CASCADE is too hard. PYTHIA matches quite well apart from the lowest p_t . Here PYTHIA falls more steeply than the data. In $d\sigma/d\eta$ both predictions tend to fall too steeply towards positive η . Due to their different total visible cross sections – PYTHIA is above the data and CASCADE below – PYTHIA overestimates the backward direction (negative η) whereas CASCADE underestimates the forward direction. Without its large resolved component (dominated by charm excitation processes) the shape of the PYTHIA prediction would be even more different from the data. The shape of $d\sigma/dW_{\gamma p}$ is well reproduced by PYTHIA as well as by CASCADE.

The FMNR calculations describe the data quite well within the large theoretical uncertainties. Around $p_t(D^*) \approx 3$ GeV and for $\eta(D^*) \approx 0.5$ the data are slightly underestimated by the predictions. The central values of the ZMVFNS calculation all lie significantly above the data whereas the lower bound describes the data as well as FMNR.

The values of the FONLL calculation in figure 5.14 are those calculated for [82] and thus no values below $p_t(D^*) = 2.5$ GeV can be shown. No significant difference between the *massive* FMNR and the *matched* FONLL calculation can be seen.

5.7.2 Double Differential Cross Sections

The statistics of the data makes a more detailed look into the D^* meson distributions possible. The $p_t(D^*)$ dependence of the cross section in three different $\eta(D^*)$ bins is shown in figure 5.15. The data are compared with predictions of FMNR and PYTHIA. The predictions are compatible with the data within the uncertainties, but again it can be seen that in forward direction (figure 5.15c)) the data tend to lie above the predictions and that in PYTHIA the resolved contribution increases.

As we will see in the next chapter, requiring a jet in addition to the D^* gives more conclusive information on the charm production mechanism.

³Note that for the comparison of reconstructed quantities CASCADE 1.0 has been used instead of CASCADE 1.2 considered here.

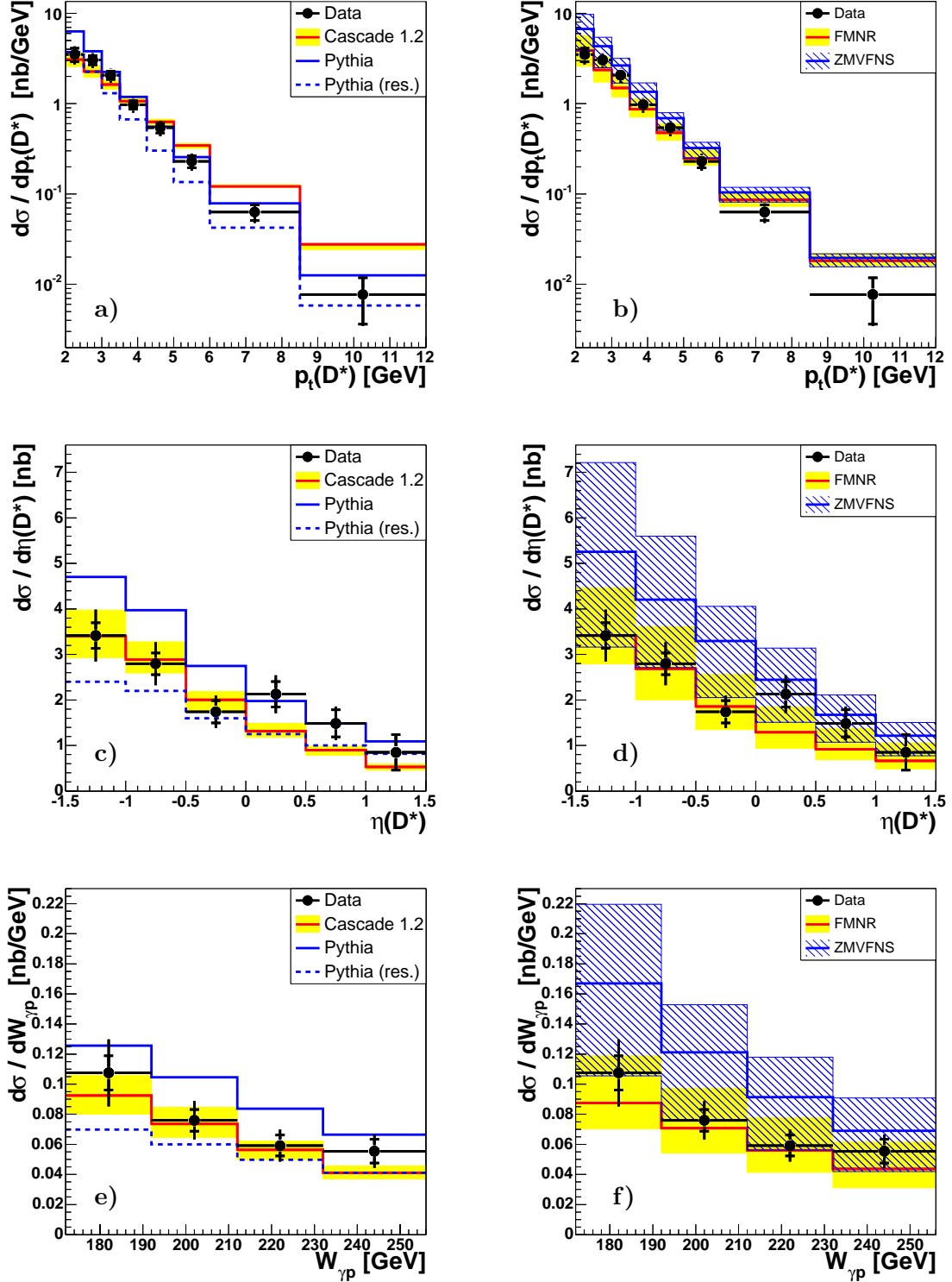


Figure 5.13: Differential D^* production cross sections in bins of $p_t(D^*)$ (a,b), $\eta(D^*)$ (c,d) and $W_{\gamma p}$ (e,f) compared with the predictions of the leading order calculations supplemented with parton shower PYTHIA and CASCADE on the left and compared with next-to-leading order calculations in the massive scheme (FMNR) and massless scheme (ZMVFNS) on the right. For PYTHIA the sum of the resolved and excitation processes of the prediction is shown separately and labelled as “res.”.

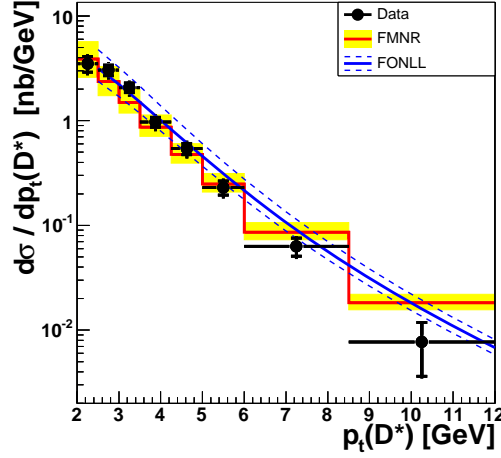


Figure 5.14: Differential D^* production cross sections in bins of $p_t(D^*)$ compared with the predictions of the massive next-to-leading order calculation FMNR and the matched calculation FONLL.

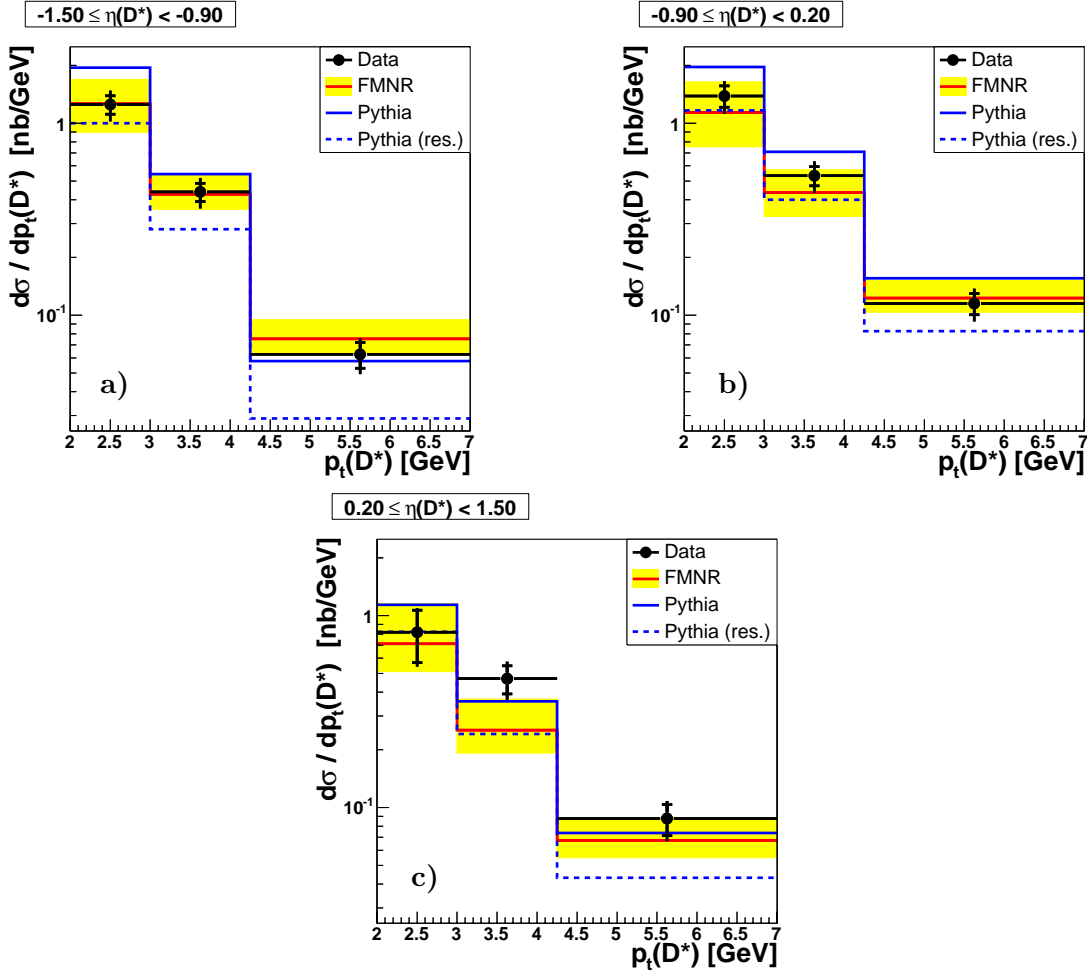


Figure 5.15: Differential D^* cross sections as a function of $p_t(D^*)$ for three bins in $\eta(D^*)$. The results are compared with the predictions of PYTHIA and the massive next-to-leading order calculation FMNR. For PYTHIA the sum of the resolved and excitation processes of the prediction is shown separately and labelled as “res.”.

Chapter 6

Measurement of D^* Mesons Associated with a Jet

In the previous chapter inclusive D^* production cross sections have been presented and compared with QCD predictions. To achieve a more detailed understanding of the charm production mechanism, it is desirable to investigate the hadronic final state. This is done by requiring a jet which does not contain D^* meson, as introduced in section 1.6.

6.1 Jet Selection

Jet Definition

Jets are defined by the inclusive k_t -algorithm [32] in the p_t -recombination and ΔR -distance scheme (cf. section 1.5). The input of the jet algorithm are the combined hadronic-final-state objects (HFS) as defined in section 3.7. The algorithm is run in the laboratory frame. Since the algorithm is invariant under longitudinal Lorentz boosts, in photoproduction the result is the same as if the algorithm would be applied in the photon-proton centre-of-mass system.

To ensure that all decay particles of the D^* candidate end up in the same jet, the HFS objects of the D^* decay tracks are replaced by the D^* candidate itself, i. e. the four-vectors that belong to the D^* decay tracks are replaced by the sum of the momenta of the tracks assigning the kaon and pion mass respectively.

In events which contain more than one D^* candidate, the jet algorithm is run separately for each candidate. For each candidate only its own decay tracks are replaced by the D^* candidate. Since most candidates are random track combinations of the background, the jet finding would be biased by random existence of the second candidate otherwise.

The minimal required transverse momentum is $p_t(\text{jet}) > 3 \text{ GeV}$. To ensure a satisfying transverse momentum measurement even at these low values of p_t , jets are restricted to the central detector region $|\eta(\text{jet})| < 1.5$ where well measured tracks dominate the HFS objects.

For hadron level jets of a Monte Carlo event generator the input of the algorithm consists of stable particles excluding the scattered positron. Also here the D^* meson replaces its decay products, i. e. D^* mesons decaying in the analysed chain are treated as stable particles.

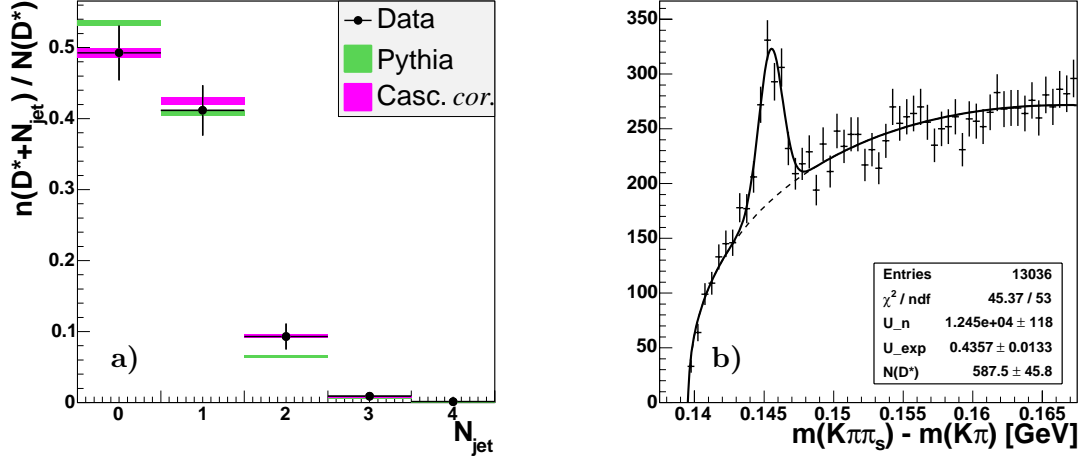


Figure 6.1: Normalised number of reconstructed jets not containing the D^* meson (a) and Δm distribution of D^* mesons associated with at least one jet (b).

| Jet Algorithm and Input | Visible Jet Range |
|---------------------------------------|---|
| inclusive k_t -algorithm | $p_t(\text{jet}) > 3.0 \text{ GeV}$ |
| p_t -weighted reconstruction scheme | $ \eta(\text{jet}) < 1.5$ |
| ΔR angular scheme | $D^* \notin \text{jet}$ |
| laboratory frame | highest- p_t jet if $N(\text{jet}) > 1$ |
| D^* replaces K, π, π_s in HFS | |
| | Reconstruction Cut |
| | $N_{daug}(\text{jet}) > 1$ |

Table 6.1: Definition and selection of the jets of the D^* +jet sample.

Selection of Jets Associated to D^* Mesons

The basis of the D^* +jet analysis is the selection of D^* candidates as described for the inclusive D^* measurement of the previous chapter.

Due to the replacement of the D^* decay particles by the D^* candidate and since the transverse momentum of the D^* candidate is at least 2 GeV, often one of the jets defined by the jet algorithm contains the D^* candidate. To investigate the production process further, the jet which contains the D^* candidate is excluded. The small amount of jets containing one particle only are excluded in data and on reconstruction level in the simulation.

Figure 6.1a) shows the multiplicity of the (non- D^* -) jets. For about 50% of the D^* mesons at least one jet is found. If more jets are found, like in about 10% of the cases, the jet with the highest transverse momentum is selected for further analysis.

Table 6.1 summarises the jet definition and selection criteria. The Δm distribution of the D^* candidates which a jet has been found for can be seen in figure 6.1b). The D^* fit gives 588 ± 46 D^* +jet combinations with a signal-to-background ratio of 0.45. The fit parameters $\mu = 0.1455 \text{ GeV}$, $\sigma = 0.8468 \text{ MeV}$ and $u_s = 20.59$ are fixed to the values

obtained from the fit of the Δm distribution of the inclusive D^* sample. If not stated otherwise, in the following all distributions will be obtained from such D^* fits in each shown bin.

6.2 Comparison of Data and Simulation

In this section the quality of the description of the data by the simulations is tested with respect to quantities related to the D^* +jet selection described above.

First the distributions of kinematical quantities of the jets and the D^* mesons associated with a jet (e. g. $\eta(\text{jet})$) are considered as well as quantities derived from those like $\eta(D^*) - \eta(\text{jet})$.

Secondly the contributions of tracks, electromagnetic or hadronic energy depositions in the calorimeters to the jet transverse momentum are compared between data and simulation.

6.2.1 D^* and Jet Quantities

To compare the simulations with the data, normalised distributions are used (cf. section 5.4.2).

The transverse momentum and the pseudorapidity distributions of the selected jets are shown in figure 6.2a-b) together with the simulations based on the PYTHIA and the modified CASCADE predictions. CASCADE has a slightly harder $p_t(\text{jet})$ spectrum than PYTHIA, but both describe the distribution of the data within the uncertainties. Also the $\eta(\text{jet})$ distribution is described well.

Figure 6.2c-d) compares the transverse momentum and the pseudorapidity distributions of D^* mesons that are associated with a jet. For the $p_t(D^*)$ distribution the observation is the same as for $p_t(D^*)$. The $\eta(D^*)$ distribution shows the same tendency as the inclusive D^* sample, i. e. low η are overestimated by the simulations and the data exceed the simulations in the medium forward region, $\eta(D^*) \approx 0.5$.

Having shown that the simulations satisfactorily describe the single D^* or jet quantities in the data within the uncertainties, the combined D^* +jet quantities are investigated: The differences in pseudorapidity $\eta(D^*) - \eta(\text{jet})$ and in azimuthal angle $\Delta\phi(D^*, \text{jet})$ between the D^* and the jet. Also investigated are the transverse momentum $p_t(D^*+\text{jet})$ and the invariant mass $m(D^*+\text{jet})$ of the D^* -jet pair and $x_\gamma(D^*+\text{jet})$.

With $x_\gamma(D^*+\text{jet})$ an approximate measure of the fraction of the photon momentum entering the hard process can be defined which has already been discussed in section 1.6.2:

$$x_\gamma(D^*+\text{jet}) = \frac{\sum_{i \in D^*} (E - p_z)_i + \sum_{j \in \text{jet}} (E - p_z)_j}{\sum_{k \in \text{HFS}} (E - p_z)_k} \quad (6.1)$$

The sums in the numerator include the decay particles of the D^* meson and the daughter particles of the jet, respectively. Thus the $E - p_z$ contribution of the jet differs from $E - p_z$ of the massless jet four-vector. If the HFS algorithm assigns a momentum to a D^* decay track that is different from the track measurement, the momentum defined by the HFS algorithm is taken. In this manner all reconstructed $x_\gamma(D^*+\text{jet})$ values are restricted to the physical range between 0 and 1.

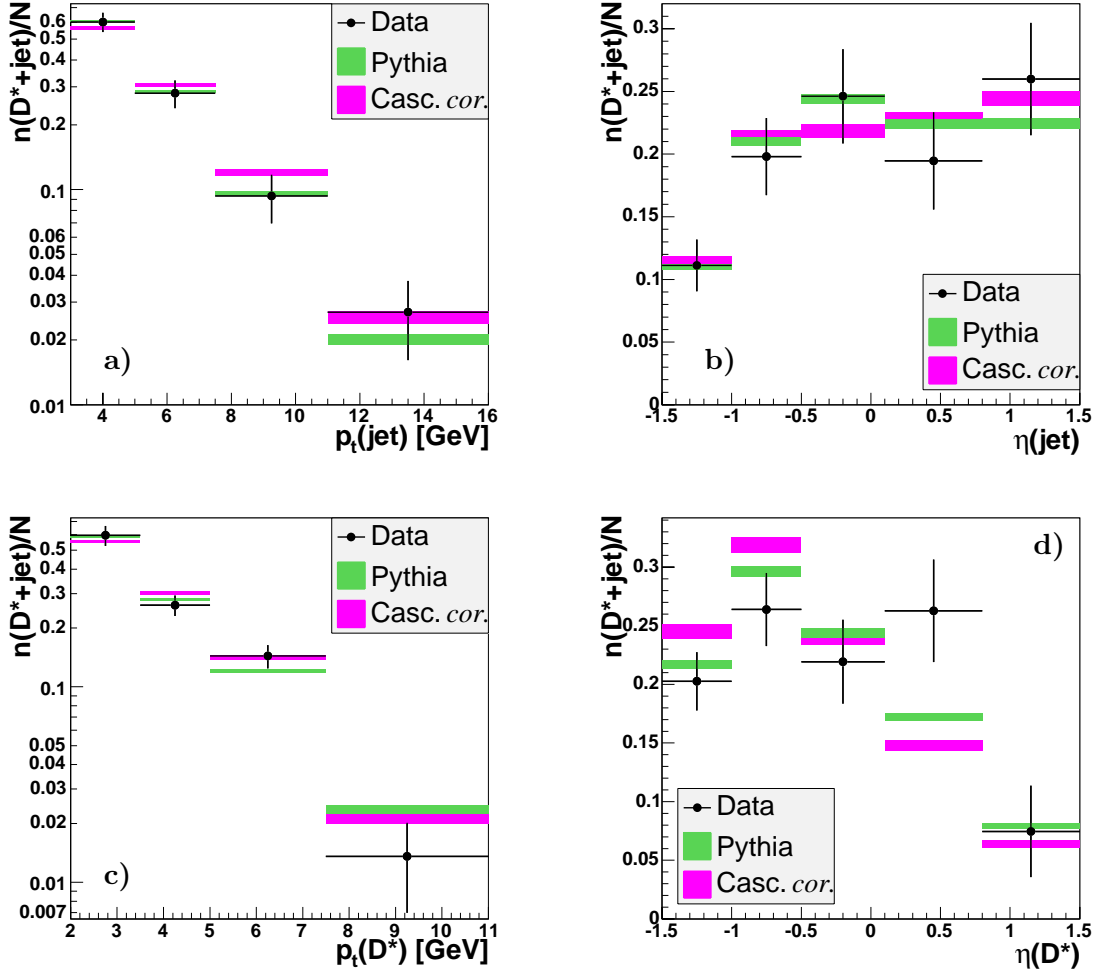


Figure 6.2: Comparison of the normalised distributions of p_t (a) and η (b) of the selected jets and of p_t (c) and η (d) of the D^* mesons associated with a jet in the data with the simulations PYTHIA and CASCADE.

Figure 6.3 compares the distributions of the combined D^*+jet quantities in the data and the simulations. The description of the data by the simulations is not as good as for the single D^* or jet kinematic quantities. Especially $x_\gamma(D^*+jet)$ rises much steeper towards its maximum at about 0.8. Here and in the other combined quantities the differences between the models PYTHIA and CASCADE are more pronounced than for the single D^* or jet quantities. But within the statistical uncertainty of the data both models describe the data.

6.2.2 Composition of the Transverse Jet Momentum

The input of the jet algorithm are the combined hadronic-final-state objects (HFS) as defined in section 3.7. The algorithm combines tracks measured in the tracking devices

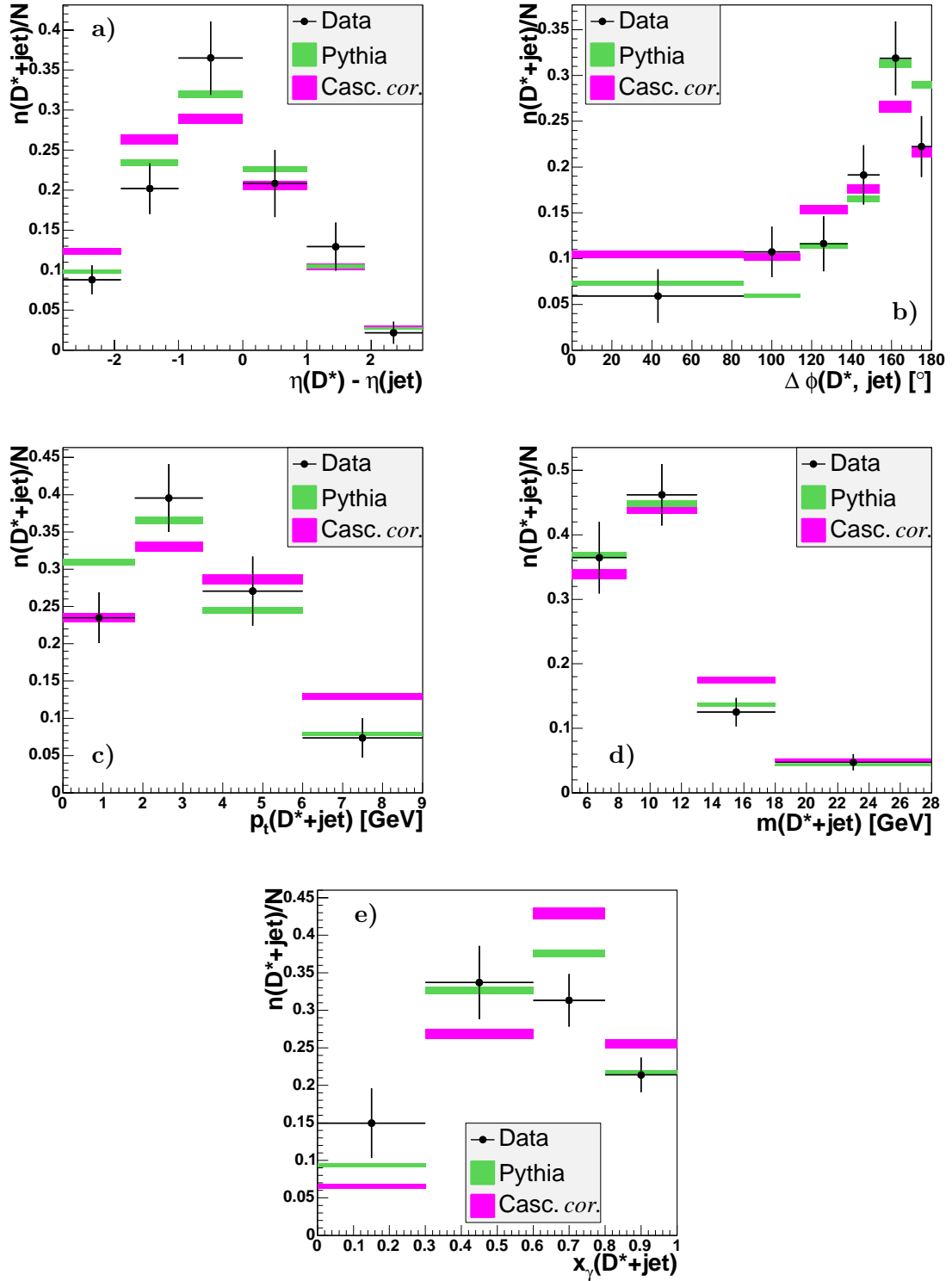


Figure 6.3: Comparison of the normalised distributions of the combined D^*+jet quantities $\eta(D^*) - \eta(jet)$ (a), $\Delta\phi(D^*, jet)$ (b), $p_t(D^*+jet)$ (c), $m(D^*+jet)$ (d) and $x_\gamma(D^*+jet)$ (e) in the data with the simulations PYTHIA and CASCADE.

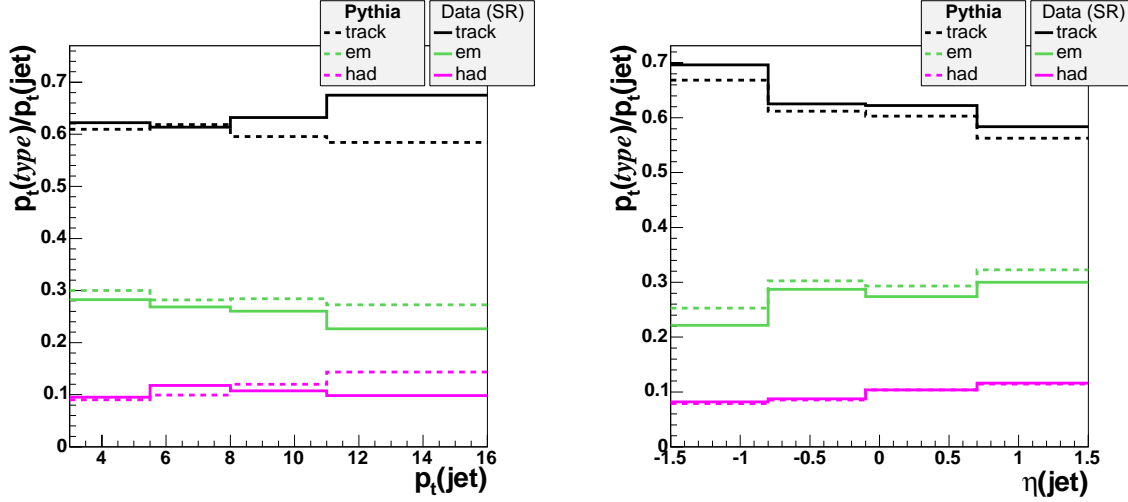


Figure 6.4: Mean transverse momentum fractions of the jets in the data and in the *PYTHIA* simulation as a function of $p_t(\text{jet})$ and $\eta(\text{jet})$: track, electromagnetic (em) and hadronic (had) measurement.

with energy depositions in the calorimeters to avoid double counting of energy. For each combined object the algorithm defines whether the four-vector is computed from the track or the calorimeter measurement. In the latter case it is also decided whether the energy deposition has to be interpreted at the electromagnetic or the hadronic energy scale. This defines three types of momentum measurement, i. e. type *track*, if the momentum is defined by the track, type *em* and type *had*, if the energy is measured in the calorimeter and interpreted as electromagnetic and hadronic, respectively.

Since the transverse momentum of a jet defined by the p_t -weighted reconstruction scheme is just the sum of the transverse momenta of its daughters (cf. eq. 1.17), one can define transverse momentum fractions of a jet,

$$\frac{p_t(\text{type})}{p_t(\text{jet})} := \frac{\sum_{\text{jet}}^{\text{type}} p_t}{p_t(\text{jet})}, \quad \text{type} = \text{track}, \text{em} \text{ or } \text{had}. \quad (6.2)$$

The sum runs over all particles inside the jet whose momentum measurement is of type *track*, *em* or *had*.

Figure 6.4 compares the mean fractions in bins of the transverse momentum and the pseudorapidity of the jets between the data and the simulation. To get better statistics in the data, no D^* fit is performed, but all jets associated to a D^* candidate in the signal region $143 < \Delta m < 148$ MeV (SR) are counted.

The track fraction dominates and reaches almost $2/3$. This indicates that charged particles are mainly reconstructed as tracks and their energy depositions in the calorimeter are ignored. In the backward direction ($\eta(\text{jet}) < -0.8$) the track fraction is larger. There the calorimetric coverage is worse than in the central and more forward region ($\eta > 0$) and neutral particles can be lost. The electromagnetic fraction is almost $1/3$ whereas the hadronic fraction plays a minor role.

The fractions are of the same size in the simulation, but the track fraction is slightly overestimated, especially at higher transverse momenta. This can be attributed to the fact that the track momentum errors are smaller in the simulation than in the data. At higher momenta the errors are relatively large and the particles of the jet enter the calorimeter closer to each other. Then it can happen that the energy depositions in the cone around the extrapolated track are compatible with the track momentum although in addition to the charged particle also a neutral particle deposited energy. In these cases the neutral particle would be lost for the HFS.

In addition to the mean transverse momentum fractions that have been considered so far the figures 6.5 and 6.6 show distributions of the transverse momentum fractions, for all jets and in bins of $p_t(\text{jet})$ (figure 6.5) and in bins of $\eta(\text{jet})$ (figure 6.6). Due to limited statistics in data, the highest $p_t(\text{jet})$ bin shown in figure 6.4 cannot be examined differentially. The simulation follows the data quite closely, besides the general trend of underestimating the track fraction.

6.3 Resolution of Jet Quantities

Since the composition of the measured jet momentum is dominated by track measurements and reasonably described by the simulation, the quality of the transverse momentum and pseudorapidity reconstruction can be investigated.

The transverse momentum resolution is defined as $(p_t^{rec} - p_t^{gen})/p_t^{gen}$. To ensure that the reconstructed and generated jet are identical, they are considered only if they are close to each other, $\Delta R = \sqrt{\eta^2 + \phi^2} < 1$. In order not to introduce a bias at low p_t^{rec} , no minimal p_t requirement is applied to the generated jets.

The result is shown in figure 6.7 in bins of the transverse momentum and the pseudorapidity of the jet. All distributions peak slightly below zero, but have a tail towards large values such that the mean value generally is above zero.

The reconstruction of the pseudorapidity $\eta(\text{jet})$ is investigated in figure 6.8. The difference between the reconstructed and the generated pseudorapidity are shown for generated and reconstructed jets that can be matched with each other within $\Delta\phi < 1$. To avoid a bias at the acceptance range in pseudorapidity, generated jets are considered in an extended region $|\eta(\text{jet})| < 2.5$. Over the entire p_t -range the distributions peak at zero and have a full width at half maximum (FWHM) around 0.2. But especially at low p_t large tails are observed. This indicates that despite of the ϕ -matching at low p_t the reconstructed jet is not identical to the generated.

In general the transverse momentum and pseudorapidity resolution are reasonably described for all considered transverse momenta and pseudorapidities.

6.4 Transverse Energy Flow Relative to the Jet

In this section the transverse energy flow relative to the jet axis is investigated to gain additional insight into D^+ +jet events. The energy flow is displayed in jet profiles. They show how energy inside and outside the jet is distributed and thus are sensitive to phenomena like multiple scattering and underlying event [83].

The profile histograms show the mean momentum of HFS objects transverse to the proton direction. The mean transverse momentum is plotted as a function of the distance

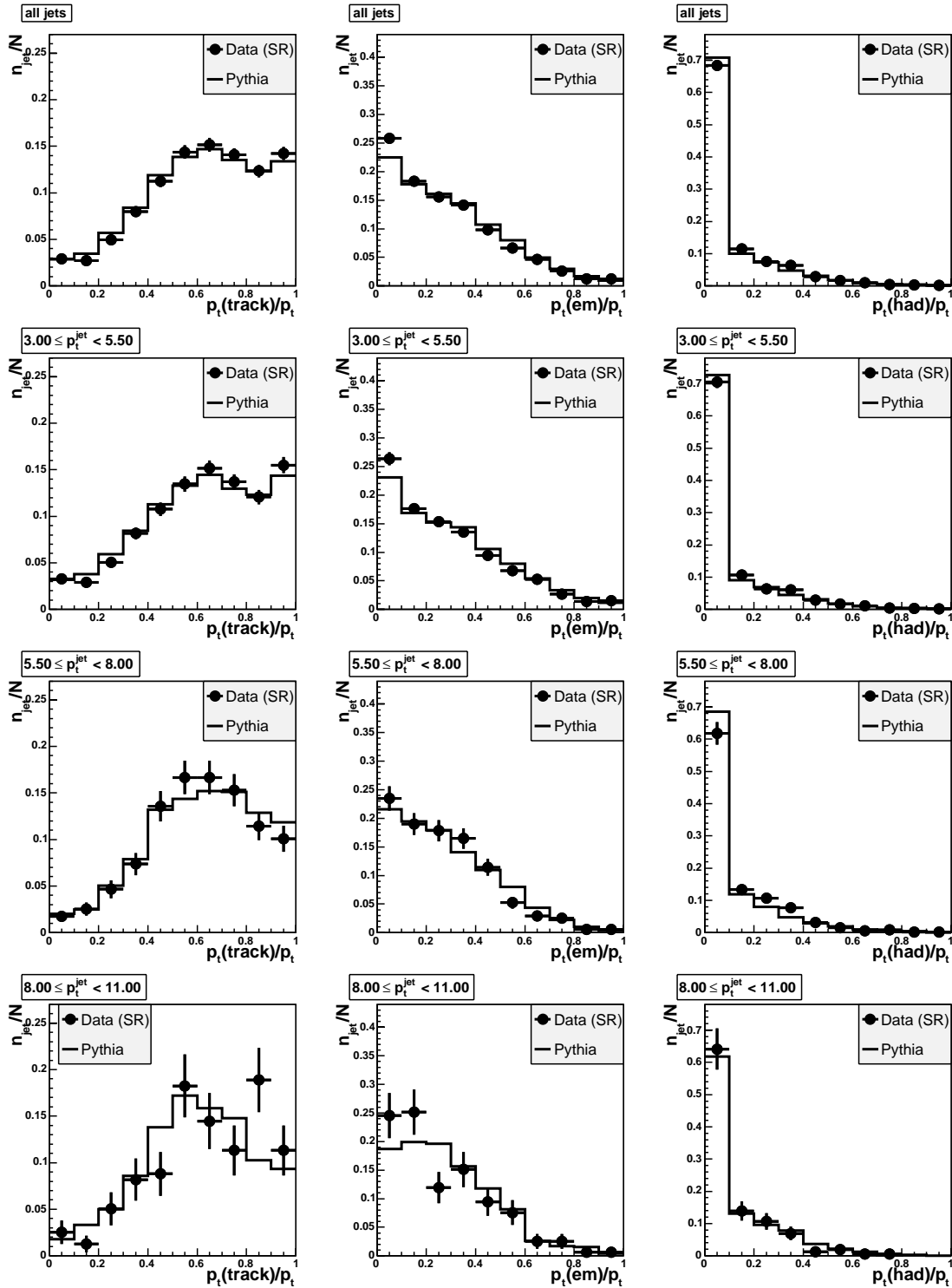


Figure 6.5: Fractions of the jet transverse momentum measurement: track fraction on the left, electromagnetic fraction in the middle and hadronic fraction on the right. The first row shows the normalised distributions for all jets whereas the other rows show different $p_t(jet)$ bins.

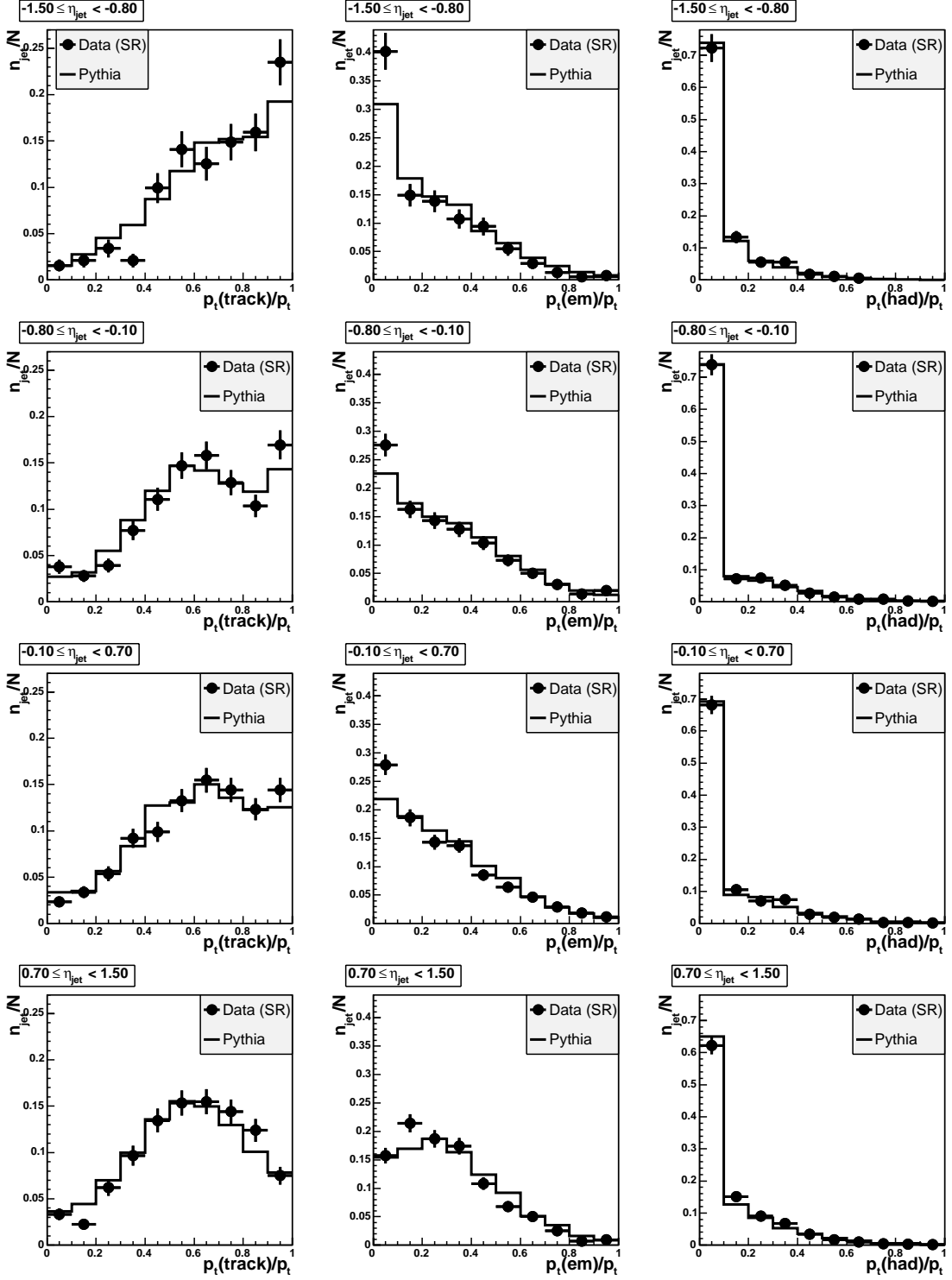


Figure 6.6: Fractions of the jet transverse momentum measurement: track fraction on the left, electromagnetic fraction in the middle and hadronic fraction on the right. Each row shows the normalised distributions for different $\eta(\text{jet})$ bins.

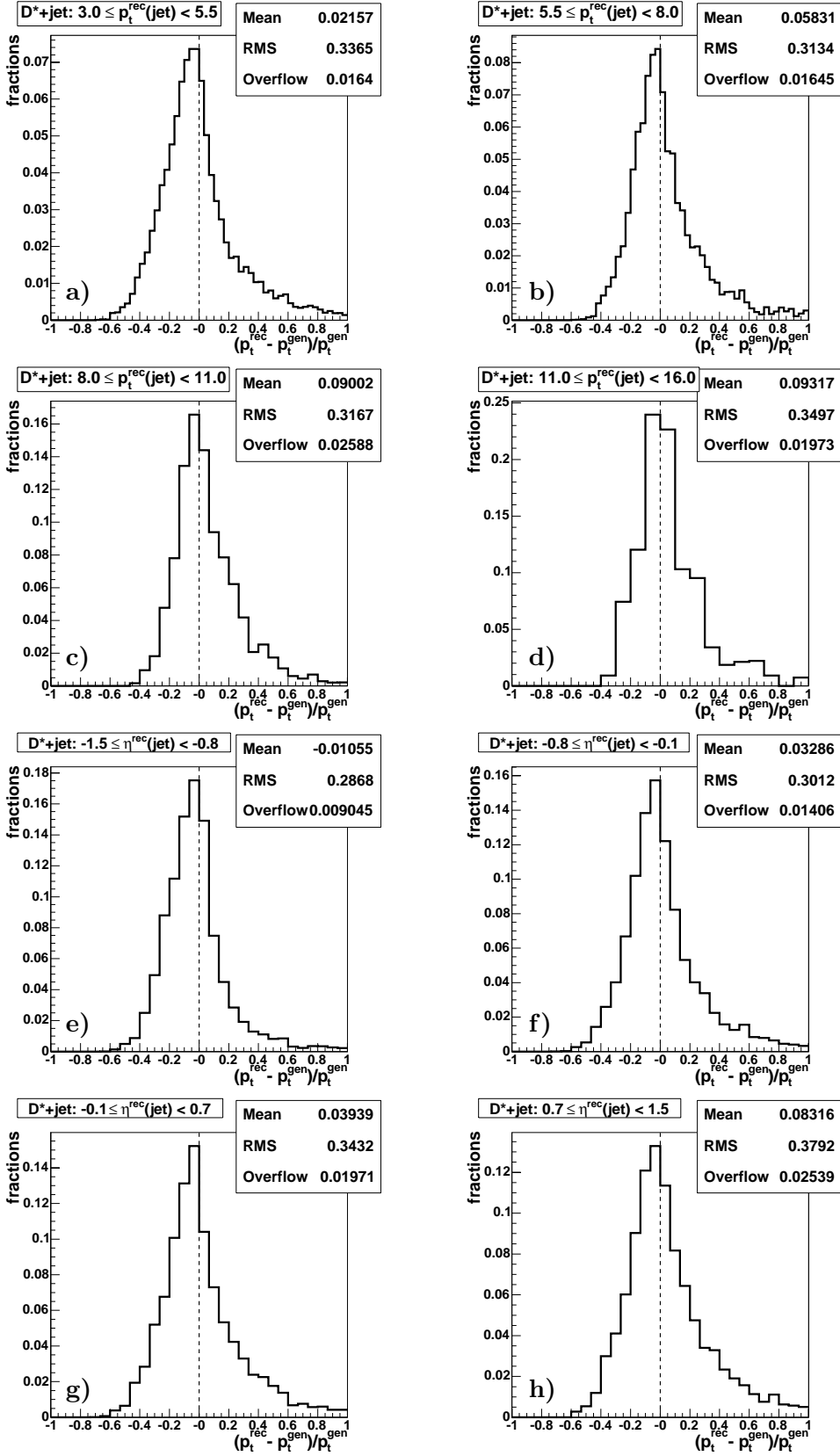


Figure 6.7: Resolution of the transverse momentum measurement of the jet in bins of $p_t^{\text{rec}}(\text{jet})$ (a-d) and $\eta^{\text{rec}}(\text{jet})$ (e-h). All distributions are normalised to one.

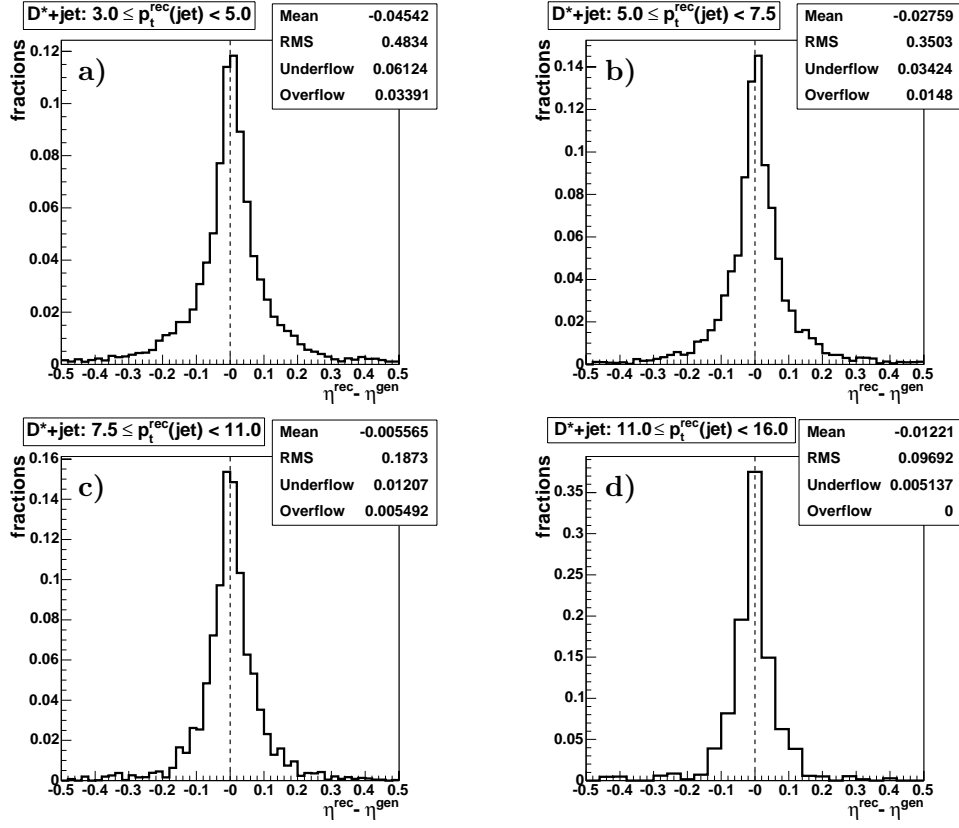


Figure 6.8: *Difference between the reconstructed and generated pseudorapidity of the jets in bins of $p_t^{\text{rec}}(\text{jet})$. All distributions are normalised to one.*

in azimuth ϕ or pseudorapidity η relative to the jet axis. Therefore the transverse momentum of HFS object i_{HFS} is filled as a weight and finally the histogram is normalised to the number of jets. To achieve profiles of the jets in $D^*+\text{jet}$ events, both the sum of weights and the normalisation result from D^* fits.

The ϕ -profile displays the transverse momentum of HFS objects at a ϕ -distance $|\Delta\phi(\text{jet}, i_{\text{HFS}})|$ from the jet. Only HFS objects close to the jet in pseudorapidity, $|\eta(\text{jet}) - \eta(i_{\text{HFS}})| < 1$, are taken into account.

In a similar way the η -profile displays the transverse momentum of HFS objects at an η -distance $\eta(i_{\text{HFS}}) - \eta(\text{jet})$ from the jet. Here only HFS objects close to the jet in ϕ , $|\Delta\phi(\text{jet}, i_{\text{HFS}})| < 1$, are taken into account. Thus particles from any other jet balancing the transverse momentum are excluded.

In figure 6.9 the jet profiles for all selected jets are shown¹ and compared with the simulations. The peaks close to zero originate from the particles of the jet itself. They are well described by the simulations.

The η -profile shows that both simulations lie above the data for energy flow more forward than the jet, $\eta(i_{\text{HFS}}) - \eta(\text{jet}) > 0$. The ϕ -profile exhibits a second peak close to π .

¹To get more stable fit results in the data, the background exponent u_e is fixed for all profiles in data. In the simulations all D^* candidates in the signal region are counted.

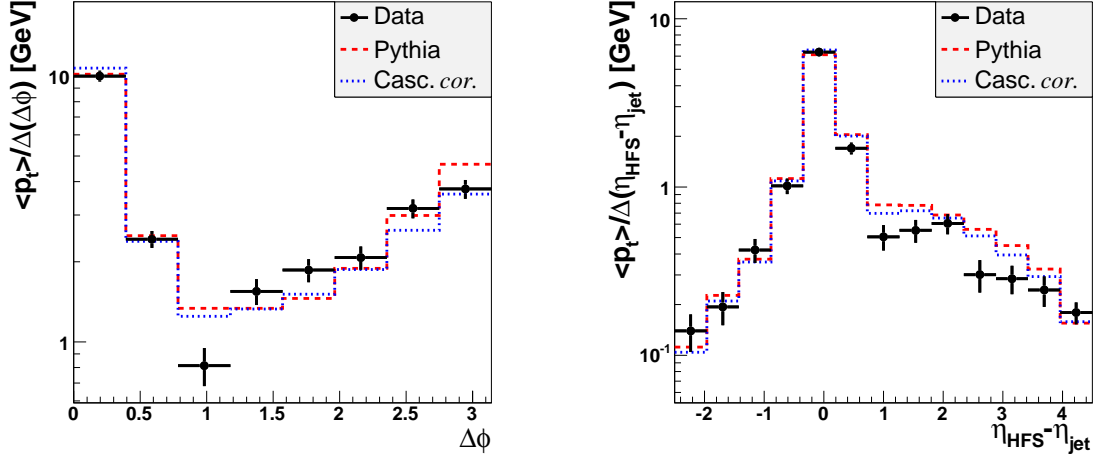


Figure 6.9: Jet profiles in ϕ and η . The error bars denote the statistical error from the D^* fit.

It can be attributed to the D^* -jets which are opposite in ϕ to the selected jets.

The behaviour of the energy flow in ϕ with respect to the jet axis is investigated in bins of $p_t(\text{jet})$ and $\eta(\text{jet})$ in figure 6.10. The two-peak structure becomes clearer with increasing transverse momentum $p_t(\text{jet})$ (figures 6.10a-c). Figures 6.10d-h) show the profiles for different $\eta(\text{jet})$. They reveal that in the forward direction ($\eta(\text{jet}) > 0$) the second peak becomes smaller and almost vanishes, which means that the D^* -jet is further away in η than $|\eta(\text{jet}) - \eta(i_{\text{HFS}})| < 1$.

In general the energy flow shown in the ϕ profiles is reasonably described by the simulations, even the pedestal between the peaks². But at higher $p_t(\text{jet})$ the data show more energy in the second peak at π . At $\eta(\text{jet}) \approx 0.5$ the second peak is less clear than the simulations predict. This is the same η -region where also the number of D^* mesons in the data exceeds those observed in the simulations whereas the number of jets is slightly below the simulations (cf. figures 6.2b+d). Comparing PYTHIA and CASCADE reveals that the second peak is always more dominant in PYTHIA than in CASCADE. But the statistical precision of the data is too limited to distinguish between the models.

6.5 Correction Factors, Purities and Stabilities

To extract cross sections for the D^* +jet sample, the efficiency correction $\epsilon = \epsilon_{L1} \cdot \epsilon_{L4} \cdot \epsilon'_{rec} \cdot \epsilon_{\text{dEdx}} \cdot \mathcal{A}_{\text{ET33}}$ (eq. 5.4) has to be determined. This is done in analogy to the determination of the correction factors for the inclusive D^* sample, described in section 5.5. The results will be shown in this section.

The resolution of the transverse momentum measurement of the jet (section 6.3) is worse than for the D^* meson. Especially at low $p_t(\text{jet})$ it is possible that the selected jet measured at detector level is not identical to the one generated, i. e. they have different

²The low values around $\Delta\phi = 1$ in the data may be influenced by the low signal-to-background ratios of the D^* fits in these bins.

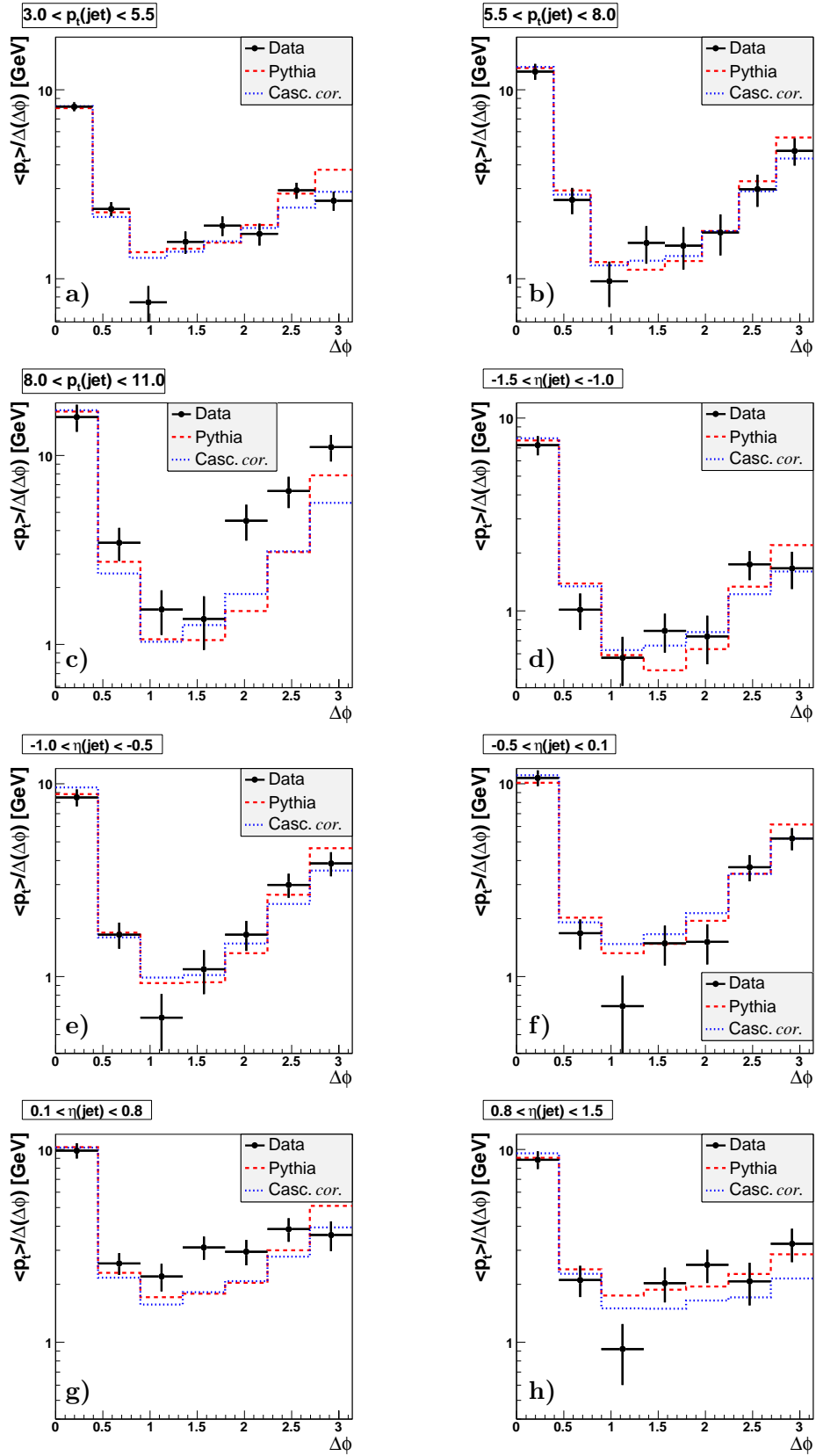


Figure 6.10: Jet profiles in ϕ for different $p_t(\text{jet})$ (a-c) and $\eta(\text{jet})$ (d-h). The error bars denote the statistical error from the D^* fit.

directions. To quantify the amount of migrations and to demonstrate that an efficiency correction based on the definition of ϵ'_{rec} in eq. 5.6 is still possible, the purity P and the stability S are presented together with the efficiencies. They are defined as

$$P = \frac{N_{gen}^{rec}}{N_{bin}^{rec}}, \quad (6.3)$$

$$S = \frac{N_{gen}^{rec}}{N_{bin}^{gen}}. \quad (6.4)$$

P and S are calculated under the condition that both a generated D^* meson and a reconstructed D^* candidate are found within the visible range of the inclusive D^* measurement (cf. table 5.6). The reconstructed candidate must lie in the signal region $143 < \Delta m < 148$ MeV and have the same charge as the generated D^* meson. Under these conditions

N_{gen} is the number of generated D^* +jet combinations in a bin,

N_{bin}^{rec} is the number of reconstructed D^* meson candidates associated with a reconstructed jet in a bin and

N_{bin}^{gen} is the number of reconstructed D^* +jet combinations in a bin with a generated D^* +jet combination in the same bin.

In the following the purity P , the stability S and the efficiencies ϵ_{L1} and ϵ'_{rec} are presented first for the total D^* +jet sample, then in bins of the measured jet and D^* quantities and finally in bins of the combined D^* +jet quantities.

6.5.1 Total D^* +Jet Sample

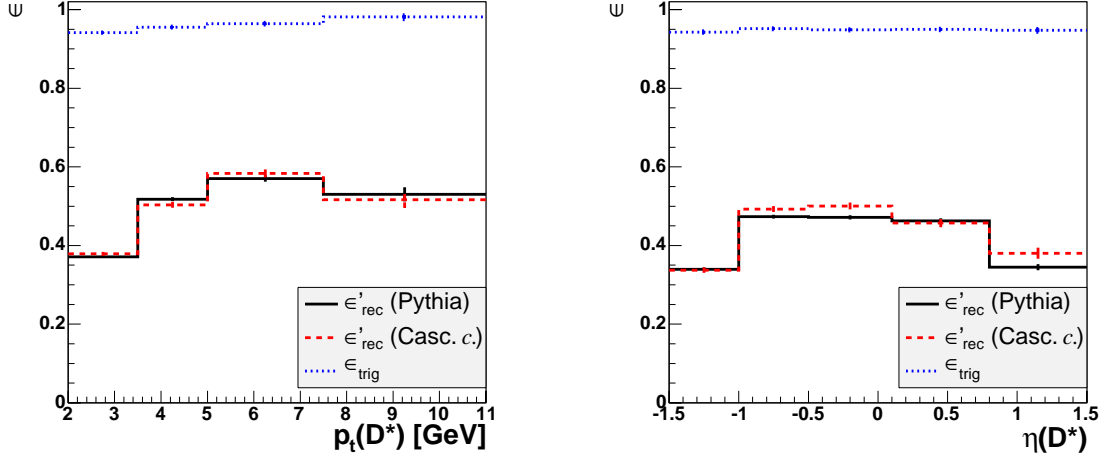
The overall factors $\epsilon_{L1} = 0.969$ and $\epsilon_{dEdx} = 0.98$ are taken as determined for the inclusive D^* sample.

The electron tagger acceptance of the D^* +jet sample has been determined to $\mathcal{A}_{ET33} = 39.2\%$ and shows only very small variations for the D^* +jet quantities considered. This value is a little higher than for the inclusive D^* sample, indicating a slightly different inelasticity distribution.

The L1 trigger efficiency of the D^* +jet sample is $\epsilon_{L1}(D^*+jet) = 94.8\%$, to be compared with $\epsilon_{L1}(D^*) = 90.9\%$ for the inclusive sample, the reconstruction efficiency amounts to $\epsilon'_{rec}(D^*+jet) = 42.0\%$, determined with the PYTHIA simulation. Using CASCADE results in $\epsilon'_{rec}(D^*+jet) = 42.7\%$ if modified according to $p_t(D^*)$ and $\epsilon'_{rec}(D^*+jet) = 44.2\%$ without this correction.

The trigger and reconstruction efficiencies are expected to be slightly higher than for the inclusive D^* sample: Requiring a jet in addition to the D^* meson selects a subset of the D^* events with higher transverse momenta on average. Higher transverse momenta give a higher efficiency for the DCRPh trigger. In addition the $p_t(jet) > 3$ GeV requirement selects D^* mesons with higher average transverse momenta balancing $p_t(jet)$. Higher average $p_t(D^*)$ leads to a higher reconstruction efficiency.

The purity and stability of finding a jet in events with a D^* meson are $P = 86\%$ and $S = 81\%$ for PYTHIA and $P = 89\%$ and $S = 83\%$ for CASCADE. This means that almost 90% of the D^* candidates that are associated with a reconstructed jet also have a jet on the generator level and that more than 80% of the generated D^* +jet pairs are

Figure 6.11: *Efficiencies of D^* mesons associated with a jet.*

also reconstructed. The slightly higher values for CASCADE can be related to the flatter $p_t(\text{jet})$ spectrum resulting in smaller migration losses due to the $p_t(\text{jet})$ cut.

6.5.2 Single D^* and Jet Quantities

The L1 trigger and the reconstruction efficiencies of D^* +jet combinations are shown in figure 6.11 as functions of $p_t(D^*)$ and $\eta(D^*)$. They follow the same trend as the inclusive D^* sample, presented in sections 5.5.1 and 5.5.4. The trigger efficiency is nearly constant, rising slightly with increasing p_t . The reconstruction efficiency rises with increasing p_t , but drops again for the highest p_t . At larger $|\eta(D^*)|$ it is lower than in the central region.

The figures 6.12a-d) show the efficiencies in bins of $p_t(\text{jet})$ and $\eta(\text{jet})$. The dependence on $p_t(\text{jet})$ is similar to that on $p_t(D^*)$, but less prominent since the transverse momentum of the jet and of the D^* are correlated due to the p_t -balance between the jet and the D^* .

Figures 6.12b-c) show the purities and stabilities in bins of $p_t(\text{jet})$. These bins are chosen such that the purity is of the same size for all bins. This is achieved by increasing the bin width with increasing $p_t(\text{jet})$: The relative resolutions (figure 6.7) stay almost constant with p_t , which means that the absolute resolutions increase with p_t . The purities and stabilities as a function of $\eta(\text{jet})$ are shown in figure 6.12e-f). Since there are relatively few jets found for $\eta < 0$ compared to $\eta > 0$ (cf. figure 6.2b)), there are fewer possibilities to reconstruct erroneously a jet in backward direction, leading to larger purity and lower stability in the backward direction.

Purity P and stability S are generally at least $P = 60\%$ and $S = 50\%$.

6.5.3 Combined D^* +Jet Quantities

The efficiencies, purities and stabilities of the combined D^* +jet variables are shown in figure 6.13. They are generally lower than those of the single jet measurement since migration effects are more prominent when combining several measured quantities like momenta and angles of the D^* and the jet. The purities and stabilities are relatively

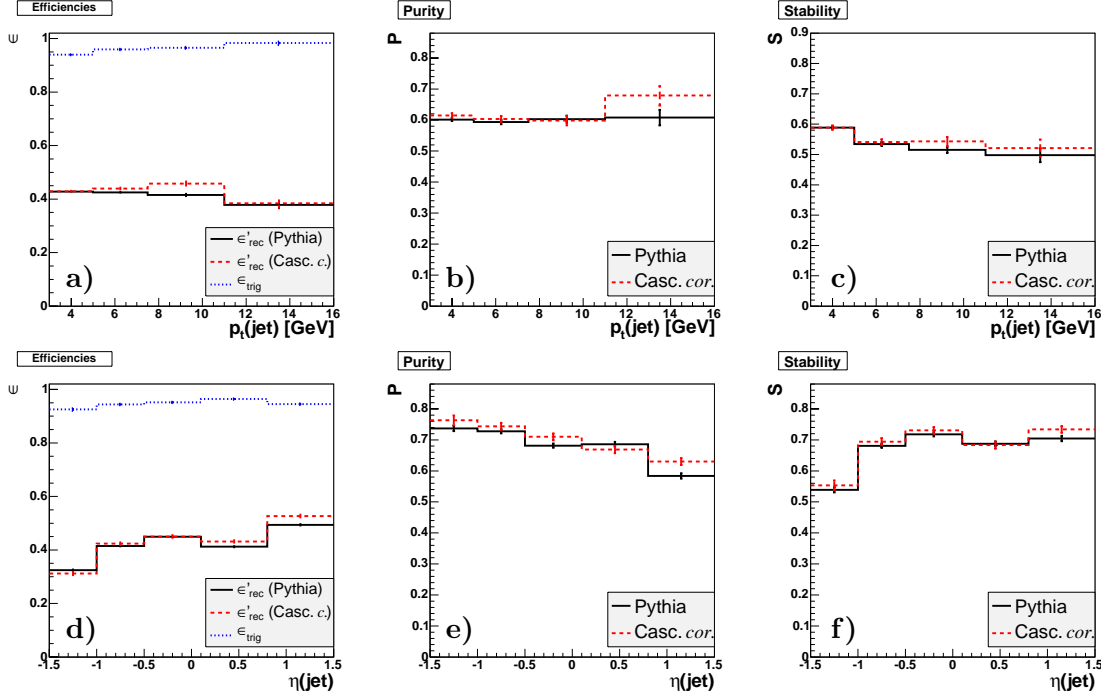


Figure 6.12: Efficiencies (a+d), purity (b+e) and stability (c+f) in bins of the transverse momentum and the pseudorapidity of the jets.

high for $\eta(D^*) - \eta(\text{jet})$. For $\Delta\phi(D^*, \text{jet})$ they are at the 60% level for CASCADE, but significantly lower for PYTHIA, especially for small $\Delta\phi(D^*, \text{jet})$. Since there are only few $D^* + \text{jet}$ pairs with small $\Delta\phi(D^*, \text{jet})$, “wrong” jets, i.e. different jet directions on reconstruction and generator level, deteriorate the purity. In $x_\gamma(D^* + \text{jet})$ the bins are chosen such that the purity is 60%. In bins of $p_t(D^* + \text{jet})$ purity and stability are around 50% only, but for $m(D^* + \text{jet})$ they are higher again, around 60%.

Generally the purities and stabilities of the combined $D^* + \text{jet}$ quantities are above 50% with exceptions in $\Delta\phi(D^*, \text{jet})$ and $p_t(D^* + \text{jet})$ where they are still above 40%. This guarantees a sufficient correlation between the generated and reconstructed quantities making the application of the efficiency correction possible.

6.6 Systematic Uncertainties

The sources of systematic uncertainties in the $D^* + \text{jet}$ cross section analysis are mostly the same as for the inclusive D^* analysis. Therefore they do not have to be estimated separately, but can be adopted from the inclusive analysis, section 5.6. This is the case for the L1 and L4 trigger efficiencies (both 4% uncertainty), the electron tagger acceptance (6%), the reconstruction efficiency (11%), the efficiency of the particle identification (2%), the branching ratio $\mathcal{BR}(D^{*+} \rightarrow K^- \pi^+ \pi_s^+)$ (2.5%), the reflection correction (1.5%) and the luminosity determination (1.5%).

To determine the systematic uncertainty of the signal extraction the procedure described in section 5.6 has been applied. Again no large deviations above the statistical

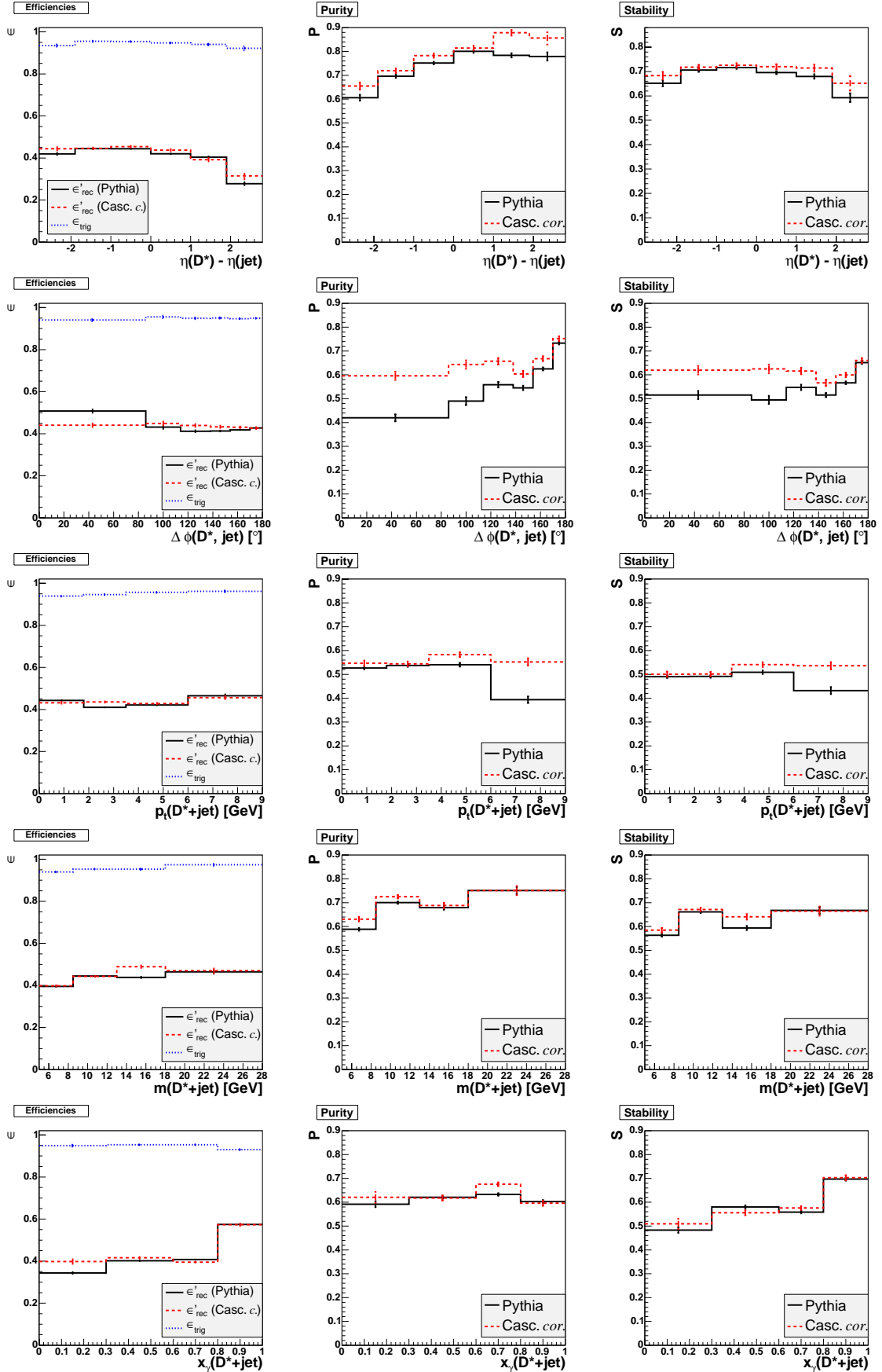


Figure 6.13: Efficiencies, purities and stabilities of the combined D^*+jet quantities $\eta(D^*) - \eta(jet)$, $\Delta\phi(D^*, jet)$, $p_t(D^*+jet)$, $m(D^*+jet)$ and $x_\gamma(D^*+jet)$.

uncertainty are observed. Thus the uncertainty is estimated to 3%, the same as for the inclusive sample.

Also the uncertainty introduced by the model dependence of the efficiency determination is estimated in the same way as for the inclusive D^* sample (cf. section 5.6), i. e. using the corrected CASCADE instead of PYTHIA for the determination of ϵ_{L1} , ϵ'_{rec} and \mathcal{A}_{ET33} and assigning the uncertainty half of the deviation. The result is 1% for the total D^* +jet sample and varies between 1% and 9% for the differential distributions. Values above 6% are reached only for the lowest $x_\gamma(D^*$ +jet), the lowest $\Delta\phi(D^*$,jet) and the largest $\eta(D^*)-\eta(\text{jet})$ bins.

The jet measurement has an additional uncertainty due to the uncertainty of the absolute energy scale of the calorimeters and the calorimeter simulation since they are used for constructing the HFS objects. As a first estimate of the influence of this uncertainty on the result, the energy measurement on the hadronic and electromagnetic reconstruction levels have been varied, by $\pm 4\%$ and $\pm 2\%$ in the LAr calorimeter and by $\pm 8\%$ and $\pm 1\%$ in the SpaCal, respectively. The hadronic and electromagnetic energy scales of the calorimeters are known to about that precision. The resulting cross section changes are smaller than the statistical uncertainty and thus cannot be used to quantify the influence of the energy scale uncertainty on the cross sections.

Therefore the uncertainty is estimated by the following consideration: On average 30% of the jet transverse momentum measurement is taken from the electromagnetic energy scale, 10% from hadronic scale and the rest is determined from tracks (cf. section 6.2.2). Multiplying these fractions with the scale uncertainties of the LAr leads to an average uncertainty of 1%. The SpaCal can be neglected. This consideration ignores that the track fraction depends on the energy measurements in the calorimeters. Thus the systematic uncertainty introduced by the uncertainty of the calorimeter energy scale is conservatively estimated to be 1.5%.

Adding all systematic uncertainties quadratically results in a systematic uncertainty of 14.7% for the total D^* +jet sample and varies from 14.7% to 17.2% for the differential distributions.

6.7 Hadronisation Corrections

Before comparing the next-to-leading order (NLO) QCD calculations as described in section 2.3 to the D^* +jet measurements, the calculations have to be corrected for hadronisation effects, i. e. the influence of the transition from partons to observable mesons on the result of the jet algorithm.

The hadronisation corrections will be determined as bin-by-bin corrections from hadron level calculations supplemented by parton showers, PYTHIA and CASCADE. The procedure is similar to the determination of the efficiencies. The hadronisation correction factor is defined as

$$C_{had} = \frac{N^{gen}(D^*$$
+jet)}{N^{ps}(D^*+jet)} \Big|_{vis}. \quad (6.5)

Here $N^{ps}(D^*$ +jet) is the number of D^* +jet pairs after the parton shower, but before the hadronisation, and $N^{gen}(D^*$ +jet) is the number after the hadronisation, both in the visible range (table 6.2) and for differential efficiencies in the corresponding bin. This procedure

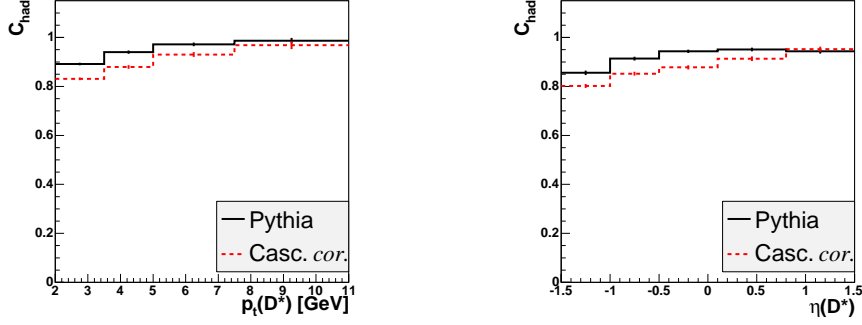


Figure 6.14: *Hadronisation correction in bins of $p_t(D^*)$ and $\eta(D^*)$.*

is an approximation since it assumes that the parton level of PYTHIA and CASCADE is similar to that of the NLO calculations.

To determine $N^{ps}(D^*+\text{jet})$ the jet algorithm is applied to all partons before the hadronisation. These can be identified since their “daughter particles” are labelled as “strings” or “clusters”. Since the D^* fragmentation is already taken care of in the NLO calculation, even for $N^{ps}(D^*+\text{jet})$ the D^* meson is considered instead of the charm quark before the fragmentation. The D^* -jet is identified as the jet which contains the charm quark which fragmented into the considered D^* meson.

The charm excitation process in PYTHIA is calculated with massless charm quarks, including a massless treatment of the charm quark in the simulation of parton radiation in the parton shower. This leads to events where the charm quark after the parton shower is highly virtual with energies which may even be far below the nominal charm mass of $m_c = 1.5$ GeV. As a consequence the direction of the charmed hadron after the hadronisation is hardly correlated with the charm quark. This behaviour is considered as unphysical and events where the charm energy is below its mass are not taken into account for the calculation of the hadronisation correction.

The resulting hadronisation corrections are $C_{had} = 0.89$ for PYTHIA and $C_{had} = 0.86$ CASCADE. Figure 6.14 shows the hadronisation corrections in bins of $p_t(D^*)$ and $\eta(D^*)$. The largest deviations from one are found for low transverse momenta. Since negative pseudorapidities are dominated by low transverse momenta, also there C_{had} is lower than one. The difference between PYTHIA and CASCADE is also largest for low momenta and negative pseudorapidities.

Since both PYTHIA and CASCADE use the same hadronisation model, the difference must be due to differences in the parton state. Like for the correction of the detector effects by the efficiencies, the results from PYTHIA will be used. They are generally closer to one. Nevertheless, for comparison the CASCADE results will also be shown in the following differential distributions.

Purity and stability of the total sample, calculated in analogy to eq. 6.3 and 6.4, amount to $P_{had} = 85\%$ and $S_{had} = 76\%$ for PYTHIA and $P_{had} = 89\%$ and $S_{had} = 76\%$ for CASCADE, respectively. The stability S_{had} being lower than the purity P_{had} is consistent with C_{had} being below one since it indicates that more often $D^*+\text{jet}$ combinations migrate out of the visible range than migrate into the visible range.

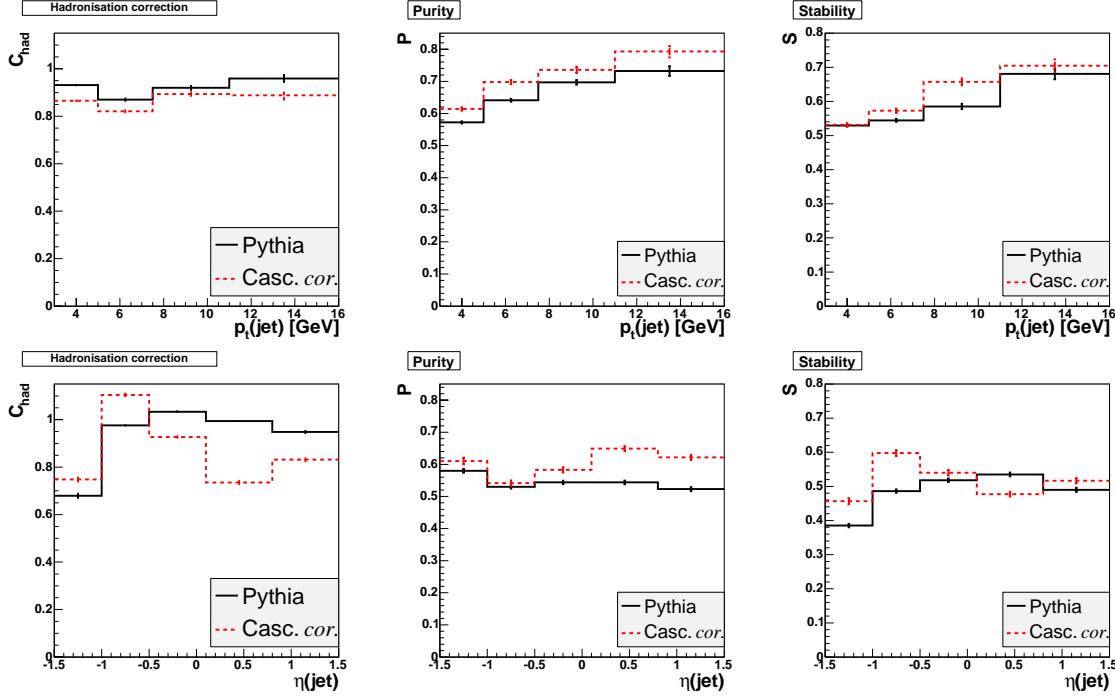


Figure 6.15: Hadronisation correction in bins of $p_t(\text{jet})$ and $\eta(\text{jet})$ and the corresponding purities and stabilities.

In figure 6.15 the hadronisation corrections and the corresponding purities and stabilities are shown for the bins in $p_t(\text{jet})$ and $\eta(\text{jet})$. Apart from low $\eta(\text{jet})$ C_{had} is quite stable. The purities and stabilities are above 50% except for the most negative pseudorapidities. They both increase with the transverse momentum, which is related to the increasing bin widths.

The hadronisation corrections, purities and stabilities for the combined D^* +jet quantities are shown in figure 6.16. For $\eta(D^*) - \eta(\text{jet})$, $p_t(D^*+\text{jet})$ and $m(D^*+\text{jet})$ the situation is similar to the jet-only quantities, although purities and stabilities are slightly lower. In $\Delta\phi(D^*,\text{jet})$ the purities and stabilities differ significantly between PYTHIA and CASCADE, but the correction is of similar size and is large only for very low $\Delta\phi(D^*,\text{jet})$. The two last bins used in the measurement are combined because the NLO calculations cannot provide smaller bins in this infrared sensitive region as discussed in section 2.3. In $x_\gamma(D^*+\text{jet})$ the corrections are up to 40%, but the purities and stabilities are not smaller than for the other quantities: The fragmentation leads to migrations towards lower values of $x_\gamma(D^*+\text{jet})$ only.

The purities and stabilities of the hadronisation corrections are slightly lower than those of the efficiency corrections (section 6.5). But they are all at least almost 40%. Only the first bin in $\Delta\phi(D^*,\text{jet})$ has a lower stability, a bin where also the statistical uncertainty of the data is very large.

The hadronisation corrections obtained from PYTHIA will be applied to the next-to-leading order calculations before the comparison with the data in the next section.

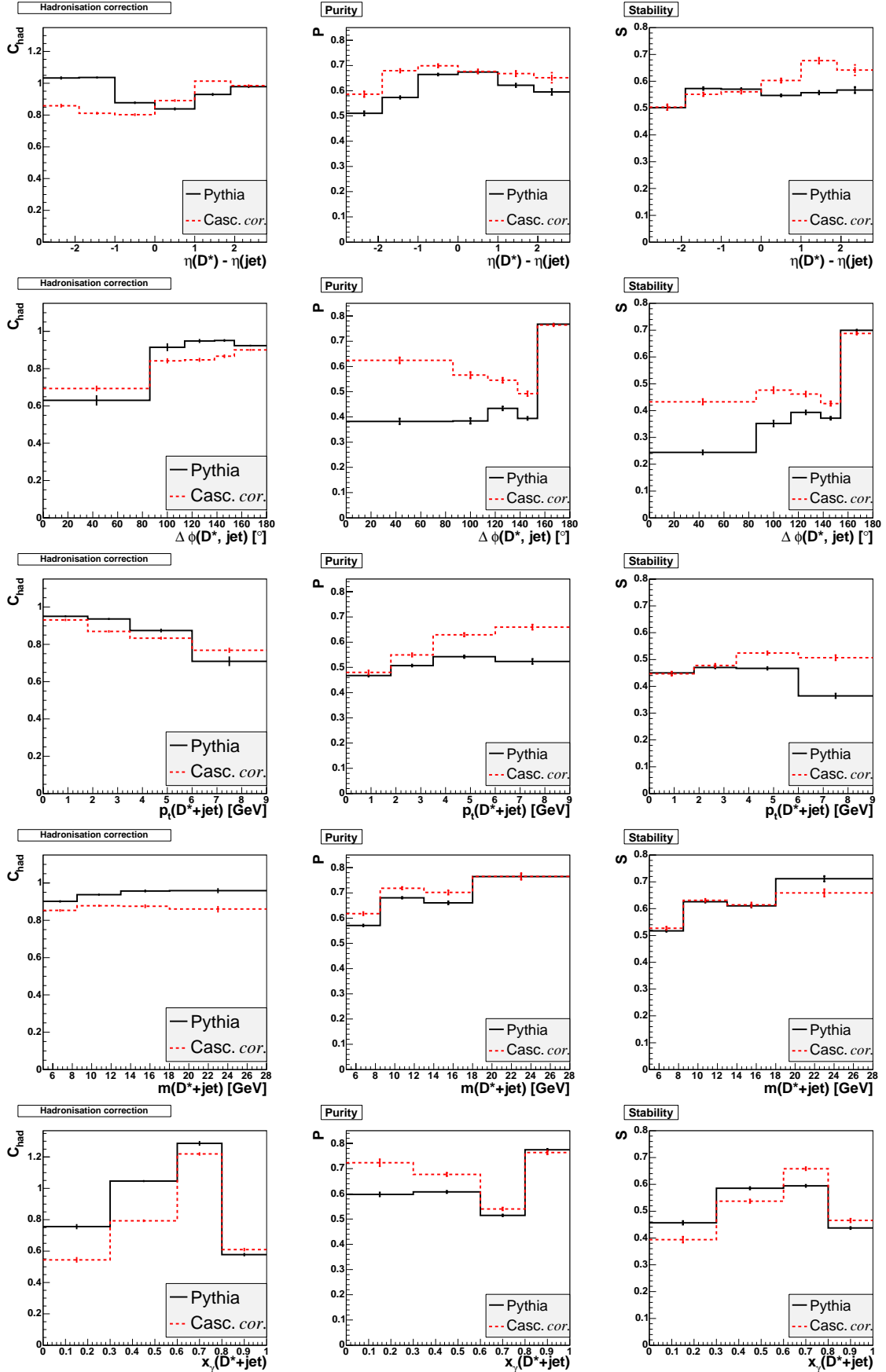


Figure 6.16: Hadronisation corrections, purities and stabilities in bins of the combined D^*+jet quantities $\eta(D^*) - \eta(jet)$, $\Delta\phi(D^*, jet)$, $p_t(D^*+jet)$, $m(D^*+jet)$ and $x_\gamma(D^*+jet)$.

| <i>Visible range: D^*+jet</i> | | |
|---|----------|-----------------------|
| Q^2 | < | 0.01 GeV ² |
| $0.29 < y < 0.65$ | | |
| ($\Rightarrow 171 < W_{\gamma p} < 256$ GeV) | | |
| $p_t(D^*)$ | > | 2.0 GeV |
| $ \eta(D^*) $ | < | 1.5 |
| $p_t(\text{jet})$ | > | 3.0 GeV |
| $ \eta(\text{jet}) $ | < | 1.5 |
| D^* | \notin | jet |
| jet with highest p_t | | |

Table 6.2: *Visible range of the D^* +jet measurement.*

6.8 Cross Sections

This section presents the cross sections of the D^* +jet sample and compares them with the QCD predictions, first the total visible D^* +jet cross section, followed by bin averaged differential cross sections as a function of the transverse momentum and the pseudorapidity of the D^* and the jet as well as combined D^* +jet quantities. The visible range is summarised in table 6.2.

To calculate the cross sections, eq. 5.7 and 5.9 are applied, respectively, now using the number of D^* +jet pairs $N(D^*$ +jet). The result of the total visible D^* +jet cross section is

$$\sigma_{vis}(ep \rightarrow e'D^* \text{ jet } X) = (2.96 \pm 0.23 \pm 0.43) \text{ nb.} \quad (6.6)$$

The first uncertainty denotes the statistical uncertainty of the D^* fit³ and the second the systematical uncertainty. The ratio of this D^* +jet to the inclusive D^* cross section amounts to $\sigma(D^*$ +jet)/ $\sigma(D^*) = 47.7\%$.

In table 6.3 the result is compared with the predictions of the collinear leading order calculation from PYTHIA, the k_t -factorisation calculation with CASCADE 1.2 and collinear next-to-leading order calculations in the *massive* scheme (FMNR) and in the *massless* scheme (ZMVFNS), cf. chapter 2. The results of the NLO calculations are stated before and after applying the hadronisation correction determined in section 6.7. The positive and negative uncertainties indicate the upper and lower bound of the prediction obtained by varying the scales and the charm mass as explained in chapter 2. The largest variations from the central prediction are obtained from the same variations which defined the uncertainty of the inclusive D^* cross section given in section 5.7. An exception is the lower bound of the FMNR prediction which is set by doubling the renormalisation scale. The relative size of the theoretical uncertainties for the D^* +jet cross section is lower than for the inclusive cross section by at least one third. For ZMVFNS the reduction is even larger.

The FMNR prediction after applying the hadronisation correction is below the data. Unlike for the inclusive D^* cross section only the upper bound of the theoretical uncertainties is compatible with the data within the experimental uncertainties. The ratio of

³The D^* fit is performed with the parameters μ , σ and u_s fixed to their values obtained from the inclusive D^* sample.

| | $\sigma_{vis}(ep \rightarrow e'D^* \text{ jet } X) \pm s_\sigma$ [nb] | s_σ/σ | $\sigma(D^*+\text{jet})/\sigma(D^*)$ |
|-----------------------------|---|-------------------|--------------------------------------|
| Data | $(2.96 \pm 0.23 \pm 0.43)$ | $\pm 16\%$ | 47.7% |
| FMNR \otimes had. corr. | $(2.27^{+0.62}_{-0.38})$ | +27% | 42.0% |
| FMNR | $(2.55^{+0.69}_{-0.43})$ | -16% | 47.2% |
| ZMVFNS \otimes had. corr. | $(2.44^{+0.48}_{-0.47})$ | +20% | 27.2% |
| ZMVFNS | $(2.73^{+0.54}_{-0.52})$ | -19% | 30.3% |
| CASCADE 1.2 | $(3.06^{+0.25}_{-0.26})$ | +8.0% | 55.4% |
| PYTHIA | 3.65 | | 45.7% |

Table 6.3: *The total visible $D^*+\text{jet}$ cross section $\sigma_{vis}(ep \rightarrow e'D^* \text{ jet } X)$ and its uncertainty s_σ compared with theoretical predictions. The FMNR and ZMVFNS predictions before applying the hadronisation correction are given for reference only. The last but one column states the relative uncertainties, where for the data the statistical and systematic contributions are added in quadrature. The right column shows the ratios between the $D^*+\text{jet}$ and the inclusive D^* cross sections. The chosen scales and particle density parametrisations of the calculations are given in table 5.8.*

the $D^*+\text{jet}$ and the inclusive D^* cross section, $\sigma(D^*+\text{jet})/\sigma(D^*)$, is underestimated, too. The ZMVFNS prediction now is below the data, but it is almost compatible with the data within either uncertainties. Since the inclusive D^* cross section was significantly overestimated, the ratio $\sigma(D^*+\text{jet})/\sigma(D^*)$ is significantly lower than for the data.

The CASCADE prediction now is closer to the data than for the inclusive sample where it was below. This can be understood since the p_t -spectrum of CASCADE has already been found to be too hard and since the jet requirement selects higher transverse momenta. PYTHIA overestimates the $D^*+\text{jet}$ measurement only slightly and its $\sigma(D^*+\text{jet})/\sigma(D^*)$ ratio is the closest to that in data.

Differential $D^*+\text{jet}$ cross sections are shown in the figures 6.17, 6.18 and 6.19, compared with the theoretical predictions. To indicate the size of the hadronisation correction, FMNR is shown once before and once after applying these corrections. The shaded and hatched bands indicate the upper and lower bound of the predictions. The contribution from the direct and resolved part of PYTHIA is also indicated. The resolved part is dominated by the charm excitation process.

The Transverse Momenta $p_t(D^*)$, $p_t(\text{jet})$ and $p_t(D^*+\text{jet})$

The differential cross sections as a function of the transverse momentum of the D^* and the jet are shown in the figures 6.17a-d). The p_t distributions of the D^* and the jet show the same behaviour as the inclusive $p_t(D^*)$ (figures 5.13a+b)). They are steeply falling with increasing p_t , the $p_t(\text{jet})$ distribution is even steeper.

Again the CASCADE predictions are too hard and PYTHIA is above the data mainly at low p_t . Within the uncertainties both next-to-leading order calculations can describe the p_t distributions, but both tend to be below the data for low p_t .

The $p_t(D^*+\text{jet})$ distribution (figures 6.17e-f)) peaks around 2.5 GeV. This is well described by CASCADE, besides the largest observed $p_t(D^*+\text{jet})$ where it is almost two

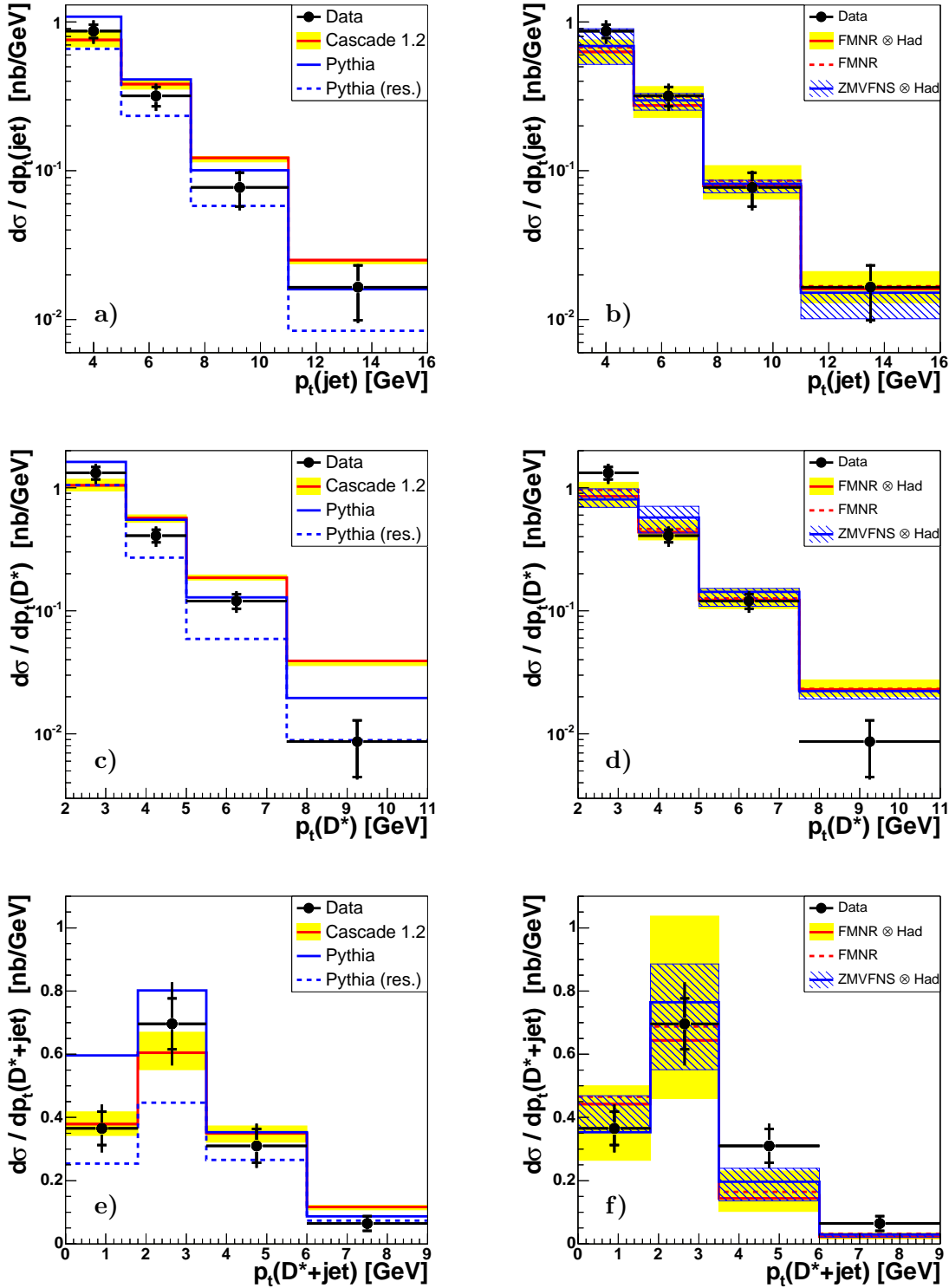


Figure 6.17: D^* +jet cross sections in bins of the transverse momentum of the jet (a,b), of the D^* meson (c, d) and of the combined D^* +jet system (e, f) compared with the predictions of PYTHIA and CASCADE on the left and of next-to-leading order calculations on the right. FMNR is a massive and ZMVFNS a massless calculation. For PYTHIA the sum of resolved and excitation processes is shown separately and labelled as “res.”.

standard deviations above the data. At large values of $p_t(D^*+\text{jet})$ the resolved fraction of PYTHIA is large and PYTHIA's overshoot in the total cross section seems to accumulate at small $p_t(D^*+\text{jet}) < 2.0$ GeV. Both next-to-leading order calculations tend to underestimate $p_t(D^*+\text{jet}) > 2.0$ GeV. For lower values the predictions match the data, but the uncertainties are very large. This is due to the fact that $p_t(D^*+\text{jet})$ is an infrared sensitive quantity. Small variations of the perturbative scales lead to large variations as has been discussed in section 2.3. Therefore the good agreement of the central prediction with the data at low $p_t(D^*+\text{jet})$ might be by chance.

The Pseudorapidities $\eta(D^*)$, $\eta(\text{jet})$ and Their Difference $\eta(D^*) - \eta(\text{jet})$

Figure 6.18 shows differential $D^*+\text{jet}$ cross sections as a function of the pseudorapidities $\eta(D^*)$, $\eta(\text{jet})$ and their difference $\eta(D^*) - \eta(\text{jet})$. The pseudorapidity distributions of the D^* and the jet differ significantly: The $\eta(D^*)$ distribution falls steeply with increasing values η , similar to the inclusive analysis (figures 5.13c+d), whereas $\eta(\text{jet})$ is almost flat. This difference is not caused by the slightly different kinematic cuts for the D^* and the jet as can be seen from the $\eta(D^*) - \eta(\text{jet})$ distribution of the direct PYTHIA component in figure 6.18e): It is symmetric as expected for direct processes (cf. section 1.6.2). It can be concluded that the jet in the forward direction is often caused by a gluon or a light quark, but not by a charm quark. The asymmetry between the $\eta(D^*)$ and $\eta(\text{jet})$ distributions is reflected in the distribution of the pseudorapidity difference $\eta(D^*) - \eta(\text{jet})$ which peaks below zero.

CASCADE describes all η distributions reasonably well. PYTHIA is above the data at negative $\eta(D^*)$ as for the inclusive sample and slightly above in the medium $\eta(\text{jet})$ range. The necessity of the inclusion of PYTHIA's resolved contribution to describe the data is clearly visible, especially for $\eta(\text{jet})$ and $\eta(D^*) - \eta(\text{jet})$.

Within their large uncertainties both next-to-leading order calculations reasonably describe the data. In the forward direction again the cross section is slightly underestimated for D^* mesons. The uncertainties of the predictions for jets in the forward direction are large and are transferred to negative $\eta(D^*) - \eta(\text{jet})$, too. They can be understood by the following consideration: The asymmetry between $\eta(D^*)$ and $\eta(\text{jet})$ indicates that most of the jets in the forward direction are produced by gluons and not by charm quarks. The amount of hard gluon radiation depends on the strong coupling constant α_s which itself depends on the renormalisation scale. Therefore varying this scale in the next-to-leading order calculations leads to significantly more or less hard gluon radiation, resulting in large variations in forward direction.

The $D^*+\text{Jet}$ Quantities $\Delta\phi(D^*, \text{jet})$, $m(D^*+\text{jet})$ and $x_\gamma(D^*+\text{jet})$

Cross sections in bins of the combined $D^*+\text{jet}$ quantities $\Delta\phi(D^*, \text{jet})$, $m(D^*+\text{jet})$ and $x_\gamma(D^*+\text{jet})$ are shown in figure 6.19.

The $\Delta\phi(D^*, \text{jet})$ distribution rises towards its maximum close to 180° , values below 80° hardly occur. Its rise is well described by CASCADE whereas PYTHIA overshoots the data at large $\Delta\phi(D^*, \text{jet})$. Without the resolved component PYTHIA cannot describe the region $\Delta\phi(D^*, \text{jet}) < 140^\circ$.

In the next-to-leading order calculations the negative contributions from interference terms dominate the largest $\Delta\phi(D^*, \text{jet})$ (cf. section 2.3). To achieve a cancellation with pos-

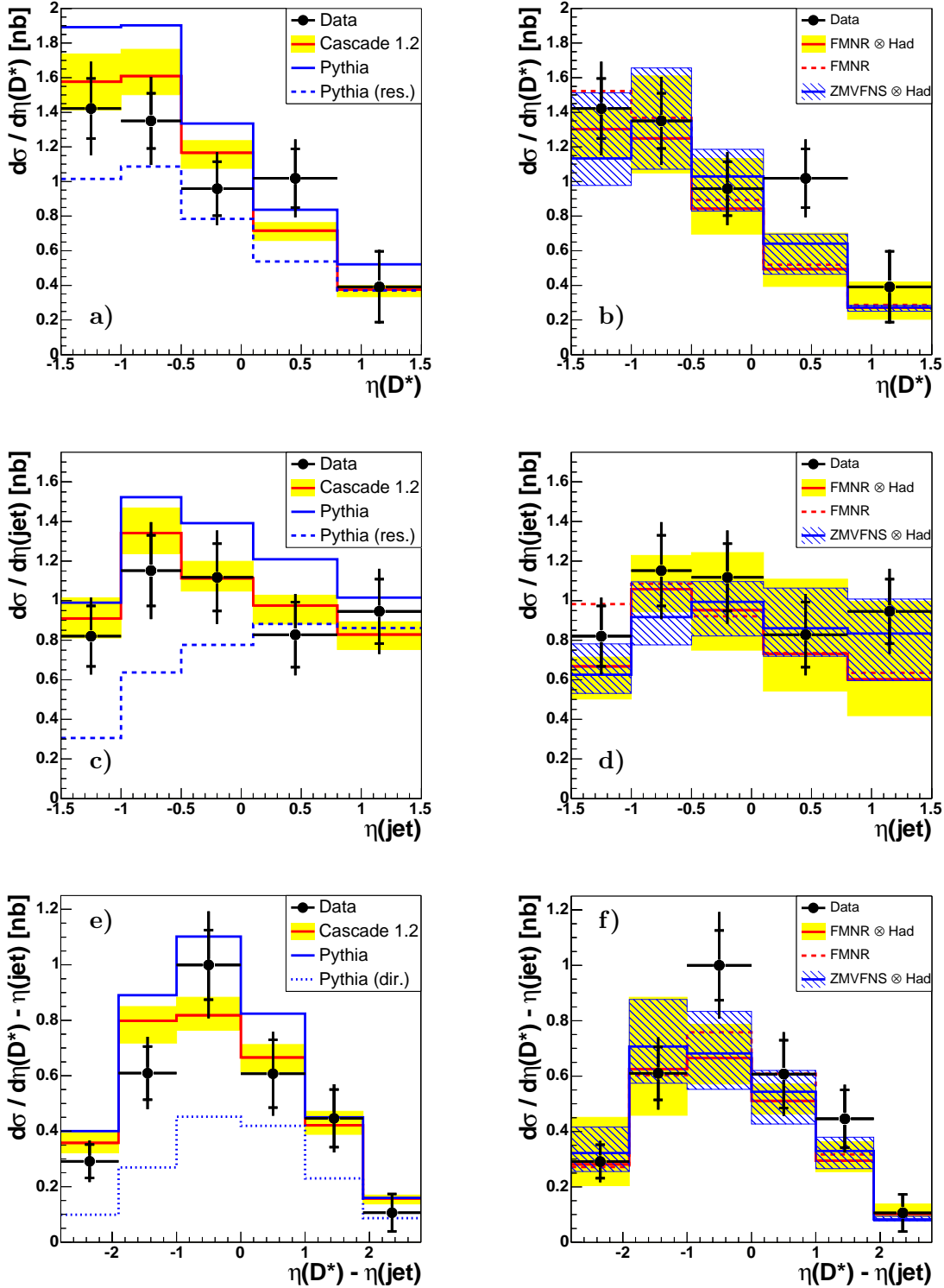


Figure 6.18: D^* +jet cross sections in bins $\eta(D^*)$ (a,b), $\eta(\text{jet})$ (c,d) and of the pseudorapidity difference $\eta(D^*) - \eta(\text{jet})$ (e,f) compared with the predictions of PYTHIA and CASCADE on the left and of next-to-leading order calculations on the right. FMNR is a massive and ZMVFNS a massless calculation. For PYTHIA the direct processes ($\eta(D^*) - \eta(\text{jet})$) or the sum of resolved and excitation processes ($\eta(D^*)$, $\eta(\text{jet})$) are shown separately and labelled as “dir.” and “res.”, respectively.

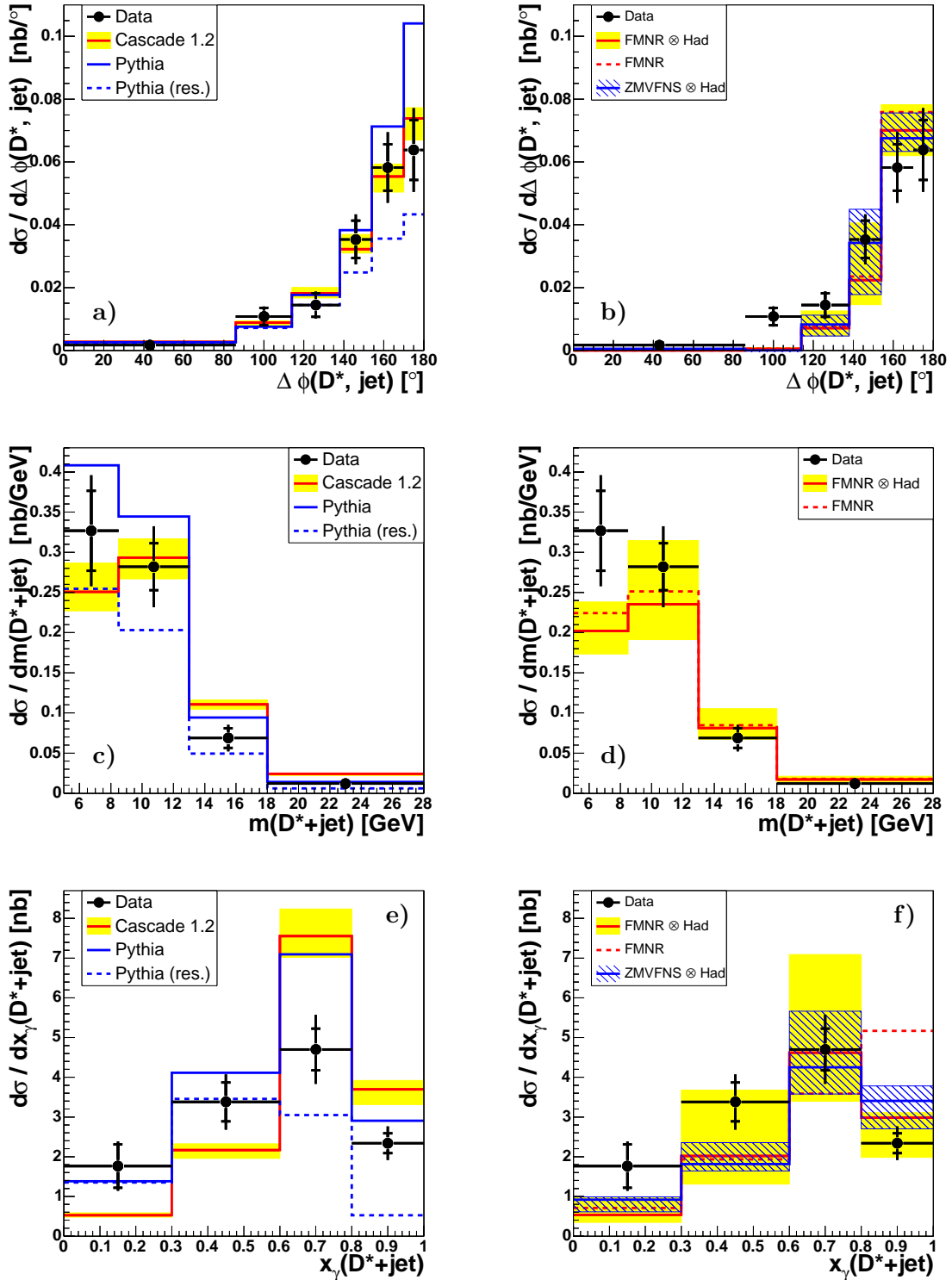


Figure 6.19: $D^*+\text{jet}$ cross sections in bins of the combined $D^*+\text{jet}$ quantities $\Delta\phi(D^*, \text{jet})$ (a,b), $m(D^*+\text{jet})$ (c,d) and $x_\gamma(D^*+\text{jet})$ (e,f) compared with the predictions of PYTHIA and CASCADE on the left and of next-to-leading order calculations on the right. FMNR is a massive and ZMVFNS a massless calculation. For PYTHIA the sum of resolved and excitation processes is shown separately and labelled as “res.”

itive terms the last two bins are merged, there the data are well described. Both FMNR and ZMVFNS show a large scale dependence at slightly lower values $138^\circ < \Delta\phi(D^*, \text{jet}) < 154^\circ$. The lowest $\Delta\phi(D^*, \text{jet})$ observed in the data, around 100° , are predicted neither by FMNR nor ZMVFNS. Since PYTHIA predicts a contribution in this region solely via resolved processes, it is unlikely that the missing cross section prediction of the NLO calculations in this region is caused by neglecting a transverse smearing in the D^* fragmentation of charm quark into the D^* meson. However, further studies are needed to investigate this hypothesis.

The cross section in the invariant mass $m(D^*+\text{jet})$ starts directly at its threshold ~ 5.5 GeV (for the D^* and the jet being back-to-back) defined by the minimal transverse momenta of the D^* and the jet and the D^* mass. It falls rapidly for $m(D^*+\text{jet})$ above ~ 12 GeV. The PYTHIA and CASCADE predictions differ at low $m(D^*+\text{jet})$, but the data are just in between. At large $m(D^*+\text{jet})$ CASCADE tends to be too high. The FMNR prediction reasonably describes the data, being somewhat below the data at low $m(D^*+\text{jet})$ values. No ZMVFNS prediction is available for this quantity.

The cross section as a function of $x_\gamma(D^*+\text{jet})$ has its maximum around 0.7 and not close to one, even for the contribution of direct photoproduction. This is different from usual definitions of x_γ , based on two jets, since the D^* carries only a fraction of the charm quark momentum whereas the D^* -jet more closely approximates the quark quantities. Nevertheless, $x_\gamma(D^*+\text{jet})$ can be used to separate direct or resolved processes in PYTHIA as can be seen in figure 6.19e). The distribution does not fall steeply towards $x_\gamma(D^*+\text{jet}) = 0$, but the cross section in the lowest bin is still about 40% of the maximal value. Neither PYTHIA nor CASCADE describe the shape of the distribution. They significantly overestimate the data at larger values $x_\gamma(D^*+\text{jet}) > 0.6$. In addition CASCADE is clearly below the data at low values. Also the NLO calculations tend to underestimate the lower values, but especially FMNR has large uncertainties. The large hadronisation correction brings the predictions closer to the data at the largest $x_\gamma(D^*+\text{jet})$.

Summarising, none of the calculations can describe all features of the measured $D^*+\text{jet}$ cross sections. In the following summary these results will be discussed together with the inclusive D^* cross sections presented in section 5.7.

Chapter 7

Summary and Discussion of D^* and D^* +Jet Cross Sections

Photoproduction of charm at HERA has been studied in data recorded by the H1 experiment in the years 1999 and 2000. The data correspond to an integrated luminosity of 51.1 pb^{-1} . Photoproduction processes are selected by detecting the scattered electron at small angles. This leads to a kinematical range of $Q^2 < 0.01 \text{ GeV}^2$ and $0.29 < y < 0.65$ where the latter corresponds to centre-of-mass energies of the photon-proton system of $171 < W_{\gamma p} < 256 \text{ GeV}$.

Charm has been tagged by reconstruction of D^* mesons in the decay channel $D^{*\pm} \rightarrow D^0 \pi_s^\pm \rightarrow K^\mp \pi^\pm \pi_s^\pm$. Particle identification using dE/dx slightly improves the signal-to-background ratio. The number of D^* mesons is determined by a fit to the distribution of the invariant mass difference $\Delta m = m(K\pi\pi_s) - m(K\pi)$. In total 1154 ± 84 D^* mesons have been reconstructed in the range $p_t(D^*) > 2.0 \text{ GeV}$ and $|\eta(D^*)| < 1.5$. The cross section in the visible kinematic region is

$$\sigma_{vis}(ep \rightarrow e'D^*X) = (6.20 \pm 0.45 \pm 0.90) \text{ nb.} \quad (7.1)$$

Differential and double differential cross sections $d\sigma/dp_t(D^*)$, $d\sigma/d\eta(D^*)$, $d\sigma/dW_{\gamma p}$ and $d^2\sigma/d\eta(D^*)dp_t(D^*)$ have been determined and compared with predictions of perturbative QCD (section 5.7). The leading order calculations PYTHIA and CASCADE are supplemented with parton showers, the former applies collinear and the latter k_t -factorisation, respectively. The next-to-leading order (NLO) calculations all apply collinear factorisation. FMNR predictions are calculated in the *massive* scheme, ZMVFNS predictions in the *massless* scheme and FONLL is a matched approach. Theoretical uncertainties arise from higher order terms and are estimated by scale variations. They are particularly large for the NLO calculations.

All calculations describe the measured shapes within the uncertainties. The $p_t(D^*)$ spectrum of the CASCADE prediction is a too hard and for ZMVFNS only the lower edges of the large uncertainties are close to the data. The $\eta(D^*)$ distribution indicates that the pure leading order photon-gluon-fusion (PGF) process in PYTHIA cannot describe the data.

The calculations include radiative processes in addition to the leading order PGF, leading to predictions closer to the observed shapes than without this radiation. PYTHIA includes charm excitation processes whereas in CASCADE k_t -unordered gluon radiation in the parton evolution from the proton side is present. In the NLO calculations one

additional radiation compared to the leading order PGF process is considered in the matrix element.

Still the $\eta(D^*)$ distribution cannot be perfectly described in shape by any calculation. In particular the data at $\eta(D^*) \approx 0.5$ tend to lie above the predictions. This irregularity is not prominent in the analysed data, but has already been observed in previous analyses on independent data sets from H1 [1] and ZEUS [7].

To investigate the charm production process in more detail, a jet not containing the D^* meson has been required in addition to the D^* . It has been shown that jets down to $p_t(\text{jet}) > 3$ GeV can be reliably measured in the central detector region. The transverse energy distribution relative to the jet axis as a function of the azimuth ϕ has been studied for different $p_t(\text{jet})$ and $\eta(\text{jet})$. It is well described by PYTHIA and CASCADE apart from $p_t(\text{jet}) > 8$ GeV and $\eta(\text{jet}) \approx 0.5$.

Requiring at least one jet with $p_t(\text{jet}) > 3$ GeV and $|\eta(\text{jet})| < 1.5$ results in a D^* +jet cross section of

$$\sigma_{vis}(ep \rightarrow e'D^* \text{ jet } X) = (2.96 \pm 0.23 \pm 0.43) \text{ nb.} \quad (7.2)$$

The ratio $\sigma(D^*\text{+jet})/\sigma(D^*)$ is described best by PYTHIA whereas it is overestimated by CASCADE and underestimated by the NLO calculations.

Differential cross sections for variables characterising the D^* , the jet and the D^* +jet system have been determined (section 6.8). The pseudorapidity distributions of the D^* and the jet are clearly different and it can be concluded that the jet in the forward direction is often caused by a gluon or a light quark, but not by a charm quark. This supports the assumption of a radiative process in addition to leading order PGF.

The prominent asymmetry in the $\eta(D^*)$ - $\eta(\text{jet})$ distribution is related to an asymmetry in the cosine of the scattering angle θ^* in the centre-of-mass system as explained in section 1.6.2. The $\cos\theta^*$ distribution has been investigated by ZEUS in dijet events with charm [8]. There it is concluded that a gluon propagator (cf. figure 1.4c) is important in charm photoproduction. The present analysis supports this conclusion at lower transverse momenta compared to the ZEUS analysis.

The $p_t(D^*\text{+jet})$ and $\Delta\phi(D^*, \text{jet})$ distributions can shed light on the mechanism producing the additional radiation. They are sensitive to transverse momentum k_t of the partons before the hard interaction. In CASCADE this transverse momentum results from the parton evolution in k_t -factorisation. Indeed only CASCADE describes both distributions quite well. On the other hand the CASCADE transverse momentum spectra are too hard both for the D^* and the jet.

The quantity $x_\gamma(D^*\text{+jet})$ is influenced by the amount of energy not contained in the D^* +jet system which may be lost in radiative processes. This distribution is not well reproduced by any of the calculations, CASCADE e.g. overestimates large values $x_\gamma(D^*\text{+jet}) \approx 0.7$. PYTHIA is too high in the same $x_\gamma(D^*\text{+jet})$ region, but in contrast to other calculations PYTHIA predicts a reasonably large contribution at low $x_\gamma(D^*\text{+jet})$ values.

Summarising it can be concluded that charm photoproduction at HERA is in general reasonably understood: In addition to the leading order PGF, radiative processes are found to be relevant. The exact mechanism of the radiation and its quantitative importance are difficult to prove since on the one hand none of the calculations describes all observed features in the data and on the other hand the uncertainties of the data and of the calculations are both large.

Chapter 8

Outlook

A deeper understanding of QCD radiation is important to get more insight in the strong interaction and to be able to predict precisely hard processes involving hadrons. Particularly in view of the **L**arge-**H**adron-**C**ollider (LHC) which is currently being built at CERN near Geneva, a proper understanding of the parton evolution and an accurate determination of the parton densities is required.

To achieve a deeper insight into the radiative QCD processes apparent in charm photoproduction, the uncertainties of the calculations which indicate the importance of higher order terms, have to be reduced. A first step would be a unified and consistent way to define these uncertainties. For the quantities that are not “infrared safe”, e.g. $\Delta\phi(D^*, \text{jet})$, a resummation of higher order terms is needed. Another promising concept is the MC@NLO approach where parton showers are matched to NLO matrix elements. At present MC@NLO calculations are not yet available for HERA.

The statistical uncertainties of the data are still quite large, particularly for D^* mesons in the forward direction or for small $x_\gamma(D^*+\text{jet})$. The data recorded by H1 in 1999 and 2000 contain about 700 D^* mesons in photoproduction tagged by a second electron tagger at $z = -43.2$ m. The signal-to-background ratio is better than for the analysed data of the tagger ET33. On the other hand the acceptance of the second tagger lies in the region of inelasticities $y \approx 0.1$, i.e. $W_{\gamma p} \approx 100$ GeV. The lower photon-proton centre-of-mass energy results in a lower rate of jets in addition to the D^* which can be observed in the central detector region. Therefore the statistics of $D^*+\text{jet}$ events is only about 150 events.

More statistics can be expected from the HERA II data, where a significantly larger integrated luminosity is envisaged. The challenge is to trigger charm photoproduction events, requiring improved trigger facilities. For this task the H1 experiment developed the Fast Track Trigger (FTT) on the trigger levels L1, L2 and L3 [84]. Already at the second level L2 track parameters in three dimensions are provided by the FTT. At the third level L3 the invariant masses of particle resonances, e.g. the mass difference Δm , can be calculated combining tracks.

A new electron tagger at $z = -5.4$ m is installed, replacing the ET33. It tags photoproduction events around $y \approx 0.75$ ($W_{\gamma p} \approx 275$ GeV). Due to the higher y smaller x can be reached, a kinematical region where k_t -effects are expected to increase. Of course it is desirable to develop a trigger for charm photoproduction that does not require the detection of the scattered electron. Such an untagged charm trigger is aimed for in the final commissioning of the FTT when the exact trigger thresholds and invariant mass algorithms will be defined.

Bibliography

- [1] C. Adloff, *et al.* (H1), Nucl. Phys., **B545**, (1999) 21. [hep-ex/9812023](#).
- [2] J. Abbiendi, *et al.* (ZEUS), Eur. Phys. J., **C6**, (1999) 67. [hep-ex/9807008](#).
- [3] C. Adloff, *et al.* (H1), Phys. Lett., **B528**, (2002) 199. [hep-ex/0108039](#).
- [4] S. Chekanov, *et al.* (ZEUS), Phys. Rev., **D69**, (2004) 012004. [hep-ex/0308068](#).
- [5] D. Acosta, *et al.* (CDF), Phys. Rev. Lett., **91**, (2003) 241804. [hep-ex/0307080](#).
- [6] M. Acciarri, *et al.* (L3), Phys. Lett., **B503**, (2001) 10. [hep-ex/0011070](#).
- [7] ZEUS-Collaboration, *Measurement of D^* Photoproduction at HERA*, 31st International Conference on High Energy Physics, ICHEP '02, Amsterdam (2002). Abstract 786, ZEUS-pre1-02-004,
URL http://www-zeus.desy.de/physics/phch/conf/amsterdam_paper.html.
- [8] S. Chekanov, *et al.* (ZEUS), Phys. Lett., **B565**, (2003) 87. [hep-ex/0302025](#).
- [9] J. Wagner, *Charm and Beauty Production at HERA with D^* -Muon Events*, Ph.D. thesis, Universität Hamburg (2004).
- [10] A. Aktas, *et al.* (H1), *Measurement of Charm and Beauty Photoproduction at HERA using $D^*\mu$ Correlations*, to be published (2005).
- [11] V. N. Gribov, L. N. Lipatov, Sov. J. Nucl. Phys., **15**, (1972) 438 and 675.
- [12] L. N. Lipatov, Sov. J. Nucl. Phys., **20**, (1975) 94.
- [13] G. Altarelli, G. Parisi, Nucl. Phys., **B126**, (1977) 298.
- [14] Y. L. Dokshitzer, Sov. Phys. JETP, **46**, (1977) 641.
- [15] E. A. Kuraev, L. N. Lipatov, V. S. Fadin, Sov. Phys. JETP, **45**, (1977) 199.
- [16] I. I. Balitsky, L. N. Lipatov, Sov. J. Nucl. Phys., **28**, (1978) 822.
- [17] M. Ciafaloni, Nucl. Phys. **B296**, (1988) 49.
- [18] S. Catani, F. Fiorani, G. Marchesini, Phys. Lett., **B234**, (1990) 339.
- [19] S. Catani, F. Fiorani, G. Marchesini, Nucl. Phys., **B336**, (1990) 18.
- [20] G. Marchesini, Nucl. Phys., **B445**, (1995) 49. [hep-ph/9412327](#).

- [21] C. Adloff, *et al.* (H1), Eur. Phys. J., **C30**, (2003) 1. [hep-ex/0304003](#).
- [22] S. Chekanov, *et al.* (ZEUS), Phys. Rev., **D67**, (2003) 012007. [hep-ex/0208023](#).
- [23] A. Aktas, *et al.* (H1), Eur. Phys. J., **C33**, (2004) 477. [hep-ex/0310019](#).
- [24] W.-K. Tung, S. Kretzer, C. Schmidt, J. Phys., **G28**, (2002) 983. [hep-ph/0110247](#).
- [25] C. Adloff, *et al.* (H1), Z. Phys., **C72**, (1996) 593. [hep-ex/9607012](#).
- [26] G. Heinrich, B. A. Kniehl, Phys. Rev., **D70**, (2004) 094035. [hep-ph/0409303](#).
- [27] L. Gladilin, *Charm Hadron Production Fractions* (1999). [hep-ex/9912064](#).
- [28] B. Andersson, G. Gustafson, G. Ingelman, T. Sjöstrand, Phys. Rept., **97**, (1983) 31.
- [29] C. Peterson, D. Schlatter, I. Schmitt, P. Zerwas, Phys. Rev., **D27**, (1983) 105.
- [30] V. Kartvelishvili, A. Likoded, V. Petrov, Phys. Lett., **B78**, (1978) 615.
- [31] J. Binnewies, B. A. Kniehl, G. Kramer, Phys. Rev., **D58**, (1998) 014014. [hep-ph/9712482](#).
- [32] S. Ellis, D. Soper, Phys. Rev., **D48**, (1993) 3160. [hep-ph/9305266](#).
- [33] J. M. Butterworth, J. P. Couchman, B. E. Cox, B. M. Waugh, Comput. Phys. Commun., **153**, (2003) 85. [hep-ph/0210022](#).
- [34] F. Jacquet, A. Blondel, in *Study of an ep-Facility for Europe* (ed. U. Amaldi), 391–396 (DESY, 1979).
- [35] S. Frixione, B. R. Webber, JHEP, **06**, (2002) 029. [hep-ph/0204244](#).
- [36] S. Frixione, P. Nason, B. R. Webber, JHEP, **08**, (2003) 007. [hep-ph/0305252](#).
- [37] T. Sjöstrand, *et al.*, Comput. Phys. Commun., **135**, (2001) 238. [hep-ph/0010017](#).
- [38] H. Jung, G. P. Salam, Eur. Phys. J., **C19**, (2001) 351. [hep-ph/0012143](#).
- [39] H. Jung, Comput. Phys. Commun., **143**, (2002) 100. [hep-ph/0109102](#).
- [40] H. Jung, *The CCFM Monte Carlo Generator CASCADE Version 1.2007* (2004). URL <http://www.desy.de/~jung/cascade/cascade12007.ps.gz>.
- [41] H. L. Lai, *et al.* (CTEQ), Eur. Phys. J., **C12**, (2000) 375. [hep-ph/9903282](#).
- [42] M. Glück, E. Reya, A. Vogt, Phys. Rev., **D46**, (1992) 1973.
- [43] H. Jung, in *XII International Workshop on Deep Inelastic Scattering (DIS 2004)* (eds. D. Bruncko, J. Ferencei, P. Stríženec), vol. 1, 299–302 (SAS, 2004). [hep-ph/0411287](#).
- [44] S. Eidelman, *et al.* (Particle Data Group), Phys. Lett. **B592**, (2004) 1.
- [45] S. Frixione, M. L. Mangano, P. Nason, G. Ridolfi, Phys. Lett. **B348**, (1995) 633. [hep-ph/9412348](#).

- [46] S. Frixione, P. Nason, G. Ridolfi, Nucl. Phys., **B454**, (1995) 3. hep-ph/9506226.
- [47] B. A. Kniehl, in *14th Topical Conference on Hadron Collider Physics* (eds. M. Erdmann, T. Müller), 161–170 (Springer, Heidelberg, 2003). hep-ph/0211008.
- [48] A. D. Martin, R. G. Roberts, W. J. Stirling, R. S. Thorne, in *XI International Workshop on Deep Inelastic Scattering (DIS 2003)* (eds. V. T. Kim, L. N. Lipatov), 150–154 (PNPI, 2003). hep-ph/0307262.
- [49] P. Aurenche, J. P. Guillet, M. Fontannaz, to be published (2004/5).
- [50] J. Pumplin, *et al.* (CTEQ), JHEP, **07**, (2002) 012. hep-ph/0201195.
- [51] M. Cacciari, S. Frixione, P. Nason, JHEP, **03**, (2001) 006. hep-ph/0102134.
- [52] S. Frixione, P. Nason, JHEP, **03**, (2002) 053. hep-ph/0201281.
- [53] G. Kramer, H. Spiesberger, Eur. Phys. J., **C38**, (2004) 309. hep-ph/0311062.
- [54] M. Cacciari, P. Nason, unpublished (2003).
- [55] C. Grab, private communication (2004).
- [56] P. Nason, C. Oleari, Nucl. Phys., **B565**, (2000) 245. hep-ph/9903541.
- [57] A. Aktas, *et al.* (H1), *To be submitted to* Eur. Phys. J., **C**. DESY 05-004.
- [58] S. Hengstmann, *A Measurement of Diffractive Charm Production at HERA*, Ph.D. thesis, Universität Zürich (2000).
- [59] I. Abt, *et al.* (H1), Nucl. Instrum. Meth., **A386**, (1997) 310.
- [60] I. Abt, *et al.* (H1), Nucl. Instrum. Meth., **A386**, (1997) 348.
- [61] D. Dünkemann, *Wirkungsquerschnitte für Photoproduktion von D^* -Mesonen in ep -Wechselwirkungen am H1-Experiment bei HERA*, Diploma thesis, Universität Hamburg (2001).
- [62] D. Pitzl, *et al.*, Nucl. Instrum. Meth., **A454**, (2000) 334. hep-ex/0002044.
- [63] A. Aktas, *et al.* (H1), Eur. Phys. J., **C38**, (2005) 447. hep-ex/0408149.
- [64] B. Andrieu, *et al.* (H1 Calorimeter Group), Nucl. Instrum. Meth., **A336**, (1993) 460.
- [65] R. D. Appuhn, *et al.* (H1 SPACAL Group), Nucl. Instrum. Meth., **A386**, (1997) 397.
- [66] R. D. Appuhn, *et al.* (H1 SPACAL Group), Nucl. Instrum. Meth., **A374**, (1996) 149.
- [67] H1-Collaboration, *Luminosity Measurement in the H1 Experiment at HERA*, 28th International Conference on High Energy Physics, ICHEP '96, Warsaw (1996). Abstract pa17-026, URL <http://documents.cern.ch/ichep96/talk/669.html>.
- [68] S. Aid, *et al.* (H1), Z. Phys., **C69**, (1995) 27. hep-ex/9509001.

- [69] J. Steinhart, *Die Messung des totalen $c\bar{c}$ -Photoproduktions-Wirkungsquerschnittes von Λ_c -Baryonen unter Verwendung der verbesserten dE/dx -Teilchenidentifikation am H1-Experiment bei HERA*, Ph.D. thesis, Universität Hamburg (1999).
- [70] R. Brun, *et al.*, *GEANT 3 User's Guide* (1987). CERN-DD/EE/84-1.
- [71] M. Peez, B. Portheault, E. Sauvan, *An Energy Flow Algorithm for Hadronic Reconstruction in OO: Hadroo2*, H1 internal note (2005). H1-01/05-616.
- [72] L. West, *How to Use the Heavy Flavour Working Group Track, Muon and Electron Selection Code*, H1 internal software manual (2000).
- [73] B. Weßling, *Measurement of the Beauty Cross Section using the Semileptonic Decay into Electrons at HERA*, Ph.D. thesis, Universität Hamburg (2004).
- [74] U. Kathage, *Photoproduktion von $D^{*\pm}$ -Mesonen bei HERA*, Ph.D. thesis, Universität Kiel (1997).
- [75] G. Feldman, *et al.*, Phys. Rev. Lett., **38**, (1977) 1313.
- [76] F. Sefkow, *et al.*, IEEE Trans. Nucl. Sci., **42**, (1995) 900.
- [77] H. Beck, *Principles and Operation of the z-Vertex Trigger*, H1 internal note (1996). H1-05/96-479.
- [78] T. Wolff, *et al.*, *A Driftchamber Track Finder for the First Level Trigger of H1*, H1 internal note (1992). H1-02/92-213.
- [79] J. Reidberger, *The H1 Trigger with Emphasis on Tracking Triggers*, H1 internal note (1995). H1-01/95-419.
- [80] Heavy Flavour Group (H1), *HQSEL45* (1999).
URL <https://www-h1.desy.de/h1/iww/iwork/ihq/sw-doc/hqsel99.html>.
- [81] S. Schmidt, *Messung charminduzierter Zweijetereignisse in tief inelastischer ep-Streuung mit dem H1-Detektor*, Ph.D. thesis, Technische Universität München (2004).
- [82] G. Flucke, in *XI International Workshop on Deep Inelastic Scattering (DIS 2003)* (eds. V. T. Kim, L. N. Lipatov), 711–714 (PNPI, 2003).
- [83] T. Affolder, *et al.* (CDF), Phys. Rev., **D65**, (2002) 092002.
- [84] A. Baird, *et al.*, IEEE Trans. Nucl. Sci., **48**, (2001) 1276. hep-ex/0104010.

Danksagung

Mein Dank geht an alle, die diese Arbeit ermöglicht und begleitet haben.

Allen voran sei Herrn Prof. Blobel gedankt für seine Betreuung und die lehrreichen Gespräche über Statistik und Spurrekonstruktion.

Herrn Prof. Klanner sei gedankt für die Übernahme des zweiten Gutachtens.

Gedenken möchte ich Dr. Ralf Gerhards', dessen Begeisterung für schwere Quarks mich zu dieser Arbeit gebracht hat und der im Dezember 2003 so plötzlich verstorben ist.

Dr. Hannes Jung danke ich für die Bereitschaft, daraufhin meine Betreuung zu übernehmen, sowie für seine erhellenden Erklärungen zum Thema Faktorisierung und für viele Ideen.

Dank geht an Frau Prof. Naroska für die vielen Anregungen, Dinge klarer zu formulieren, an Dr. Christoph Grab für die Beantwortung mancher Frage zum FMNR-Programm, an Dr. Gudrun Heinrich für die ZMVFNS-Rechnungen in meinem kinematischen Bereich und an Lluís für die Hilfe bei der Erstellung der CASCADE-Vorhersagen.

Die gute Atmosphäre unseres Büros verdanke ich meinen jetzigen und ehemaligen Kolleginnen und Kollegen Angela, Bengt, Dirk, Ingo, Jeannine, Martin, Svetlana und Thomas. Mit Bengt und Ingo hatte ich viel Spaß, das H100-Projekt zum Laufen zu bringen und am Laufen zu halten – auch wenn die Daten oft immer noch zu kriechen scheinen. . .